Alma Mater Studiorum – Università di Bologna

DOTTORATO DI RICERCA IN

Ingegneria Elettrotecnica

Ciclo XXVIII

Settore Concorsuale di afferenza: 09/E1

Settore Scientifico disciplinare: ING-IND/31

TITOLO TESI

Superconducting technology for power and energy management

Presentata da: Babak Gholizad

Coordinatore Dottorato	**Relatore**
Prof. Domenico Casadei	**Prof. Antonio Morandi**

Esame finale anno 2016

I dedicate this thesis to my family and long standing friends for their constant support and unconditional love.
I love you all dearly.

ABSTRACT

In this thesis integration of high temperature superconductor technology in the future advanced power system will be investigated. In particular, superconducting magnetic energy storage system (SMES) for power quality of distribution grid and customer protection will be discussed. The complete design method, including the magnet and power electronic interface design will be discussed in more details. The method will be applied to the design of an industrial scale SMES system. Commercially available high temperature superconductor (HTS) material (YBCO) and magnesium diboride (MgB_2) tapes will be considered for the design of the magnet. A multifunctional control algorithm for compensating voltage sag and improving power quality will be implemented, and the advantages of the SMES system and utilized control algorithm for this application will be illustrated.

As a second part of the thesis, high temperature superconducting DC (HTS-DC) cables for transmission and distribution will be introduced. A method for both electromagnetic and thermo fluid-dynamic design of power cable will be developed. As a first case study superconducting DC collector grid for offshore wind-park will be technically and economically evaluated and the cost and loss model of the system will be discussed. Also, the transient behavior of the high temperature superconducting DC cable in high voltage DC (HVDC) system, which is crucial for stability, will be evaluated. Both line commutated converters (LCC) and voltage source converters (VSC) will be considered.

ACKNOWLEDGMENT

After finishing a journey, you look back and realize how it changed you, how it helped you grow, and how it helped shape who you are. This has been undoubtedly a magnificent experience which has enriched me both personally and professionally. First of all, I would like to thank to my family in Iran, for all the support and encouragement they provided during all the years of my growth. Without their support I would not have been able to complete my PhD research work successfully. Furthermore, I would like to thank to all my friends in Iran for all the care and support they provided me, regardless the distance, and in spite of their own problems. I would like to express my deepest and sincere gratitude to my advisor Prof. Antonio Morandi for the continuous support of my Ph.D study and research, for his patience, motivation, enthusiasm, and knowledge. His guidance helped me in all the time of my research activity and the writing of this dissertation. His professional supervision and immense technical knowledge have helped my research to steer in the right direction and framed this thesis. His support and guidance have always given me strength to continue forward. All the merits for the results obtained during my research period should be addressed to him. I am looking forward to extend our collaboration also for the future research work. Besides my advisor, I would like to thank the rest of the academic board of the DEI for their kindness, collaborations and willingness to help. My special thanks go to Prof. Rik W. De Doncker director of E.ON Energy Research Center and Institute for Power Generation and Storage Systems (PGS) because of his encouragement and insightful comments during my internship in the RWTH Aachen University Germany. From this university I would like to thank Dr. Ing. Hanno Stagge, Dip. Ing. Nils Soltau, and Dip. Ing. Marco Stieneker for the valuable discussions on the DC networks and Offshore Wind Park collector grid. Also, I would like to thank the rest of the PGS group too. I had very good moments with this group during my internship period. I am very thankful the three years financial support of my PhD by Uinbo scholarship. Also, Marco Polo Grant by DEI for my internship in Germany (2014) is acknowledged. All the friends and colleagues are the subject of my special thanks. Best wishes for your future plans and endeavors. I must declare my joyful life here in Italy. It was a great opportunity to live in such a wonderful country as expected.

TABLE OF CONTENT

TABLE OF FIGURES

TABLE OF TABLES

PART I. SUPERCONDUCTING MAGNETIC ENERGY STORAGE SYSTEM

1. INTRODUCTION

The energy storage system is the key technology for assuring appropriate power quality and for increasing the penetration of renewable sources. Several energy storage technologies exist, each of which offering specific performances. Among these, Superconducting Magnetic Energy Storage (SMES) offers important advantages, including fast response time from standby to full power. The SMES system may not be cost effective currently, but they are attractive because of the positive cost and environmental impact of them through the reduced fuel consumption and emissions [1.1]. The advantages of the SMES system can be highlighted as [1.2]:

- high deliverable power,
- virtually infinite number of charge discharge cycles without degradation, and
- high round trip efficiency.

Due to these characteristics, SMES can find a very wide application as stand-alone storage device or in combination with other storage technology with complementary characteristics (e.g. in hybrid Battery-SMES storage systems [1.3]), both at the customer and at the grid level. The SMES was initially envisioned as a large-scale load-leveling device, while the energy storage density of the SMES system is less than the other storage systems, now it is seen mainly as a tool for enhancing system stability, power transfer, and power quality applications. Improving the superconducting and power electronic technologies besides the SMES characteristics and benefits will make the use of SMES more desirable for power utility applications.

1.1. GENERAL SPECIFICATIONS AND APPLICATIONS OF THE ENERGY STORAGE SYSTEM

An energy storage system is made up of a storage device, which absorb and store the energy or delivers stored energy to the network with some losses, and a power conditioning system (a set of solid state power converters) which control the power exchange between the electric terminals of the storage device and the grid. Auxiliary devices such as cooling and control, which also they have some losses, are usually needed for the operation of the system. The storage systems have a cyclic operation which includes the charge, discharge and idle work duration (the energy supplied to the grid must be first absorbed from the grid) in power systems. However, it must be considered that in many applications the parameters of the operating cycle (duration, charge and discharge time, possibly idling) changes continuously and randomly [1.2].

The main parameters of an energy storage system are

- Maximum power (charge/discharge rate) that can be absorbed or supplied, P
- Duration of the power delivery, Δt
- Response time required for making the maximum power available starting from stand-by, t_r
- Number of cycles that can be reliably endured during the lifetime, N

The input / output power of the storage system can be fully controlled if the storage system is not discharged below the certain level this limitation is exist because of the intrinsic characteristics of the power conversion / conditioning systems [1.2]. The minimum quantity of energy E_{min} should always remain in the storage device. If the maximum power P is to be delivered for the interval Δt the rated energy E of the device can be obtained as:

$$E = E_{\text{min}} + P\Delta t \tag{1.1}$$

The efficiency of the storage system in a cycle can be defined as follows [1.2]:

$$\eta = \frac{P\,\Delta t}{\dfrac{P\,\Delta t}{\eta_s\,\eta_c} + P_{\text{idle}}\,\Delta t_{\text{idle}} + P_{\text{aux}}\,\Delta t_{\text{cycle}}} \tag{1.2}$$

where η_s is the round trip efficiency of the storage device (from electricity back to electricity), η_c is the efficiency of the converters, P_{aux} is the power required for auxiliary services and P_{idle} is the power loss (if any) during the possible idling phase. It is clear from equation (1.2) that low auxiliary and idling losses are essential for efficient long term storage ($\Delta t_{\text{cycle}} >> \Delta t$ and $\Delta t_{\text{idle}} >> \Delta t$). However the impact of these losses on the efficiency of the energy will be less if the high rate power exchange experience with the storage system over the short cycles [1.2].

A total generated power and the load power in the electric system must continuously be in balanced condition. In power system imbalance due to the random fluctuation of loads induced by customers, or due to the variation of generation from non-programmable sources (i.e. renewables), generation/transmission failure occurs. In power system system-wide failure (black out) can occur due to the power imbalance if it is not promptly compensated. Continuous and fast regulation of the generated power (and/or loads) is then required. Load imbalance occurs in a power system on different time scales, from less than one second in case of contingency to minutes following the typical change induced by customers or variable generation. A very large variation of the load occurs at intervals of hours. A potential method for reducing load imbalances and assuring the reliability of the power system is energy storage [1.2] and [1.4]. Energy storage also allows a more economic planning and exploitation of the generation resources. Furthermore, it can also be used at the customer level for appropriate power quality or for smoothing the power absorption of impulsive loads. The main specifics of the storage system for each of the applications are indicatively shown in Figure 1.1. Other applications such as damping of sub-synchronous resonance, black start or deferral of new transmission and distribution are also possible, but are likely to have a more limited cost/benefit trade-off. Smart loads and smart grid, beside energy storage, are also emerging as an integrating technology for energy management in the electric power systems [1.2]. Furthermore the increase of transmission capacity by means of multi-terminal DC links to exchange generating resources over larger areas is also receiving an increasing attention for the same reason [1.5]. Finally, improved controllability of conventional generation can also bring significant contributions [1.2].

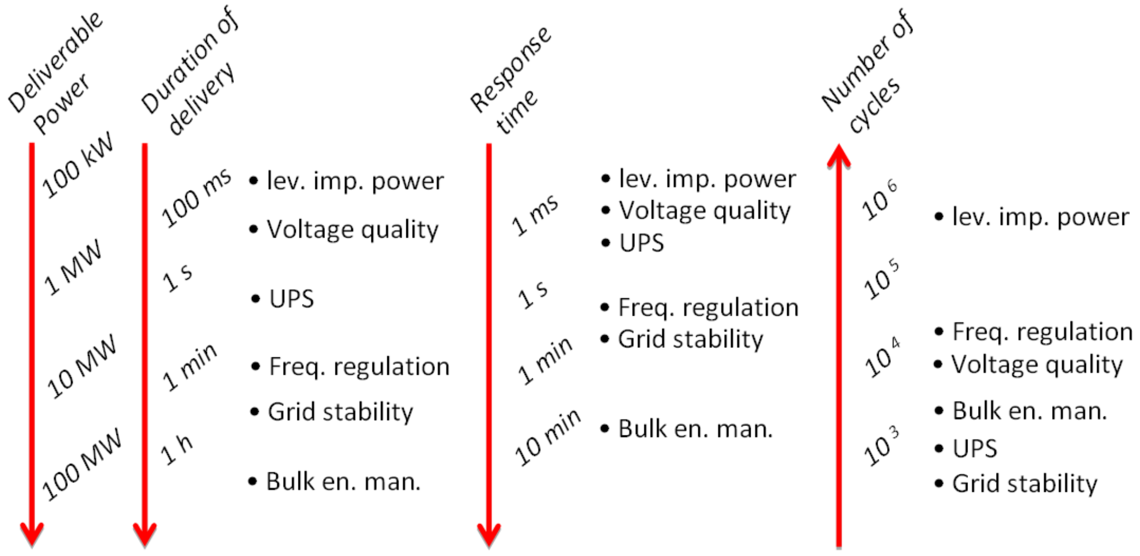

Figure 1.1 Parameters of the storage system for different applications [1.2]

1.2. THE ROLE OF THE SMES SYSTEM IN POWER SYSTEM

In 1970s superconducting energy storage system (SMES) was first proposed as technology in power systems. In the SMES energy is stored in the magnetic field which is generated by the circulating DC current in the large inductance, the inductance made by the superconducting coil. A SMES system consists of a superconducting coil, the cryogenic system which provides the cold environment to guarantee the superconductivity in the coil, power conversion or conditioning system (PCS) with control and protection function. Since in the SMES there is no energy conversion from one form to another form the total efficiency of the round trip working of the

SMES system can be very high. However, round trip efficiency of the SMES depends on the idle working time during the round trip operations (see equation (1.2)), while the losses due to the idle working time period in power electronic switches and continues cooling requirements will decrease the efficiency of the SMES system; if the duration of the idle working is not so long during the round trip operation of the SMES system, the efficiency of the SMES system can be more than 90% [1.2]. Depending on its PCS unit's control loop and power electronic switches characteristic, the SMES system can respond rapidly (MWs/milliseconds). While there is no moving part in the SMES system, it is reliable and environmentally friendly technology. Compared to other storage technologies, the SMES technology has a unique advantage in two types of applications:

1. power system transmission control and stabilization, and
2. power quality power systems [1.1].

Round trip efficiency and faster response capability of the SMES system has been and can be further exploited in different applications in all levels of electric power systems. SMES systems have the capability of providing

- load leveling,
- frequency support (spinning reserve) during loss of generation,
- enhancing transient and dynamic stability,
- dynamic voltage support (VAR compensation),
- improving power quality,
- increasing transmission line capacity,
- thus, overall enhancing security and reliability of power systems

The characteristics of potential SMES applications for generation, transmission, and distribution are given in Table 1.1 and depicted in Figure 1.1.

Among these applications, the ones with power ranges of 20–200 MW and energy ranges of 50–500 MJ (0.014–0.14 MWh) have been found to be the most cost beneficial applications [1.1]. As can be seen from Table 1.1, applications of transmission stability and frequency control are therefore economically attractive. Furthermore, custom power and power quality have also been found to be economically feasible low-power applications for SMES [1.1] and [1.7].

Also, the SMES can integrate with the flexible AC transmission system (FACTS) controllers to provide energy storage at the transmission level or custom power devices at the distribution level [1.6]. Adding significant energy storage capability to the FACTS controllers (e.g. StatCom) allows these devices to provide active power in addition to reactive power; and the number of degrees of the freedom for control purposes will increase to two. Therefore the effectiveness of the outer power system control function increases, and enhancing system reliability and/or availability will be possible.

Table 1.1. Typical stored energy for various power systems applications of SMES (in 1MWh = 3600MJ) [1.1] and [1.7]

	Application	Typical Stored Energy Capacity	Typical Discharge Period
Generation	Load leveling	100 – 5000	Hours
	Dynamic Response	80 – 2000	Hours
	Spinning Reserve	2 – 300	Minutes
	Frequency Control	0.15 – 15	Seconds
Transmission	Load Leveling	10 – 1000	Minutes – Hours
	Stabilization	0.002 – 10	Seconds
	Voltage/VAR Control	0.0003 – 0.03	Milliseconds (Cycles)
Distribution	Load Leveling	0.015	Minutes –Hours
	Power Quality	0.00003 – 0.003	Seconds
	Custom Power	0.00003 – 0.003	Milliseconds (Cycles)

1.3. IMPROVED FACTS CONTROLLER: FACTS AND SMES

Second generation FACTS controllers are power electronic devices with integrated energy storage that handles both the active and reactive power to enhance the transmission system performance. With the appropriate configuration and control, they can influence the transmission system parameters such as impedance, voltage, and phase angle. FACTS controllers can be connected to the power system in series, parallel or combined form and they can utilize or redirect the available power and energy from the AC system. Without energy storage, they are limited in the degree of freedom and sustained action in which they can help the power grid [1.8]. One of the viable energy storage technologies, SMES, can be added to a FACTS controller to significantly improve the control actions of FACTS.

A SMES system requires a PCS that can be either a voltage or current source inverter. Since the inverter utilized for a FACTS controller is voltage source based, it is a logical approach to attach the SMES to a FACTS controller. The integration of a FACTS device with the SMES can provide independent real and reactive power absorption/injection from/into the grid. The combined system would not only provide better performance than separate stand-alone devices, but it could also have a lower cost since the combined system can generate the same performance with lower ratings. Custom power devices are similar to FACTS devices in topology, but at smaller ratings. Most of the current SMES projects use small-scale or micro SMES devices [1.9]-[1.11]. They can also be attached to custom power devices to increase the effectiveness of the overall system.

1.4. TRANSIENT CONCERNS IN SMES OPERATION

The power electronics applications in power systems continue to increase. Normal and abnormal switching of power electronics devices may generate transient over-voltages. These over-voltages, take place in very short time compared to steady state, but, they may have potential to damage any equipment that is subject to these transients. Therefore, the control and modeling of power electronics devices is an important task in power system transient studies.

A SMES system is comprised of power electronics devices. Switching actions of these devices during charge and discharge may cause serious transient over-voltages. These transients may have potential to damage the coil insulation. The SMES unit may fail simply because the insulation level was not designed to withstand transients. Most of the SMES failures have been experienced due to insulation and protection problems. This is especially more important for large coils [1.12]. It is essential to characterize the transients that may be experienced by the SMES coil for insulation and protection purpose. A good analysis of transient interaction between a superconducting coil and its power electronics interface is crucial to avoid any insulation problem that may be experienced.

A detailed model of the coil is necessary to identify the transients better. Breaking down the coil into small pieces, representing the entire coil and analyzing the internal node voltages will give a better understanding of the transients that may affect the coil. A detailed modeling of the superconducting coil along with the power electronics interface modeling and control are essential in the electromagnetic transient interaction analysis.

1.5. REFERENCES

[1.1] S. Eckroad, “Program on Technology Innovation: Modeling of SMES and Its Integration to the Power Grid”, 1012153, EPRI final report December 2006, online available at: http://goo.gl/3A3C2z

[1.2] A. Morandi, “5. Power applications – 5.5 Energy Storage (SMES and Flywheels)”, in Applied Superconductivity: Handbook on Devices and Applications, Editor P. Seidel, Weinheim: Wiley-VCH; 2015, pages 660-674, http://dx.doi.org/10.1002/9783527670635

[1.3] T. Ise, M. Kita, A. Taguchi, “A hybrid energy storage with a SMES and secondary battery,” IEEE Transactions on Applied Superconductivity, vol.15, no.2, June 2005, pages 1915-1918, DOI: 10.1109/TASC.2005.849333

[1.4] P. Denholm, E. Ela, B. Kitby, and M. Milligan “The Role of Energy Storage with Renewable Electricity Generation” NREL report No. TP-6A2-47187, January, 2010, (http://www.nrel.gov/docs/fy10osti/47187.pdf)

[1.5] P. Fairley, “HVDC Supergrid Technologies Besting Expectations,” IEEE Spectrum, March, 2013, online available at: http://goo.gl/fU4c4y

[1.6] A. Arsoy, Yilu Liu, and P. F. Ribeiro “Electromagnetic Transient and Dynamic Modeling and Simulation of a StatCom-SMES Compensator in Power Systems,” IEEE Power Engineering Society Winter Meeting, 2002, Vol. 1 pages 502 - 505 (DOI: 10.1109/PESW.2002.985052)

[1.7] P.F. Ribeiro, “SMES for Enhanced Flexibility and Performance of FACTS Devices,” IEEE Summer Meeting, 18 Jul 1999-22 Jul 1999, Pages: 1120 - 1131 vol.2, DOI: 10.1109/PESS.1999.787475

[1.8] V. Karasik, K. Dixon, C. Weber, B. Batchelder, P. Ribeiro, “SMES for Power Utility Applications: A Review of Technical and Cost Considerations,” IEEE Transactions on Applied Superconductivity, Vol.9, No.2, June 1999, pages 541-546, DOI: 10.1109/77.783354

[1.9] B. Wei, P. Chen, M. Qiu, H. Zhang, J. Zhu, Y. Yang, and X. Lai “Experimental Investigation into the Characteristics of Micro-SMES’ Magnet,” IEEE Transactions on Applied Superconductivity, Vol. 22, No. 3, June 2012, DOI : 10.1109/TASC.2011.2175869

[1.10] T. Nakayama, T. Yagai, M. Tsuda, and T. Hamajima “Micro Power Grid System with SMES and Superconducting Cable Modules Cooled by Liquid Hydrogen” IEEE Transactions on Applied Superconductivity, Vol. 19, No. 3, June 2009, pages 2062-2065, DOI: 10.1109/TASC.2009.2018743

[1.11] M. Song, J. Shi, Y. Liu, Y. Xu, N. Hu, Y. Tang, L. Ren, and J. Li “100 kJ/50 kW HTS SMES for Micro-Grid” IEEE Transactions on Applied Superconductivity, Vol. 25, NO. 3, June 2015, DOI:10.1109/TASC.2014.2386345

[1.12] H. Hayashi, K. Tsutsumi, F. Irie, T. Teranishi, S. Hanai, L. Kushida, “Analysis and countermeasure for a problem of abnormal voltage generation in a SMES magnet,” CEC/ICMC Cryogenic Engineering Conference and International Cryogenic Materials Conference, Montréal, Québec, CANADA (12/07/1999) 2000, vol. 45 (A) (985 pages) (2 ref.), pp. 683-688 (http://cat.inist.fr/?aModele=afficheN&cpsidt=927382)

2. AN OVERVIEW OF SUPERCONDUCTING MAGNETIC ENERGY STORAGE SYSTEMS

2.1. PRINCIPLES OF OPERATION

In the SMES, a circulating DC current through the superconducting conductor in the large magnet creates the magnetic field and stores the electrical energy in the magnetic field. The common specifications of the SMES device are the inductively stored energy (E in Joule) and the rated power (P in Watt), and could express as follows:

$$\begin{aligned} E &= \frac{1}{2} L_\mathrm{c} I_\mathrm{c}^{2} \\ P &= \frac{\mathrm{d}E}{\mathrm{d}t} = L_\mathrm{c} I_\mathrm{c} \frac{\mathrm{d}I_\mathrm{c}}{\mathrm{d}t} = V_\mathrm{c} I_\mathrm{c} \end{aligned} \tag{2.1}$$

where L_c is the inductance of the coil, I_c is the DC current flowing through the coil, and V_c is the voltage across the coil.

The relationship between the volumetric energy density (E_v in J/m^3) and magnetic field density (B in T) is given by

$$E_\mathrm{v} = \int_{\tau_\infty} \frac{B^2}{2\mu_0} d\tau \approx \int_{\tau_\mathrm{coil}} \frac{B^2}{2\mu_0} d\tau \tag{2.2}$$

where B is the magnetic flux density, $\mu_0 = 4\pi 10^{-7}$ [VsA^{-1}m^{-1}] is the magnetic permeability of the vacuum, and τ_∞ is the infinite space. The cooling and the protection system is also an integral part of the SMES. In practice the integral can be restricted without introducing a relevant error over the region where the magnetic field is significant, that is the volume τ_coil occupied by the coil. This includes the cross section of the coil, where the conductors are allocated, and the bore. If the coil is superconducting, it has no resistance and, provided that a perfect short circuit can be created at its terminals, the magnetic energy can be stored indefinitely since no decay of the current occurs. In alternative if the terminals can be connected by means of a low resistance contact a low dissipation occurs [1.2].

By using superconducting materials, extremely high current densities and thus magnetic excitations (H) and magnetic density (B) can be achieved at essentially no losses, leading to most compact coil designs and the superior characteristics of SMES systems. Therefore a high specific energy density in no loss condition is achievable. Consequently, the use of the superconducting material can increase the E_v.

A SMES system consists of a superconducting coil, the cryogenic system, and the power conversion or conditioning system (PCS) as the interface of the coil to the power system with control and protection functions. IEEE defines SMES as “A superconducting magnetic energy storage device containing electronic converters that rapidly injects and/or absorbs real and/or reactive power or dynamically controls power flow in an AC system” [1.7]. Such a device has a number of advantages and unique characteristics: no conversion of energy from one form to another is required; consequently SMES has inherently high storage efficiency, a 90% or greater round trip efficiency [1.2]. Depending on the power conversion unit control loop and switching characteristics, the SMES device can respond very rapidly (MWs/milliseconds) to power demands from maximum charge to maximum discharge. SMES systems can offer very reliable and long lifetime service [2.1].

Because of its benefits and unique characteristics, the SMES device is quite competitive with other energy storage technologies; therefore the SMES technology has received considerable attention from electric utilities and the government. Throughout the development of SMES, potential applications were identified, and cost/benefit analyses were carried out [2.1]-[2.4]. Although SMES was initially considered as a diurnal energy storage device, other potential applications can be listed as follows:

- Dynamic and transient stability
- Spinning reserve/ frequency support
- Voltage/VAR support
- Transmission capacity improvement
- Power quality enhancement

2.2. THE COMPONENTS OF THE SMES

A SMES system connected to a power system consists of several subsystems as shown in Figure 2.1. A (usually large) superconducting coil is the heart of the SMES system. It is contained in a cryostat or “Dewar” that includes a vacuum vessel, which prevents massive heat transfer from the surrounding area into the coil. Some smaller SMES coils are totally immersed in the liquid coolant. In larger units, a hollow cable-in-conduit-conductor (CICC) can be used to carry the coolant as in a pipe system. It is worth to point of that for medium sized high temperature superconductors conduct cooling system is also possible and cost effective. The cryogenic auxiliary system provides the coolant and maintains the coil temperature below the critical temperature of the superconductor. A power conversion system is used for two purposes:

1. to convert from DC to AC and
2. to charge and discharge the coil.

A transformer provides the connection to the power system and adjusts the operating voltage to the ideal level for the power conversion system. The centralized control unit manages the system by issuing appropriate commands to local controls of the subsystems.

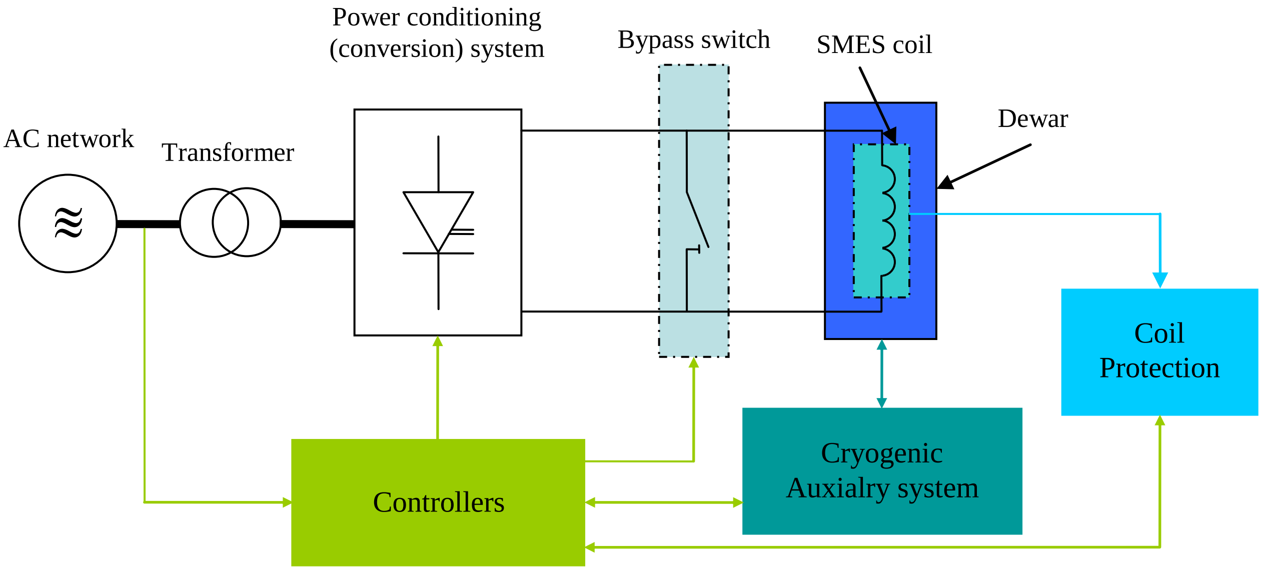

Figure 2.1 Major component of the SMES system (power conversion system can be thyristor base multi-pulse converter, voltage source inverter (VSI) with DC-DC two quadrant chopper, or current source inverter (CSI))

There are two types of superconductors used to form a SMES coil; low temperature superconductors (LTS) and high temperature superconductors (HTS). A composite of alloys of Niobium and Titanium (Nb-Ti) with copper stabilizer is used most commonly for low temperature superconductors (LTS). The use of copper serves several purposes:

- it mechanically supports and separates the individual Nb-Ti filaments,
- electrically isolates the filaments by providing a resistive barrier that reduces losses during charge and discharge, and
- stabilizes the superconductor by conducting current during short periods when the conductor undergoes a transition to the normal state

The HTS material is, at present, bismuth-strontium-calcium copper-oxide (BSCCO), yttrium barium copper oxide coated conductor (YBCO) and most recently magnesium diboride (MgB_2) are investigated for SMES applications [2.1] and [2.4].

For proper operation of the SMES system the magnet coil has to remain superconducting. A refrigerator in the cryogenic system maintains the required temperature for the proper superconducting operation; the operational temperature of LTS magnet is 4.2 K and the operational temperature of HTS material is 15-30 K (for different HTS materials). The refrigeration load can affect the overall efficiency and cost of a SMES system. The refrigeration losses include the losses due to the current lead from room temperature area to cold area, AC current losses of the coil, conduction and radiation losses. These losses should be minimized to achieve a higher efficient and less costly SMES system.

Any abnormal condition that may cause a safety hazard to personnel or damage to the magnet should be detected and protected through the magnet protection system. Monitoring/Protection system may include

1. instruments for monitoring the thermal, structural, and electrical operating conditions of the coil
2. a quench detection system that prevents any temperature to rise above the certain level, and
3. an emergency discharge resistor

SMES is essentially a DC device an appropriate interface must be provided to connect a SMES to an AC power system. A PCS provides a power electronic interface between the AC power system and the superconducting coil. It allows the SMES system to respond within few milliseconds to power demands that could include a change from the maximum charge rate to maximum discharge rate. This rapid response allows a diurnal storage unit to provide spinning reserve and improve system stability [2.1]. The converter/SMES system is highly efficient, as there is no energy conversion from one form to another. Converters may produce harmonics on the AC bus and in the terminal voltage of the coil. Using higher pulse converters can reduce these harmonics. The superconducting coil is charged or discharged by making the voltage across the coil positive or negative [1.1]. The coil absorbs power from the AC system and acts as a load during a half cycle when the converter voltage is positive. During the next half cycle, the coil operates as a generator sending power back into the AC systems when the converter voltage is made negative. When the unit is on standby, independent of storage level, the current is constant, and the average voltage across the superconducting winding is zero. There are two fundamental different interfaces, the voltage source inverter (VSI, see section 3.2.2) and the current source inverter (CSI, see section 3.2.1).

A bypass switch is used to reduce energy losses when the coil is on standby. The utilization of the switch also serves for other purposes such as bypassing DC coil current if utility tie is lost, removing converter from service, and protecting the coil if cooling is lost.

2.3. DESIGN CONSIDERATIONS

In the design stage of a coil, several factors are taken into account to achieve the possible best performance of a SMES system at lower cost. These factors may include coil configuration, energy capability, structure, operating temperature. A compromise is made between each factor considering the parameters of energy/mass ratio, Lorentz forces, stray magnetic field, and minimizing the losses for a reliable, stable and economic SMES system.

2.3.1. Coil configuration: Solenoid vs. Toroid

The solenoid and toroid shaped SMES coils are two main coil designs which have been extensively studied. Solenoid type is simple and easy to construct, and it minimizes the amount of conductor for a given storage capacity [2.5]. However, this type of design results in rather large strays magnetic field [2.5], which may impose some restriction on the site where the SMES can be allocated due to the concerns related to environmental and health effects [1.2], [2.6] and [2.7]; and may require active shielding which increases the needed amount of the superconductor [1.2]. To reduce the stray magnetic field, an alternative was sought, and a toroid coil design was utilized. This design is more complicated to fabricate, and significantly more expensive since it requires the use of more conductors [2.5], [2.6] and [2.8]. According to the evaluation of these designs in [2.5] and [2.9], the solenoid stores almost twice the energy stored in a toroid will be more economical if they are built as solenoids with a height to diameter ratio of about one third and with a maximum field.

For the magnet with small rating in order of the kWh, which is suitable for power quality applications, the solenoid is more cost effective since it is simpler to manufacture, uses less superconductor [2.5] (if the shield is not considered) and allows an easier handling of the electromagnetic stress [1.2]. However, for the larger size magnets the toroid configuration is more advantageous since it is made of small modules which can be produced separately and assembled on site and also offers advantages in terms of stress management. Independently on the rating a toroidal coil must be used if an anisotropic superconductor is considered [2.10]. At the end of a solenoid a significant radial component of the magnetic field produces which creates unacceptable degradation of the wire performance [1.2]. A toroidal winding is hence mandatory for the effective usage of YBCO [2.10].

Solenoid and toroid coils have been used in different variations: single tunnel, multi tunnel, low aspect ratio, single layer and multi-layer structures for solenoid, forced balanced scheme and quasi force free structures for toroids. Due to its simplicity and cost effectiveness, the solenoid type (as shown in Figure 2.2) has been used widely, though the toroid-coil designs were also incorporated by a number of small-scale SMES projects.

The approach for improving the performance of the coil assembly with HTS materials still is an ongoing research activity [2.11].

Figure 2.2 Solenoid type coil with LN_2 reservoir tank [2.12]

2.3.2. Conductor

An appropriate super-conducting section and enough structural and stabilizing material for assuring proper mechanical strength and providing the required protection against quench are necessary. A further requirement is the low AC loss which is particularly important when continuous operation at a high ramp rate is required. A magnetic field in the order of several Tesla for the practical interest of the SMES application to achieve volume energy densities is needed. The magnetic field depends linearly on the total current per unit length. This means that a high enough magnetic field can be obtained either by means of a reduced mass of conductor operating at the large engineering current density or by means of larger mass with a reduced current density [1.2]. Since the volume of the winding usually much smaller than the volume of the bore, a large mass of the conductor does not largely affect the overall volume of the SMES system (and the volumetric energy density, J/m^3). However a large Lorentz force arises in the coil due to high magnetic field. The produced stress distribution because of the magnetic field must be withstood by the material. The minimum mass M of structural material which must be used in order to contain the stress associated with a magnetic energy E can be derived from the Virial theorem as [2.13]

$$M \geq k \frac{\rho}{\sigma} E \tag{2.3}$$

where ρ is the mass density, σ is the allowable stress and k is a coefficient, always ≥ 1, which depends on the geometry of the coil (for a solenoid $k = 1$). If the conductor has adequate strength to satisfy this structural requirement no additional reinforcement is required. Note that equation (2.3) sets a linear dependence of the conductor’s mass with the stored energy. Based on electromagnetic considerations only it can be easily deduced that the minimum mass of material needed to store an energy E in a solenoid operating at given current density scales as $E^{2/3}$ [2.13]. There is a practical limit for the conductor mass for large energy storage because of the structural constraint [1.2]. Furthermore a minimum value of the mass also arises from thermal stability considerations [2.13]. For the passive protection, a minimum total mass of conductor is necessary to have enough heat capacity to absorb all the energy without excessive over-temperature. This limit can be even stricter than the mechanical one [1.2]. If an active protection scheme, (using an external resistor during the quench) considers a more relaxed limit due to stability will obtain. Accurate evaluation of the mass of the conductor is to be calculated case by case by considering the rated energy, possible volume constraints and protection method. Practically using the engineering current densities is not possible because more structural and stabilizing material is needed [2.14]. The optimal choice depends on the cost/performance trade off of the material. If the stored energy increases, a level of stress will occur that the conductor itself is not enough and further reinforcement is required. This can be obtained, even in case of very high storage capacity, by banding the coil with additional structural material integrated in the cold structure [1.2].

2.3.3. Energy storage and availability

Coil inductance (L_c) or PCS maximum voltage (V_{max}) and current (I_{max}) ratings determine the maximum energy/power that can be drawn or injected by the SMES coil. Increasing any of these parameters improves the energy/power capability of the SMES. But, there are other factors that need to be taken into consideration:

- Increasing the I_{max} cause: larger conductor cross section, larger current leads and related lead losses, and larger and more expensive PCS
- Increasing the V_{max} causes: larger and expensive PCS and insulation problems
- Increasing the L_c causes: more turns in the magnet

The density of volumetric energy is proportional to the square of the magnetic field intensity (B). An increase in B has a positive impact in energy density, but causes larger radial and axial stresses that need to be supported with more structural material that induces more cost. A compromise between conductor cost, magnet size and the cost of the structure should be made to determine the optimal B. Also B is depended on the superconducting material and limits with the property of that.

2.4. POTENTIAL SMES APPLICATIONS

A new technology finds its applications if it replaces the existing technology at lower cost or has extraordinary capabilities to serve the needs. SMES system has fast response time and high round trip efficiency. While high round trip efficiency is very important in load leveling, rapid response is a driving factor in power quality applications. On the other hand, the transmission applications such as voltage/VAR control and stabilization relies on the ability of a SMES system to absorb/inject both real and reactive power on alternate cycles. High power/energy ratio is preferred in small-scale SMES systems. In [2.2] wide range of the potential and already studied applications of the SMES is reported. The studied applications cover from low energy - low power to bulk energy storage system [2.13]. Also, several research studies have done or already under development on the hybrid energy storage system with SMES integrated system [1.3] and [2.4].

Extended applications of SMES include transportation systems such as aircraft carrier and naval shipboard power and electric and hybrid-electric vehicles, and electrically sensitive manufacturing and remote energy usage, such as weather research stations, island systems, and ground based defense systems [2.16].

2.5. COMPARISON BETWEEN SMES AND OTHER ENERGY STORAGE SYSTEMS

As with any technology trying to find its widespread acceptance and commercialization, the new technology either has to represent a breakthrough in its functionality and capabilities irrespective to cost, or has to match the performance of a conventional technology at a lower cost. SMES seems to fall in the first category.

Without any doubt, the cost of SMES is currently high, compared to the conventional storage technologies; like as pumped hydro, compressed air, batteries, and flywheel. However, SMES systems have a unique advantage in two types of application. The first type is the transmission control and stabilization since SMES can respond to power demand very fast and can handle high power demand for longer periods. The second type is the power quality application where SMES can easily be sited near industrial loads [1.2].

2.6. REVIEW PAST AND PRESENT STATE OF THE ART OF THE SMES

In 1970 SMES technology has been introduced for bulk energy storage and management system by Ferrier. He presented a single, large, centrally located SMES unit to satisfy all of the cyclic power requirements for the French utility. This idea was not pursued due to high capital and development costs.

Based on the nowadays state art of the technology application of the SMES for that range of the energy is not cost competitive. It is estimated that MWh-GWh class SMES could become viable in the long term scenario [2.1]. SMES applications such as power quality and frequency stabilization have potential to be technically and economically favorable in near and/or medium term. Nb-Ti conductors operating at 4.2 K have been mainly considered so far in the SMES development [1.1]. A 10 MVA/30 MJ SMES with Nb-Ti has been built and submitted to long term real grid test in 1983 [2.17]. Since 1980s many other prototypes for power quality applications, with a rated power in the range 0.1-10 MW and usable energy in the range 0.2-10 MJ, have been built worldwide

[2.18]-[2.23] and have been submitted to successful laboratory tests as well as to live grid tests [2.18] and [2.23].

More recently HTS conductors have also been considered. In particular SMES prototypes with rated energy in the range 0.6-1.0 MJ have been developed based both on Bi2212 and Bi2223 conductors [2.23]-[2.25]. However, despite the higher critical temperature, an operating temperature of 4.2 K has been chosen in order to reduce the amount of conductor needed [2.23]-[2.25] (an operating temperature of 20 K is chosen in [2.26] where the SMES is developed for special purposes). Indeed the high cost of the material does not seem to offer favorable conditions for future development of SMES based on first generation HTS conductors. Substantial cost reduction is instead expected in the near future for second generation HTS conductors. Research projects for the development of high field/high energy density SMES based on YBCO coated conductors are in progress [2.23], [2.25], [2.27] and [2.28]. In particular the design of a 100 MW / 2 GJ class SMES system for frequency stabilization has been carried out based on high performance YBCO tape operating at 20K - 11T [2.27]. A small unit coil has been built as a first step in establishing the technology [2.23]. Furthermore a challenging 20 kW / 3.2 MJ SMES demonstrator based on YBCO operating at 4.2 K - 25 T is under development [2.28]. Investigation into the feasibility of SMES based on MgB_2 is also in progress. An operating temperature of 20 K is considered for allowing combined use with liquid hydrogen technology [2.4] and [2.29]. At the present MgB_2 has a lower cost compared to YBCO. However, it has a lower critical field; therefore the volume energy density is limited. This means that larger windings are needed, which translates in more demanding cryogenics.

2.7. REFERENCES

[2.1] S. Nomura, T. Shintomi, S. Akita, T. Nitta, and S. Meguro “Technical and Cost Evaluation on SMES for Electric Power Compensation,” IEEE Transactions on Applied Superconductivity, Vol. 20, No. 3, June 2010, pages 1373-1378, DOI: 10.1109/TASC.2009.2039745

[2.2] M. H. Ali, Bin Wu, and R. A. Dougal “An Overview of SMES Applications in Power and Energy Systems,” IEEE Transactions on Applied Superconductivity, VOL. 1, No. 1, April 2010, pages 38-47, DOI:10.1109/TSTE.2010.2044901

[2.3] X. Y. Chen, J. X. Jin, Y. Xin, B. Shu, C. L. Tang, Y. P. Zhu, and R. M. Sun, “Integrated SMES Technology for Modern Power System and Future Smart Grid,” IEEE Transactions on Applied Superconductivity, Vol. 24, NO. 5, October 2014, DOI: 10.1109/TASC.2014.2346502

[2.4] M. Sander, R. Gehring, and H. Neumann “LIQHYSMES—A 48 GJ Toroidal MgB2-SMES for Buffering Minute and Second Fluctuations,” IEEE Transactions on Applied Superconductivity, Vol. 23, No. 3, JUNE 2013, DOI: 10.1109/TASC.2012.2234201

[2.5] M. Watanabe, S. Ishiguri, R. Maruyama, M. Yamaguchi, S. Fukui, J. Ogawa, and T. Sato “A Study on High Temperature Superconducting Coil of Different Coil Arrangements,” IEEE Transactions on Applied Superconductivity, Vol. 17, No. 2, June 2007, pages: 2002-2005, DOI: 10.1109/TASC.2007.898425

[2.6] W. Hassenzahl, “A comparison of the conductor requirements for energy storage devices made with ideal coil geometries,” IEEE Transactions on Magnetics, Vol.25, No.2, pages: 1799-1802, March 1989, DOI:10.1109/20.92651

[2.7] R.F. Giese, “Progress toward High Temperature Superconducting Magnetic Energy Storage (SMES) – A Second Look,” Argonne National Laboratory, December 1998

[2.8] D. Lieurance, F. Kimball, C. Rix, C. Luongo, “Design and Cost Studies for Small Scale Superconducting Magnetic Energy Storage Systems,” IEEE Transactions on Applied Superconductivity, Vol. 5, No. 2, June 1995, pages: 350-353, DOI: 10.1109/77.402561

[2.9] R.W. Boom and H.A. Peterson, “Superconductive Energy storage for Power Systems,” IEEE Transactions on Magnetics, vol. MAG-8, pages: 701-703, September 1972, DOI: 10.1109/TMAG.1972.1067425

[2.10] Y. Oga, S. Noguchi, and M. Tsuda “Comparison of Optimal Configuration of SMES Magnet Wound With MgB2 and YBCO Conductors,” IEEE Transactions on Applied Superconductivity, Vol. 23, No. 3, June 2013, DOI: 10.1109/TASC.2012.2231452

[2.11] S. Ishiguri and D. Kiuchi “Performance Improvement and Optimization of New High-Temperature Superconducting Coil Assembly,” IEEE Transactions on Applied Superconductivity, Vol. 24, No. 2, April 2014, DOI: 10.1109/TASC.2013.2292120

[2.12] Magnet cutaway, online availabel at: http://nmr.chem.umn.edu/cutaway.html

[2.13] W. V. Hassenzahl, D. W. Hazelton, B. K. Johnson, P. Komarek, M. Noe, and C. T. Reis “Electric Power Applications of Superconductivity,” Proceedings of the IEEE, Vol. 92, No. 10, OCTOBER 2004, pages 1655-1674, DOI: 10.1109/JPROC.2004.833674

[2.14] P. Tixador, N. T. Nguyen, J. M. Rey, T. Lecrevisse, V. Reinbold, C. Trophime, X. Chaud, F. Debray, S. Semperger, M. Devaux, and C. Pes “SMES Optimization for High Energy Densities,” IEEE Transactions on Applied Superconductivity, Vol.22, No.3, June 2012, DOI : 10.1109/TASC.2011.2175870

[2.15] A. B. Arsoy, Z. Wang, Y. Liu, and P. F. Ribeiro “Transient Modeling and Simulation of a SMES Coil and the Power Electronics Interface,” IEEE Transactions on Applied Superconductivity, Vol. 9, NO. 4, December 1999, pages 4715-4724, DOI: 10.1109/77.819343

[2.16] A. Morandi, L. Trevisani, F. Negrini, P. L. Ribani, and M. Fabbri “Feasibility of Superconducting Magnetic Energy Storage on Board of Ground Vehicles with Present State-of-the-Art Superconductors,” IEEE Transactions on Applied Superconductivity, Vol. 22, No. 2, April 2012, DOI: 10.1109/TASC.2011.2177266

[2.17] H. J. Boenig, J. F. Hauer “Commissioning Tests of the Bonneville Power Administration 30 MJ Superconducting Magnetic Energy Storage Unit,” IEEE Transactions on Power Apparatus and Systems, vol. PAS-104, No. 2, February 1985, pages: 302-312, DOI: 10.1109/TPAS.1985.319044

[2.18] W. Buckles and W. Hassenzahl, “Superconducting magnetic energy storage,” IEEE Power Engineering Review, Vol. 20, pages: 16–20, May 2000, DOI: 10.1109/39.841345

[2.19] K.-P. Juengst, R. Gehring, A. Kudymow, G. Kuperman, and E. Suess “25 MW SMES-Based Power Modulator,” IEEE Transactions on Applied Superconductivity, Vol. 12, NO. 1, MARCH 2002, pages: 758-761, DOI: 10.1109/TASC.2002.1018512

[2.20] L. Ottonello, G. Canepa, P. Albertelli, E. Picco, A. Florio, G. Masciarelli, S. Rossi, L. Martini, C. Pincella, A. Mariscotti, E. Torello, A. Martinolli, and M. Mariani, “The Largest Italian SMES,” IEEE Transactions on Applied Superconductivity, Vol. 16, No. 2, June 2006, pages: 602-607, DOI: 10.1109/TASC.2005.869677

[2.21] H. J. Kim, K. C. Seong, J. W. Cho, J. H. Bae, K. D. Sim, S. Kim, E. Y. Lee, K. Ryu, and S. H. Kim, “3 MJ/750 kVA SMES system for improving power quality,” IEEE Transactions on Applied Superconductivity, Vol. 16, No. 2, June 2006, pages: 574–577, DOI: 10.1109/TASC.2006.871329

[2.22] A. Morandi, M. Breschi, M. Fabbri, F. Negrini, R. Penco, M. Perrella, P. L. Ribani, M. Tassisto, and L. Trevisani, “Design, manufacturing and preliminary tests of a conduction cooled 200 kJ Nb-Ti µSMES,” IEEE Transactions on Applied Superconductivity, Vol. 18, No. 2, pages: 697-700, 2008, DOI:10.1109/TASC.2008.921285

[2.23] S. Nagaya, N. Hirano, T. Katagiri, T. Tamada, K. Shikimachi, Y. Iwatani, F. Saito, Y. Ishii "The state of the art of the development of SMES for bridging instantaneous voltage dips in Japan," Cryogenics, Volume 52, Issue 12, December 2012, pages 708-712, DOI:10.1016/j.cryogenics.2012.04.014

[2.24] L. Xiao and L. Lin "Recent Progress of Power Application of Superconductor in China," IEEE Transactions on Applied Superconductivity, Vol. 17, No. 2, June 2007, pages 2355-2360, DOI: 10.1109/TASC.2007.898160

[2.25] M. Park, S. Kwak, W. Kim, J. Lee, J. Han, K. Choi, H. Jung, J. Bae, S. Kim, K. Sim, H. Kim, K. Seong, and S. Hanh "Conceptual Design of HTS Magnet for a 5 MJ Class SMES," IEEE Transactions on Applied Superconductivity, Vol. 18, No. 2, June 2008, pages: 750-753, DOI: 10.1109/TASC.2008.922533

[2.26] P. Tixador, B. Bellin, M. Deleglise, J. C. Vallier, C. E. Bruzek, A. Allais, and J. M. Saugrain, "Design and first tests of a 800 kJ HTS SMES," IEEE Transactions on Applied Superconductivity, Vol. 17, No. 2, June 2007, pages: 1967–1972, DOI: 10.1109/TASC.2007.898520

[2.27] K. Shikimachi, N. Hirano, S. Nagaya, H. Kawashima, K. Higashikawa, and T. Nakamu, "System coordination of 2 GJ class YBCO SMES for power system control," IEEE Transactions on Applied Superconductivity, Vol. 19, No. 3, June 2009, pages: 2012-2018, DOI: 10.1109/TASC.2009.2018491

[2.28] Q. Li, D.W. Hazelton, V. Selvamanickam, and T.F. Lehner, "Superconducting Magnetic Energy Storage (SMES) Systems for GRIDS," The 10th EPRI Superconductivity Conference, October 11-13, 2011, Tallahassee, FL, USA, Online availabe at: http://goo.gl/0lEBQy

[2.29] T. Shintomi, T. Asami, G. Suzuki, N. Ota, T. Takao, Y. Makida, T. Hamajima, M. Tsuda, D. Miyagi, M. Kajiwara, and J. Hirose "Design Study of MgB2 SMES Coil for Effective Use of Renewable Energy," IEEE Transactions on Applied superconductivity, Vol. 23, No. 3, June 2013, DOI: 10.1109/TASC.2012.2234181

3. POWER ELECTRONICS CONVERSION/CONDITIONING AND CONTROL OF THE SMES SYSTEM

Power electronics can be defined as the use of solid state devices to control and convert/process electric power. It supplies voltages and currents in a form that is desirable for user loads [3.1]. As a consequence of the advances in power electronics technology, power electronics has found its applications in power system, spreading out to all voltage levels [3.2].

The power electronics interfaces between a superconducting coil and the AC power system; and it is called a SMES power conversion/conditioning system (PCS). A PCS is expected to transfer energy into or out of the SMES on command, to control real and reactive power, and to be able to bypass the coil when there is no need for energy into or out of the coil [3.3].

Different converter/inverter topologies have been developed to operate SMES. Different factors such as semiconductor device types, switching technologies, converter system configuration and reactive power requirement have been considered / evaluated for the PCS design. These factors will be addressed in the following sections.

3.1. SEMICONDUCTOR DEVICE TYPES

Power semiconductor devices are the main part of the power electronics circuit. The appropriate selection of a device affects the reliability and efficiency of the overall system. In choosing the appropriate device several factors are important [3.1]:

- device cost
- rugged operation, modularity and reliability
- current and voltage ratings of the device
- switching frequency of the device
- low switching and conduction loss of the device

Line commutated power electronic switches have been initially used in power conversion of SMES systems, they were replaced by high power self-commutated semiconductor devices, which offers more controllability and flexibility. The present viable devices for high power applications between all of the possible devices are gate turn off thyristor (GTO), insulated gate bipolar transistor (IGBT) and integrated gate commutated thyristor (IGCT). Also, using emitter turn off thyristor (ETO) for high power application is studied in [3.3]; however, serial MOSFET for controlling the gate signal of the thyristor is a possible limitation for high current applications.

A ***GTO*** is a four-layer thyristor with a turn-off capability. Current is conducted by applying a positive gate signal and positive voltage, and is terminated by applying a negative gate signal. To provide the energy to turn-on and off functions, a snubber circuit is used. For high power applications, excessive voltages are produced during turn-off, therefore the snubber parameters should be selected carefully. GTOs have been developed in during 1980s. Their current and voltage handling capabilities are very high, but they have slower switching speeds, higher losses and higher costs than conventional forced commutated thyristors.

An ***IGCT*** is an improved GTO device. Its substantial improvements include the low inductance gate drive, raggedness of thyristors, the change of turn-off process (hard switching) and the inverse diodes. The IGCT technology offers higher switching rates of transistors, and reduced switching losses. The higher rate of gate current change vastly improves minimum on and off times. More uniform turn-on characteristics and faster turn-off times make IGCT devices ideal for series connection without significant derating or parametric selection.

An ***IGBT*** is a device that is part way to being a thyristor, part way to latching stays as a transistor. It contains an integrated MOS structure with insulated gate. They are fairly new development for high power applications. Like transistors, they potentially have the ability to limit current flow by controlling the gate voltage. Their turn-on and turn-off actions are faster, but their power handling capability is lower than GTOs and IGCTs.

3.2. POWER ELECTRONICS CONVERTER TYPES FOR SMES

Two basic types of inverters, current-sourced inverters (CSI) or voltage-sourced inverters (VSI) are commonly used for the power conversion unit between SMES and AC power system. Basic concepts of these inverters are schematically drawn in Figure 3.1. From this figure, it seems that a CSI is more appropriate for SMES applications since SMES is also a current source. But, there are applications where VSI based FACTS controllers (or custom power devices) are used in power systems, and attachment of SMES devices can improve the effectiveness and capability of the overall system. Both CSI and VSI will describe in the next subsections with their circuit topologies, switching schemes and applications.

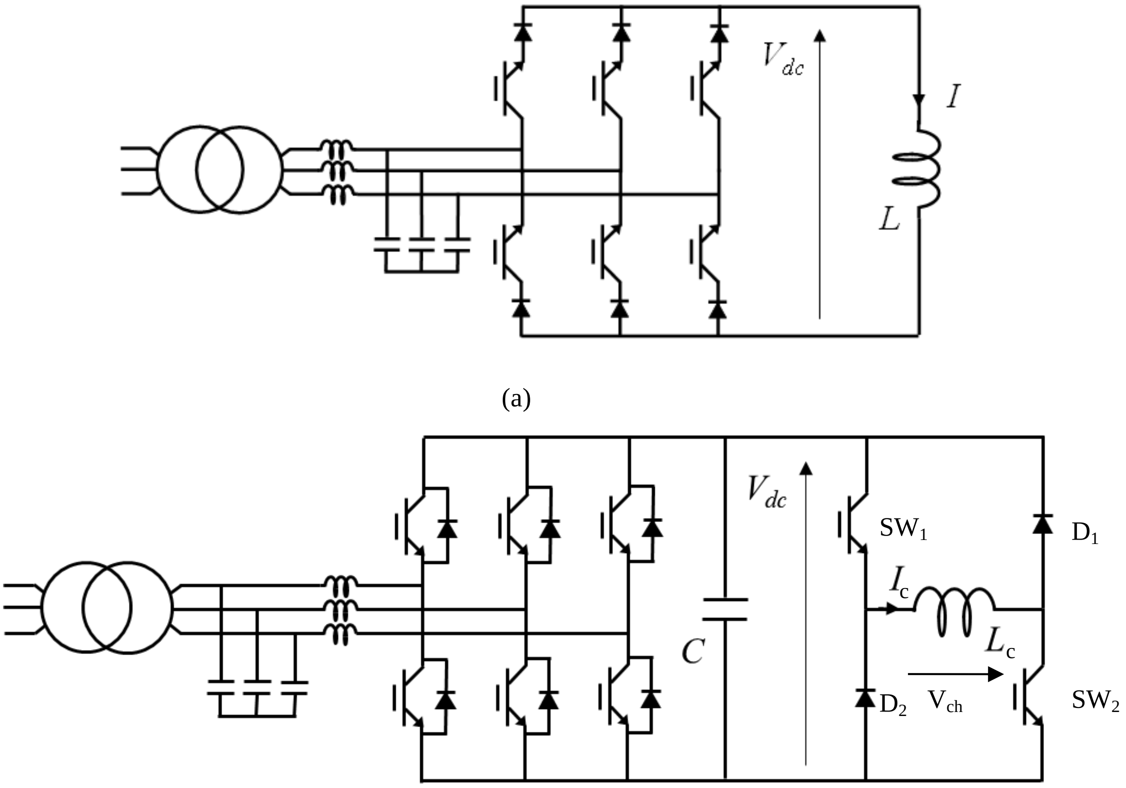

(a)

(b)

Figure 3.1 Basic concepts of Voltage and source inverter for SMES application, (a) current source inverter (b) voltage source configuration

3.2.1. Current source inverter

As can be seen from Figure 3.1 (a), a CSI consists of a power electronics block a large inductance on the DC side, and capacitor or filter on the AC side. While the inductor maintains constant DC current, AC capacitors provide a stiff AC bus for supplying the fast changing current pulses needed for the commutations. The DC current flow is maintained in one direction, and the power flow direction can be changed by reversing the DC voltage. The power electronic block can be either a line commutated diode based, or line commutated thyristor based or self-commutated turn-off devices.

By this configuration, independent control of real and reactive power in a wide range and fast response can be achieved by using turn off devices. Harmonics can be eliminated using PWM scheme. A fast response and wide range power controllability are essential for the stabilizing mode of SMES [3.5] and [3.6].

The operating principle of a 3-phase 6-pulse CSI (see Figure 3.1 (a)) consisting of thyristor or turn-off devices controlled by a firing circuit can be explained as follows: positive gate signal initiates the current conduction at a prescribed time and 20ms (one cycle of power frequency of 50 Hz) sequence to maintain the desired average voltage across the coil. By changing the firing angle (α), the variation between the maximum positive value and the maximum negative value of voltage across the coil (V_c) can be obtained. The average voltage and real and reactive powers (P and Q) are expressed as follows:

$$\begin{aligned} V &= V_c \cos(\alpha) \\ P &= P_c \cos(\alpha) \\ Q &= Q_c \cos(\alpha) \end{aligned} \tag{3.1}$$

3.2.2. Voltage source inverter

A VSI is consist of turn-off device based converter, a DC link capacitor, and inductance on the AC side. The large capacitance ensures that the voltage is unipolar. It also handles sustained charge/discharge current. An inductive interface is needed to ensure that the DC link capacitor is not short-circuited. It should be noted that the VSI must have bidirectional valves (combination of a turn-off device and diode) to allow current flow in either direction. Furthermore, there is no need for reverse voltage capability of the turn-off devices, since the DC voltage does not reverse [3.1].

A three phase two level VSI (see Figure 3.1 (b)) operates by turning on or off per device per cycle. The AC output voltage can be controlled by varying the width of the voltage pulses, and/or the amplitude of the DC bus voltage. Due to the nature of converters, harmonics are present. To reduce harmonic magnitude, either a multi-pulse VSI with 180-degree conduction or a three phase PWM scheme are utilized [3.1].

The VSI and the chopper are linked by a DC link capacitor that behaves as a stiff, but a controllable DC voltage source providing the desired characteristics. A three-phase VSI and single-phase chopper connection is illustrated in Figure 3.1 (b). VSI can provide continuous rated capacity VAR support even at low or no coil current, whereas CSI is dependent of the coil current in providing VAR support.

Independent control of active and reactive power can be obtained by means of proper control of the inverter. A capacitor is used as intermediate (low capacity) storage element for leveling the voltage of the DC bus. The state of charge of the capacitor is regulated by SMES which continuously inject or extract current from the DC bus by means of a PWM controlled chopper.

Since, CSI is not commonly used for utility applications of this kind because, as opposed to VSI, their reactive power capability is proportional to the SMES coil current. Further, the implementation of a CSI is more complex than that of a VSI, particularly because of potential over-voltage problems due to stray inductances and the need for an AC side capacitive filter [1.1]. Table 3.1 summarizes the differences between VSI and CSI, in this table advantage of each configuration is bolded. It is worth to point out that the active power capability of a CSI is equal to that of a VSI, where the active power of these configurations are dependent to the stored energy in the coil and it is independent to the PCS configuration.

Table 3.1. Comparison between voltage and current source inverter (VSI and CSI) [1.1]

Issue	VSI	CSI
Reactive power	**Always full range available (no coil needed)**	Minimum capacitive, but full range dependent on coil current
Capacitor	DC	AC
Device	**Asymmetrical**	Symmetrical (series diode)
AC system control	Complex	**Easy, since decupled**
di/dt fault current	High	**Low**
Implementation	**Easy**	Complex
Losses (inverter only)	**Lower**	Higher

The detail operation of the VSI configuration discusses here. Two switching devices (SW_1 and SW_2) in the DC-DC chopper are switched on and off simultaneously and creating the voltage across the SMES coil as illustrated in Figure 3.2. Changing the duty cycle D of their switching pattern can control the DC component of this voltage as follows:

$$\bar{V}_{\mathrm{CH}} = (1-2D)V_{\mathrm{dc}} \tag{3.2}$$

This is in turn will cause the average value of the coil current to change over time, according to:

$$\frac{\mathrm{d}I_{\mathrm{c}}}{\mathrm{d}t} = -\frac{\bar{V}_{\mathrm{CH}}}{L_{\mathrm{c}}} \tag{3.3}$$

where L_c is the total coil inductance. The freewheeling diodes (D_1 and D_2) ensure the continuous current flow through the coil while SW_1 and SW_2 are off. According to the equation (3.3), the energy flow into the SMES coil is as follows:

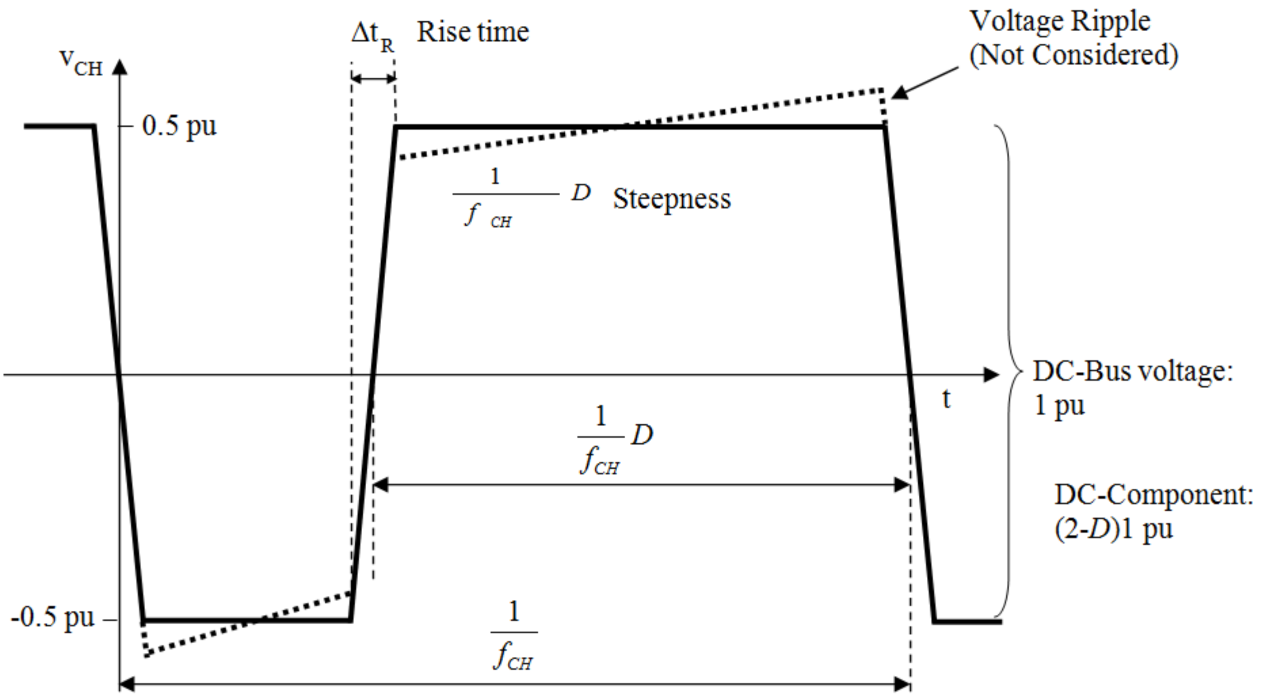

Figure 3.2 Simplified voltage signal imposed onto the SMES coil by chopper operating at constant frequency f_{CH} and duty cycle D [1.1]

$D = 0.5$	$\frac{dI_c}{dt} = 0$	No net energy transfer → Stand by
$D > 0.5$	$\frac{dI_c}{dt} < 0$	Energy transfer out of the coil → Discharge
$D < 0.5$	$\frac{dI_c}{dt} > 0$	Energy transfer into the coil → Charge

For reducing both the step change in voltage during switching and the current requirements for each switch, multilevel and multiphase chopper arrangements have been proposed previously. A small inductor is placed at the output of each chopper phase in multiphase DC-DC choppers to allow current sharing. For eliminating the low order ripple frequencies in the chopper output voltage and input current, where the lowest ripple frequency is the chopper switching frequency times the number of chopper phases, using either fast switching devices or a multiphase chopper is preferable [1.1].

Although the DC-DC chopper can serve the entire region of operation between charge and discharge, a dedicated bypass switch may be adopted in order to [1.1]:

- energy loss reduction during the standby operation of the coil
- bypass the DC coil current if the utility tie is lost
- remove the AC side converter from service and protect the coil if cooling is lost

Placing such a bypass switch within the cryogenic environment of the SMES coil would further reduce the standby losses. However, at present, no feasible technology is available to enable high-power, silicon-based cryogenic switching devices [1.1].

3.2.3. Hybrid integration of the SMES with other technologies

Currently installed FCATS controllers (or custom power devices) in the power system are using VSI interface and it is logical to integrate the SMES system in the DC bus of these controllers. Integrating SMES with multi MVA level FACTS controller make it possible to provide independent real power control without a large increase in the MVA rating of the converter [3.7]. Since the SMES has fast response and high round trip efficiency for the short round trip duration, integrating SMES with other storage technology (e.g. batteries, fuel cells [3.8] and [3.9]) and distributed generation (e.g. PV arrays and wind generators [2.29]) at the DC link could have complementary characteristic to those technologies.

3.3. REFERENCES

[3.1] N. Mohan, T.M. Undeland, W.P. Robbins, "Power Electronics Converters, Applications and Design 3rd edition," John Wiley, New York, 2003, ISBN: 978-0-471-22693-2

[3.2] J. D. van Wyk, and F. C. Lee, "On a Future for Power Electronics," IEEE Journal OF Emerging and Selected Topics in Power Electronics, Vol. 1, No. 2, JUNE 2013, pages: 59-72, DOI: 10.1109/JESTPE.2013.2271499

[3.3] M. G. Molina, P. E. Mercado, and E. H. Watanabe, "Improved Superconducting Magnetic Energy Storage (SMES) Controller for High-Power Utility Applications," IEEE Transactions on Energy Conversion, Vol. 26, No. 2, June 2011, pages: 444-456, DOI: 10.1109/TEC.2010.2093601

[3.4] X. Shi , S. Wang , W. Yao, A. Waqar, W. Zuo, and Y. Tang, "Mechanism Analysis and Experimental Validation of Employing Superconducting Magnetic Energy Storage to Enhance Power System Stability," Energies, Vol. 8, No. 1, 2015, pages: 656-681; DOI: 10.3390/en8010656

[3.5] Z. Wang, K. T. Chau, B. Yuwen, and F. Li, "Power compensation and power quality improvement based on multiple-channel current source converter fed HT SMES," IEEE Transactions on Applied Superconductivity, Vol. 22, No. 3, June 2012, DOI: 10.1109/TASC.2011.2174573

[3.6] Z. Wang, L. Jiang, Z. Zou, and M. Cheng, "Operation of SMES for the Current Source Inverter Fed Distributed Power System under Islanding Mode," IEEE Transactions on Applied Superconductivity, Vol. 23, No. 3, June 2013, DOI: 10.1109/TASC.2012.2232703

[3.7] F. Ribeiro, B. K. Johnson, M. L. Crow, A. Arsoy, and Y. Liu, "Energy Storage Systems for Advanced Power Applications," Proceedings of the IEEE, Vol.89, No.12, pages: 1744-1756, Dec 2001, DOI: 10.1109/5.975900

[3.8] T. Ise, M. Kita, and A. Taguchi, "A Hybrid Energy Storage With a SMES and Secondary Battery," IEEE Transactions on Applied Superconductivity, Vol. 15, No. 2, June 2005, pages: 1915-1918, DOI:10.1109/TASC.2005.849333

[3.9] H. Louie, and K. Strunz “Superconducting Magnetic Energy Storage (SMES) for Energy Cache Control in Modular Distributed Hydrogen-Electric Energy Systems,” IEEE Transactions on Applied Superconductivity, Vol. 17, No. 2, June 2007, pages: 2361-2364, DOI: 10.1109/TASC.2007.898490

4. SMES COIL DESIGN

4.1. SUPERCONDUCTING CONDUCTOR AND CABLE

Since the high temperature superconducting (HTS) materials show the performance of these materials for power system applications with less operating cost, in the rest of this thesis HTS material and specially both second generation HTS materials (2G HTS i.e. YBCO coated conductors) and MgB_2 are considered in the design of the coil. In particular the design of the SMES is carried out based on the two commercially available conductors whose characteristics are listed in Table 4.1 and Table 4.2. The engineering current density of the two conductors in the temperature range between 16 K and 24 K is plotted in Figure 4.1 as a function of the magnetic field. In the case of YBCO the field orientation is perpendicular to the tape. Data of Figure 4.1 are taken from [4.1] for YBCO and from [4.2] for MgB_2. The critical engineering current density of the YBCO conductor corresponding to a generic orientation θ can be expressed as follows [4.3]:

$$J_e(B,T,\theta) = J_e(B,T,0)\, f(\theta) \tag{4.1}$$

where $\theta = 0$ corresponds to the orientation perpendicular to the tape. Function $f(\theta)$ is referred to as a lift factor. The lift factor of the considered YBCO tape is reported in Figure 4.2 [4.4]. Data shown are obtained with an applied field of 5 T. It is worth to point out that the dependence of the lift factor of YBCO on the applied field is reported in the literature [4.3]-[4.6], especially at low temperature. However, as a first approximation, this dependence is not considered in the following. In the case of MgB_2 an isotropic behavior is observed, therefore no dependence of J_e on the field orientation needs to be specified. This means that the equation (4.1) with $f(\theta) = 1$ is to be used.

A solenoid layout is considered for the SMES coil. The required current capacity is in the order of a few kA. This means that more conductors must be placed in parallel in order to assemble a cable with an appropriate current capacity for the manufacturing of the solenoid. A Rutherford assembly is considered for the case of the MgB_2 wires. Feasibility of multi-strand Rutherford cables made of MgB_2 round wires has been demonstrated [4.7]. Multi-layers solenoid coils made of Rutherford cables are routinely manufactured. Instead a Roebel assembly is considered for the YBCO tapes [4.8]. Multi-layers solenoid coils made by YBCO Roebel cable has been recently manufactured for transformer applications [4.9]. It is worth to point out that for assembling the YBCO tapes in a Roebel cable a meander-like form must first be obtained for each of them by mechanical punching which produce scraps [4.8]. Indeed, only half of the tape is actually exploited.

Table 4.1. Main characteristics of the MgB_2 conductor

Manufacturer	Columbus
Type	round wire
Nominal radius	1.13 mm
Filling factor	0.14
Matrix	Ni 70%, Copper 20 %
Critical tensile strength	300 MPa
Critical current, 16 K – 3 T	200 A

Table 4.2. Main characteristics of the YBCO coated conductor

Manufacturer	Superpower
Type	flat tape
Nominal Width	12 mm
Nominal thickness	0.1 mm
YBCO thickness	1 μm
Stabilizer (Copper)	2×20 μm
Substrate (Hastelloy)	100 μm
Critical tensile strength	550 MPa
Critical current, 16 K – 3 T (perp)	1019 A

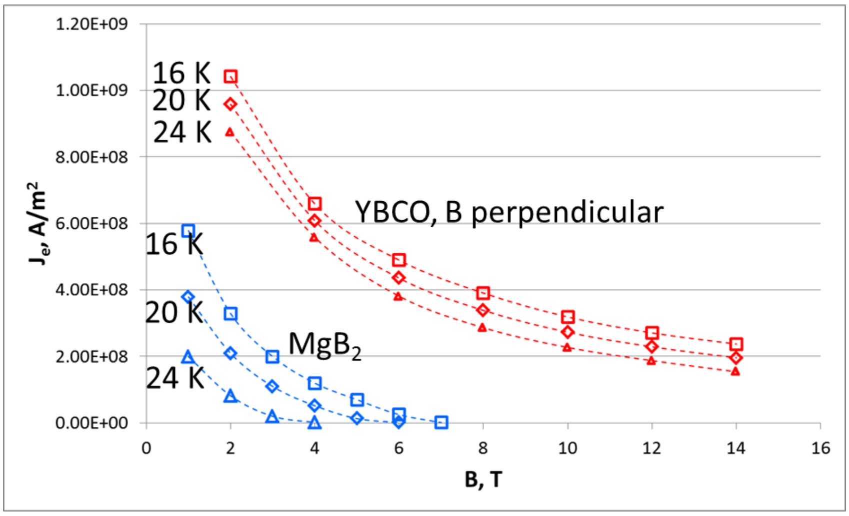

Figure 4.1 Engineering critical current density versus applied field of the MgB_2 and the YBCO conductor in the range 16 K – 24 K

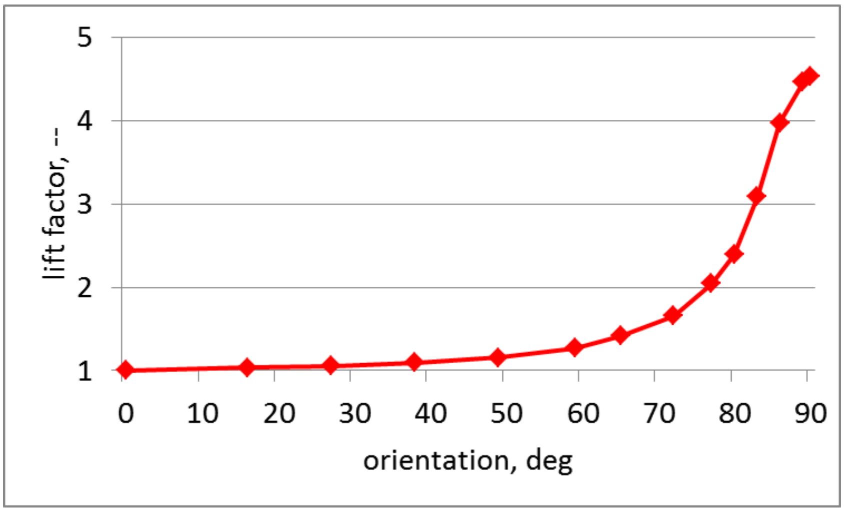

Figure 4.2 Lift factor $f(\theta) = J_e(B,T,\theta) / J_e(B,T,0)$ of YBCO conductor

4.2. ELECTROMAGNETIC DESIGN OF THE SC COIL

A solenoid geometry is considered for the SC coil. For the stored energies in the MJ range this is the most cost effective geometry and also has the highest Joule/ampere-turn ratio, which minimizes the amount of material needed [4.10]. The solenoid is made of multiple pancakes stacked in the axial direction [2.26], [4.11] and [4.12]. In order to carry out the electromagnetic design the input parameters listed in Table 4.3 are preliminary chosen.

Table 4.3. Input parameters for the design of the SC coil

Aspect ratio of the solenoid, a	*Length to diameter ratio*
Filling factor of the solenoid, b	*Fraction of the cross section filled with SC conductor. This takes into account both the filling factor of the SC cable (Rutherford, Roebel) and the electrical insulation.*
J/J_c ratio of the SC conductor, c	*Safety factor*
Operating temperature of the superconductor, T	
SC material, MgB_2 or YBCO	
Reference field of the solenoid, B_{ref}	*Approximate field (axial component at the center) which is intended to be produced by the solenoid at the maximum current during normal operation*

The layout of the solenoid is arrived at by means of the design procedure which consists of the following steps.

4.2.1. Step one

The volume V_{bore} of the solenoid bore is obtained based on the energy ΔE to be delivered and the energy density $e = B_{\text{ref}}^2/2\mu_0$ corresponding to the reference field by means of equation (4.2). The inner diameter D_{sol} and the height H_{sol} of the solenoid are obtained accordingly by considering the aspect ratio a

$$\begin{aligned} V_{\text{bore}} &= 2\mu_0\,\Delta E / B_{\text{ref}}^2 \\ D_{\text{sol}} &= (4V_{\text{bore}}/a\pi)^{1/3} \\ H_{\text{sol}} &= aD_{\text{sol}} \end{aligned} \qquad (4.2)$$

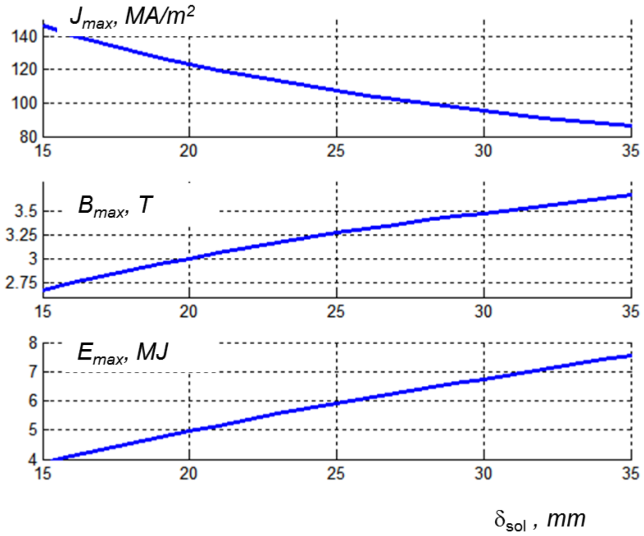

Figure 4.3 Dependence of J_{max}, B_{max} and E_{max} on the thickness δ_{sol} of the solenoid for the 3 T - MgB_2 SMES

4.2.2. Step two

Given a thickness δ_{sol} of the solenoid, the magnitude B of the magnetic field at a given point is proportional to the current density of the solenoid via the geometric coefficient k which changes from point to point, i.e. $B = k(P)\,J$. The orientation θ of the field also changes from point to point, but is independent of the current density. The critical current density of the SC conductor at the given point P is obtained by intersecting the load line of the coil with the actual J_e vs. B curve, that is by solving

$$J_e(B,0)\,f(\theta(P)) = \frac{1}{b}\frac{B}{k(P)} \qquad (4.3)$$

where b is the filling factor of the solenoid (see Table 4.3). The critical current density J_c of the solenoid is by definition the minimum critical current density found on the conductor; therefore it can be arrived at by solving equation (4.3) at a discrete set of points within the cross section of the solenoid and by taking the minimum of the values found. In practice, in case of MgB_2 ($f(\theta) = 1$) this minimum occurs at the innermost point in the middle of the solenoid, where the maximum magnitude of the field is obtained, whereas in case of YBCO this minimum occurs at the ends of the solenoid where the perpendicular (radial) component is stronger. Finally, the maximum allowable current density of the SC conductor is obtained as $J_{max} = c\,J_c$, where c is the allowable J/J_c ratio (see Table 4.3). The maximum allowable field B_{max} at the center of the solenoid is deduced based on J_{max}. The maximum energy E_{max} storable by the solenoid is also deduced based on J_{max}. As an example the dependence of J_{max}, B_{max} and E_{max} on the thickness of the solenoid is plotted in Figure 4.3 in the case of the 3 T - MgB_2 SMES.

The length of SC conductor needed to build up the solenoid with thickness δ_{sol} is given by equation (4.4) where S_{SC} is the cross section of the conductor and R_m is the average radius of the solenoid ($R_m = D_{sol}/2 + \delta_{sol}/2$). The amount of superconductor needed for the 3 T - MgB_2 SMES is plotted in Figure 4.4 as a function of the maximum storable energy. A drastic increase of the length of SC conductor can be observed with E_{max} in this case. Though substantial, the increase is less drastic in case of YBCO at 3 T.

$$length_{SC} = 2\pi R_m\, b H_{sol} \delta_{sol} / S_{SC} \qquad (4.4)$$

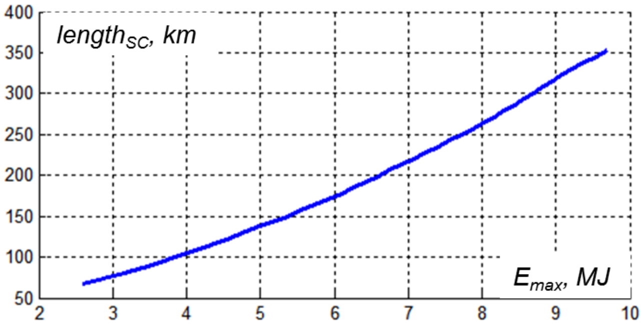

Figure 4.4 Length of SC conductor needed for the solenoid as a function of the maximum storable energy E_{max} for the 3 T - MgB_2 SMES

4.2.3. Step three

A Lorentz force arises in the coil due to the magnetic field. This produces a stress distribution which must be withstood by the superconductor. The maximum tensile stress occurring on the superconductor in the case of thick solenoid can be estimated by means of equation (4.5), where r is the ratio between the outer and the inner diameter of the solenoid, that is ($r = 1 + 2\delta_{sol}/D_{sol}$) [4.13]. For the designed coil to be acceptable from the mechanical point of view the maximum stress should be well below the critical tensile stress of the considered superconductors reported in Table 4.1 and Table 4.2. If this condition is not fulfilled banding of the solenoid with additional structural material needs to be taken into account, but this option is not considered here.

$$\sigma_{max} = \frac{1}{2} J_{max} B_{max} D_{sol} \frac{1}{r-1}\left[\frac{2r(7r^2+r+1)}{9(r+1)} - \frac{5}{12}(2r^2+r-\frac{3}{5})\right] \tag{4.5}$$

4.2.4. Step four

The last step for the design of the solenoid is the choice of the number of turns N. This is a crucial parameter since it affects the inductance L_c, and hence the operating conditions of the solenoid. The maximum current I_{max} and the deliverable energy ΔE of the solenoid are given by equation (4.6). Both these quantities depend on the thickness δ_{sol} and the number of turns N of the solenoid, as it is shown in Figure 4.5 for the 3 T - MgB_2 SMES. Note that, as expected, the maximum storable energy $E_{max} = ½ L_c I_{max}^2$ does not depend on N since L increases as N^2. Given a solenoid with assigned thickness δ_{sol} and maximum storable energy E_{max} a high number of turns, which leads to a high inductance L_c, is desirable since it implies a smaller maximum current I_{max} (Figure 4.5 (a)) with the reduced size and the heat load of current leads. A more relaxed sizing of the switches of the DC-DC converter is also obtained with a smaller maximum current. However, the deliverable energy also decreases with the number of turns since the residual energy at I_{min} increases due to the high L (Figure 4.5 (b)). This means that, if a large number of turn is used, a larger solenoid with increased thickness δ_{sol} and increased maximum storable energy E_{max} must be used in order to deliver the same of energy ΔE. In essence, a larger solenoid with much higher capital cost must be built if a reduced current I_{max} is looked for. Higher capital cost is due to the fact that, as it is shown in Figure 4.4, the amount of SC conductor needed dramatically increases with the maximum storable energy. A compromise needs then to be found between a high number of turns and a cost effective solenoid. For this purpose the curves of constant maximum current I_{max} and constant deliverable energy ΔE as a function of the thickness and the number of turns of the solenoid are plotted in Figure 4.6 for the 3 T - MgB_2 SMES.

$$I_{\max} = J_{\max} b H_{sol} \delta_{sol} / N \tag{4.6}$$

$$\Delta E = 1/2\, L (I_{\max}^2 - I_{\min}^2)$$

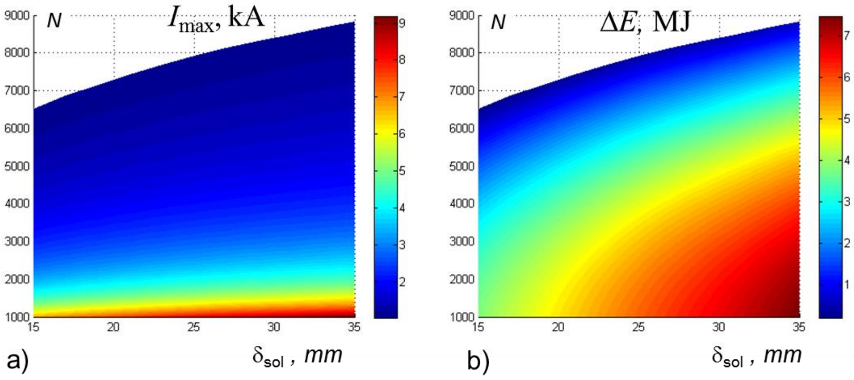

Figure 4.5 Dependence of maximum current I_{max} (a) and deliverable energy ΔE (b) on the thickness δ_{sol} of the solenoid and the number N of turns for the 3 T - MgB_2 SMES

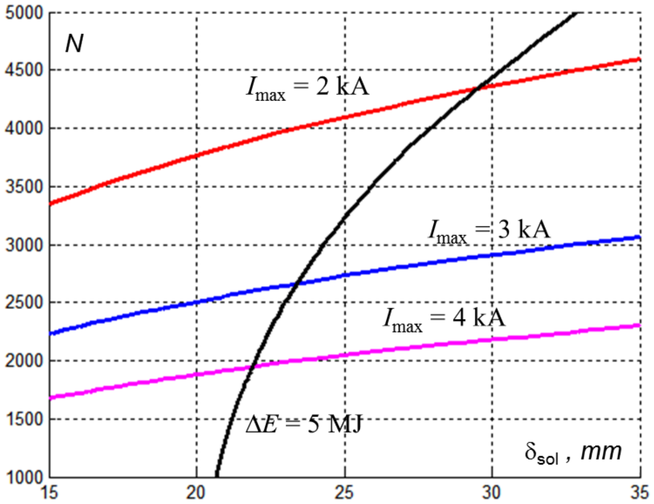

Figure 4.6 Curves of constant maximum current I_{max} and deliverable energy ΔE as a function of the thickness δ_{sol} of the solenoid and the number N of turns for the 3 T - MgB_2 SMES

4.3. AC LOSS

AC loss is the major concern for HTS-SMES technology. In order to reduce the AC losses subdivision of the HTS section of the conductors in a number of fine twisted filaments is essential [4.14]-[4.16]. MgB_2 conductors made of tens or hundreds of twisted filaments can easily be produced by means of the PIT technique [4.14]. As for the YBCO multifilamentary architecture can be obtained by means of, e.g., striations and electroplating [4.15]-[4.16]. No twisting is possible, however, in this case. Here it is assumed that the MgB_2 and the YBCO conductor are made of 361 and 10 filaments respectively. These conductors can be manufactured by means of nowadays industrial processes [4.14]-[4.16].

The current waveform of the 1MW-5s SMES during a discharge/charge cycle at full power (1 MW) is shown in Figure 4.7. Note that this waveform applies for all the designed SMES systems, no matter the material or the field level, since in all cases the chopper sees the SMES as a large and constant inductance (if the proper switching frequency for PWM controller of the DC-DC chopper has been chosen.). The corresponding AC losses per unit length of conductor are shown in Figure 4.8. These were calculated by means of the 2D FEM model developed in [4.17].

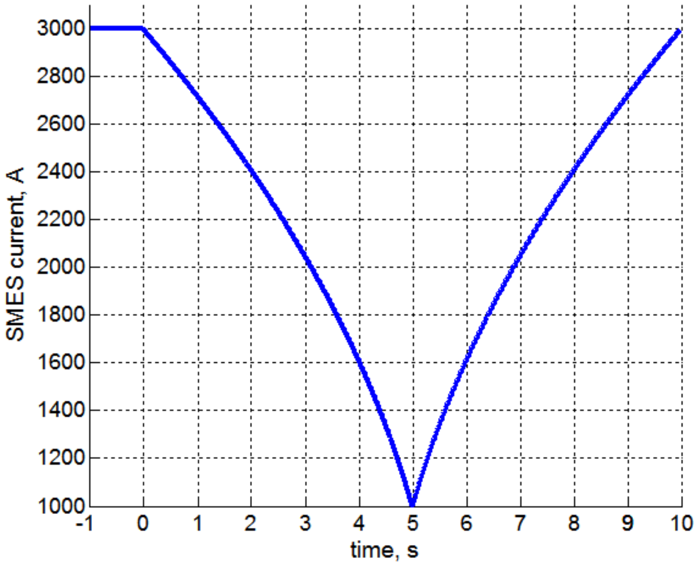

Figure 4.7 Current of the SMES during a 5s discharge/5s charge cycle at 1 MW

The AC loss per unit length of wire/tape depends on the applied field and hence on the position of the conductor within the coil. In order to obtain the plots of Figure 4.8 the losses were calculated on a discrete grid of points within the cross section. Linear interpolation can be used between these points. The total loss of the coil is obtained by integrating the distribution of Figure 4.8.

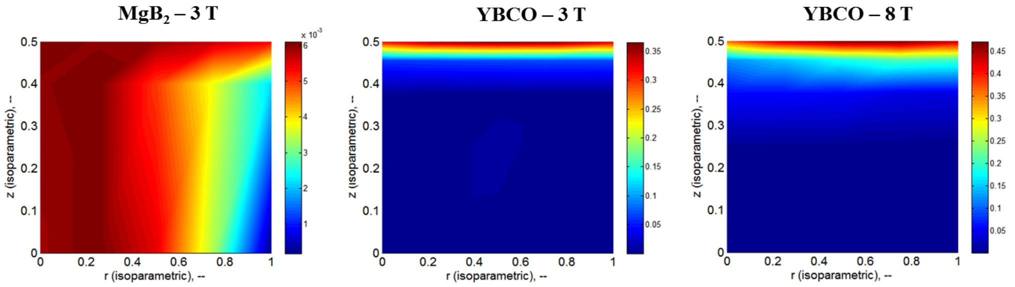

Figure 4.8 Distribution of ac loss (J/cycle) within the coil. Values are in Joule. Normalized coordinates are used for expressing the space dependence: $r^* = (r - R_i)/(R_o - R_i)$ and $z^* = z/H$

In concluding this section it is worth to point out that AC losses of YBCO based SMES could be reduced if a toroidal rather than solenoidal geometry is considered for the coil, since the perpendicular field of the conductor is reduced. Furthermore, toroidal geometry drastically reduces the stray field, thus avoiding the need of shielding which is required for the solenoid coil. However, it is to be considered that the manufacturing of a toroidal coil is more complex. No toroidal SMES of significant size have been manufactured so far.

4.4. REFERENCES

[4.1] V. Lombardo, E. Barzi, D. Turrioni, and A. V. Zlobin, “Critical Currents of YBa2Cu3O7-δ Tapes and Bi2Sr2CaCu2Ox Wires at Different Temperatures and Magnetic Fields,” 2010, FERMILAB-CONF-10-296-TD, online available at: http://lss.fnal.gov/archive/2010/conf/fermilab-conf-10-296-td.pdf

[4.2] G. Grasso – Columbus Superconductors, “In field performance of MgB2 wires”, April 2014, private communication

[4.3] D. Uglietti, H. Kitaguchi, S. Choi, and T. Kiyoshi, “Angular Dependence of Critical Current in Coated Conductors at 4.2 K and Magnet Design,” IEEE Transactions on Applied Superconductivity, Vol.19, No.3, June 2009, pages: 2909-2912, DOI: 10.1109/TASC.2009.2019089

[4.4] A. Xu, J. J. Jaroszynski, F. Kametani, Z. Chen, D. C. Larbalestier, Y. L. Viouchkov , Y. Chen, Y. Xie, and V. Selvamanickam, “Angular dependence of Jc for YBCO coated conductors at low temperature and very high magnetic fields,” Superconductor Science and Technology, Vol. 23, No. 1, 2010, 014003 (7pp), http://iopscience.iop.org/0953-2048/23/1/014003

[4.5] J. R. Thompson, J. W. Sinclair, D. K. Christen, Y. Zhang, Y. L. Zuev, C. Cantoni, Y. Chen, and V. Selvamanickam, “Field, temperature, and angle dependent critical current density Jc(H, T, θ) in coated conductors obtained via contact-free methods,” Superconductor Science and Technology, Vol. 23, No. 1, 2010, 014002 (6pp), DOI:0953-2048/23/1/014002

[4.6] P. M. Leys, M. Klaeser, F. Schleissinger, and T. Schneider, “Angle-Dependent U(I) Measurements of HTS Coated Conductors,” IEEE Transactions on Applied Superconductivity, Vol.23, No.3, June 2013, DOI:10.1109/TASC.2012.2232700

[4.7] L Kopera, P Kováč, I Hušek and T Melišek, "Rutherford cable made of single-core MgB2 wires," 2013 Supercond. Sci. Technol. 26 125007 (6pp), DOI:10.1088/0953-2048/26/12/125007

[4.8] W. Goldacker, F. Grilli, E. Pardo, A. Kario, S. I. Schlachter, and M. Vojenčiak, "Roebel cables from REBCO coated conductors: a one-century-old concept for the superconductivity of the future," Superconductor Science and Technology. Vol. 27, No.9, 2014, 093001, DOI: 10.1088/0953-2048/27/9/093001

[4.9] M. Staines, N. Glasson, M. Pannu, K. P. Thakur, R. Badcock, N. Allpress, P. D'Souza, and E. Talantsev, "The development of a Roebel cable based 1 MVA HTS transformer," Superconductor Science and Technology, Vol. 25, No. 1, 2012, 014002, DOI:10.1088/0953-2048/25/1/014002

[4.10] W. Hassenzahl, "A comparison of the conductor requirements for energy storage devices made with ideal coil geometries," IEEE Transactions on Magnetics, Vol. 25, No. 2, March 1989, pages: 1799,1802, DOI:10.1109/20.92651

[4.11] Y. Shiroyanagi, A. K. Ghosh, R. Gupta, and W.B. Sampson, "The Construction and Testing of YBCO Pancake Coils for a High Field Solenoid," IEEE Transactions on Applied Superconductivity, Vol. 21, No.3, June 2011, pages: 1649-1652, DOI: 10.1109/TASC.2010.2097570

[4.12] S. Lim, J. Barc, Y. Jung, D. Youm, C. Park, and H. Kim, "Analyses of a solenoid magnet made of pancakes of coated conductors," Superconductor Science and Technology, Vol. 18, No. 4, 2005, DOI:0953-2048/18/4/010

[4.13] M. N. Wilson "Superconducting Magnets", Oxford, Clarendon Press, 1987, page: 44

[4.14] A. Malagoli, C. Bernini, V. Braccini, C. Fanciulli, G. Romano, and M. Vignolo, "Fabrication and superconducting properties of multifilamentary MgB2 conductors for AC purposes: twisted tapes and wires with very thin filaments," Superconductor Science and Technology, Vol. 22, No. 10, 2009, 105017 (6pp), DOI:10.1088/0953-2048/22/10/105017

[4.15] I. Kesgin, G. Majkic, and V. Selvamanickam, "Fully filamentized HTS coated conductor via striation and selective electroplating", Physica C: Superconductiviy, Vol. 486, 2013, pages: 43–50, DOI:10.1016/j.physc.2013.01.016

[4.16] S. Terzieva, M. Vojenčiak, F. Grilli, R. Nast, J. Šouc, W. Goldacker, A. Jung, A. Kudymow and A. Kling, "Investigation of the effect of striated strands on the AC losses of 2G Roebel cables", Superconductor Science and Technology, Vol. 24, No. 4, 2011, 045001 (5pp), DOI:10.1088/0953-2048/24/4/045001

[4.17] A. Morandi, "2D electromagnetic modelling of superconductors," Supercondcutor Science and Technology, Vol. 25, No. 10, 2012, 104003, DOI:10.1088/0953-2048/25/10/104003

5. SMES COIL MODELLING

5.1. POWER SYSTEM TRANSIENTS BRIEF OVERVIEW

Transients in electrical power system can happen either during normal operating condition (e.g. normal operation of the switches/breakers) or in abnormal operating condition (e.g. faults) and physical phenomena (lightning strikes). Since it is considered that most power system transients have oscillatory nature, they characterize with the frequency of the oscillation [5.1].

Table 5.1. Classification of power system transients

Mode	Frequency (Hz)	Event
Electromechanical phenomena	0.001	Load frequency control
	0.01	
	0.1	
	1	Transient stability stabilizer
	10	
	10^2	Short circuits, Sub-synchronous resonance, Harmonics, Power conversion phenomena
Electromagnetic phenomena	10^3	
	10^4	Switching transients
	10^5	
	10^6	Traveling wave phenomena
	10^7	Transient recovery voltage

Transients in power system happen in very short time duration, but they are capable of causing flashovers, insulation breakdowns as a result of high transient voltage and current. A good modeling and analysis of transient behavior of a device is essential to predict over-voltages that may damage the system. Any physical power system element can be represented either by a lumped or distributed parameter model.

Several types of switching such as load switching, electric faults, capacitor switching and transformer energization may cause to generate severe transients. These transients should be well-evaluated in order to predict and determine protection to over-voltages or over-currents. The basic principles of over-voltage protection can be classified as follows [5.2]:

- limiting the voltage across sensitive insulation

- diverting the surge current and thus preventing the surge entering the load
- bonding ground references together at the equipment
- creating a low pass filter across the sensitive load to limit high frequency transients

Switching based transients could be eliminated by transient voltage surge suppressor (surge arresters). These devices should be located as closely as possible to the critically insulated equipment. Surge arresters are characterized by a voltage-current (V-I) curve. The V-I characteristic indicates that the device will never allow the voltage to exceed the value of the permissible voltage level. The most favorable device, which is used in the power system, is the metal oxide varistor (MOV) and mostly zinc oxide as a metal oxide is implemented.

5.2. TRANSIENT CONCERN IN SMES COIL

Normal or abnormal operation of the PCS of the SMES, lightning, and switching surge coming from AC system produce transient in the SMES coil. Insulation failure because of the transient over-voltages in the superconducting coil is an important issue where the insulation characteristics of the coil in the cryogenic environment are different from that at normal conditions. Compared to the steady state, transients take place for a very short time, but they have the potential to stress the coil insulation. It is essential to understand the transient behavior of a SMES coil in the design of the insulation and transient suppression schemes. A SMES coil may experience unexpected failures if the behaviors of the transient over-voltages associated with the coil are not well understood. The design of SMES coil insulation and protection systems plays an important role in avoiding SMES coil failures.

Most of the studies on the transient behavior of the SMES coil are done case by case and there are not published [1.1]. However, there are published studies [2.15] and [5.3]-[5.6]. Some of the main conclusions of these studies are as follows:

- Internal coil voltage can be higher than the terminal voltage if the coil is excited at the resonant frequency.
- The resonant frequencies could be much less for large superconducting coils depending on the winding structure.
- The damping of the transient oscillations at the cryogenic temperature is weaker than in the normal conducting coil.

5.3. COIL MODEL CONSIDERATION

The structure of the coil insulation is the major concern in the superconducting coil design, where it is important for the reliable and economic operation of the entire SMES system. A geometrically large coil makes the design more complex. In order to have complete design of the insulation structure of a winding, the transient voltage stresses of the all subcomponents of the structure must be known. The frequency response of the winding is essential in the coil insulation design.

The methods to determine these characteristics are: direct measurement on the actual winding, direct measurement on an electromagnetic model of the coil, or building a mathematical model and determining the voltage distribution and frequency response by means of the suitable computer analysis program. The first two methods give more reliable and accurate results than the mathematical analysis, however setting up a mathematical model is the most convenient and lowest cost method [5.6]. Consequently, a greater variety of design alternatives and more detailed analysis can be achieved by the mathematical model of a winding [2.15].

The detailed model of the coil should represent self and mutual inductance (L and M), and the capacitance between adjacent turns (C_{adj}), axially separated turns (C_{ax}) and turn to ground (C_{g}) of every turn of the winding. Due to high memory and computing cost, various degrees of simplification are necessary. According to [5.7], the relatively small number of frequencies is sufficient, therefore a distributed winding can be represented by an equivalent circuit of a finite but sufficient number of lumped elements. It has been emphasized that the mutual inductance must be included in a transient analysis purpose modeling for more accurate solutions.

Transient and steady state behavior of the circuit exited by an applied voltage can be established by the location of the zeros and poles of the impedance function of the circuit in the complex frequency plane. By definition, the zeros coincide with the natural frequencies of the circuit. Series resonance occurs where the terminal impedance is at its minimum, and parallel resonance occurs where the terminal impedance is at its maximum [5.7].

For dynamic operation, simulating the superconducting coil with a big inductor is common practice. However, for transient analyses, the more detailed coil model representing disks, even turns, with associated mutual inductance and capacitance yields to more accurate results [5.7].

5.4. CALCULATION OF ELECTRICAL PARAMETERS FOR A DISK TYPE WINDING

An electrical lumped parameter model is constructed for a superconducting coil to determine voltage distribution and the frequency response of the coil. A generic lumped parameter model is given in Figure 5.1. It is assumed that the coil consists of a number of disks (pancakes) comprising of a number of turns. Given the geometrical dimension of a coil, the following parameters need to be calculated for turns of the coil.

- Self-inductance of a turn
- Mutual inductance between turns
- Capacitance between adjacent turns
- Capacitance between axially separated turns
- Capacitance between turn to ground

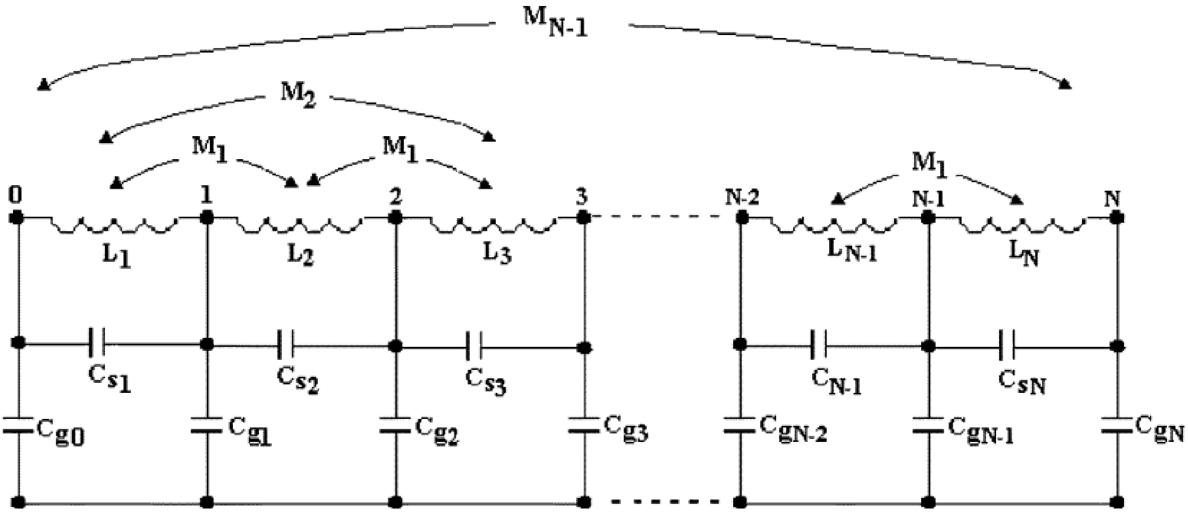

Figure 5.1 Schematic representation of a winding. C_{gi}: shunt capacitance, C_{si}: series capacitance, L_i: self-inductance, M_i = mutual inductance [5.6]

In order to calculate the inductance and capacitance of a particular turn in the coil the physical dimensions of the coil as illustrated in Figure 5.2 should be given. Figure 5.2 (a) shows the cross section of the entire coil having a number of disks, Figure 5.2 (b) illustrates two disks on top each other, and Figure 5.2 (c) displays the required dimensions in parameters computation for a turn/disk coil. In the following subsections, approximated formulas in parameter calculations will be given.

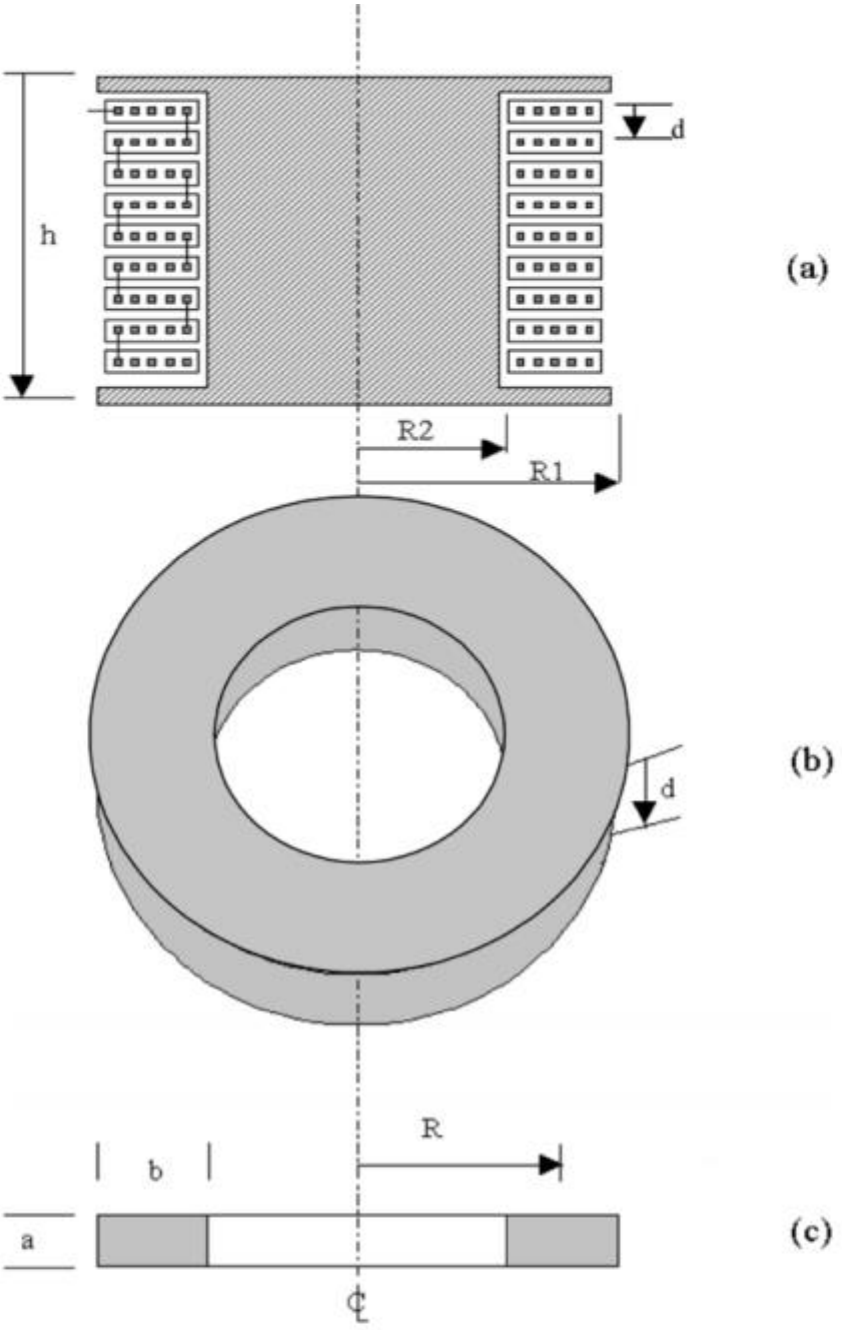

Figure 5.2 Physical dimensions for the disc type coil [5.6]

5.4.1. Self and mutual inductance calculation

Based on geometric entities inductance calculation can be written as follows [5.6]:

$$L = \mu_0 R N^2 \ln\left(\frac{8R}{R1} - 2\right)$$

(5.1) $$\ln R1 = \frac{1}{2}\ln\left(a^2 + b^2\right) - \frac{b^2}{12a^2}\ln\left(1 + \frac{a^2}{b^2}\right)$$

$$- \frac{a^2}{12b^2}\ln\left(1 + \frac{b^2}{a^2}\right) + \frac{2b}{3a}\tan^{-1}\frac{a}{b} + \frac{2a}{3b}\tan^{-1}\frac{b}{a} - \frac{25}{12}$$

where N is the number of turns in a pair of disk coils (double pancake), other dimensions are illustrated in Figure 5.2. If the inductance of one turn is to be calculated, then $N=1$. Also, the inductance can be calculated by using tables in [5.6], [5.8] and [5.9]:

(5.2) $$L = 10^{-7} R N^2 P_0$$

where P_0 is determined by the ratio of $\rho = b/2R$, which determines the thickness of the coil as:

(5.3) If $\rho < 0.2$, then $P_0 = 4\pi\left(0.5\left(1 + \frac{\rho}{6}\right)\log\left(\frac{8}{\rho}\right) - 0.84834 + 0.2041\rho\right)$

If $\rho > 0.2$, then P_0 is found from the tables given in [5.8]

Mutual inductance between two circular filaments is calculated by using the formula developed by Maxwell [5.3], [5.6], and [5.10]:

(5.4) $$M_{1-2} = \mu_0\sqrt{R_1 R_2}\left[\left(\frac{2}{k} - k\right)K(k) - \frac{2}{k}E(k)\right]$$

$$k = \sqrt{\frac{4R_1R_2}{\left(R_1 + R_2\right)^2 + d^2}}$$

where R_1 and R_2 are the radius of the circular filaments 1 and 2, d is the distance between circular filaments, μ_0 is the permeability of free space, and $K(k)$ and $E(k)$ are the complete elliptic integrals of the first and second kind.

Equation (5.4) is valid for circular filaments of negligible cross section. If the cross sectional dimensions are not small enough compared to the distance between the coils, then Lyle's method is applied to calculate the mutual inductance between turns or coils [5.6]. Lyle's method states that each coil (Coils 1 and 2) can be represented by two equivalent filaments as shown in Figure 5.3.

Mutual inductance between each equivalent filament (11'-33', 11'-44', 22'-33' and 22'-44') is calculated using equation (5.4), where R_1 and R_2 are replaced with an equivalent radii of r and spacing between coils vary between $d+2ß$ and $d-2ß$ in equation (5.5).

(5.5) $$r_{\mathrm{i}} = R_{\mathrm{i}}\left(1+\frac{c^2}{24R_{\mathrm{i}}^2}\right), \quad \beta = \sqrt{\frac{b^2-c^2}{12}}$$

The average of each calculated mutual inductance gives the mutual inductance between the two coils.

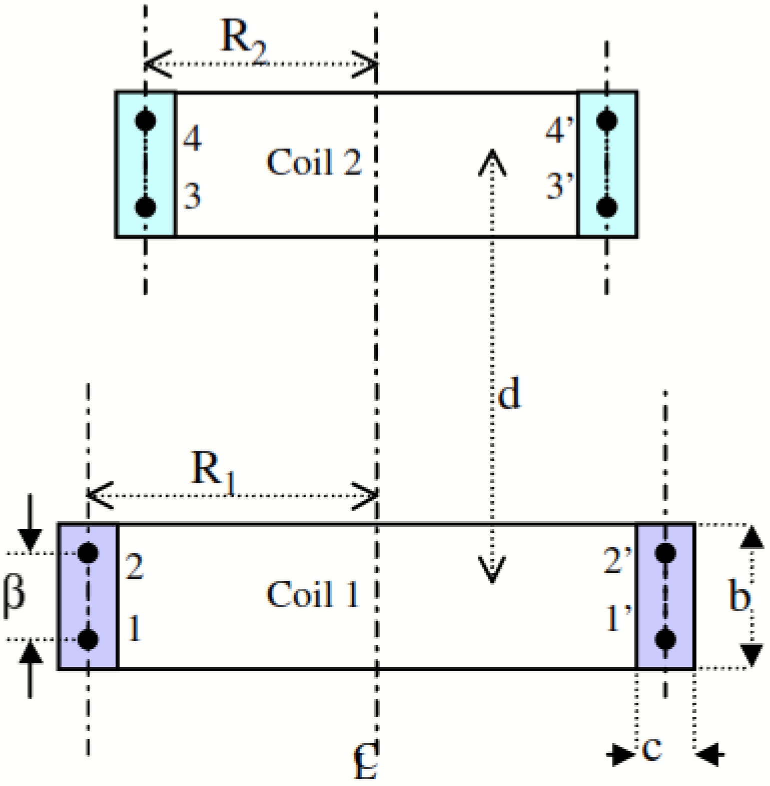

Figure 5.3 Coil representation by Lyle's method for b > c [5.6]

5.4.2. Capacitance calculation

Based on the geometric entities, series capacitance between turns, shunt capacitance between axially separated turns, and turn to ground capacitance of the double pancake can calculate easily and accurately by using the parallel plate formula:

(5.6) $$C = \frac{\varepsilon_0 \varepsilon_r A}{d}$$

where $\varepsilon_0 = 8.854\times10^{-7}$, ε is the constant of the dielectric between two plates, *A* is the area between two plates, and *d* is the distance between the plates.

The capacitances of turns in a double pancake are combined to represent capacitances between double pancakes and to ground. Equations for the series capacitance of the total winding developed by several authors have been summarized in [5.8].

5.5. LUMPED PARAMETER MODEL OF THE COIL

5.5.1. Modeling assumptions

The SMES coil can be accurately modeled with lumped parameters [5.6]. In this model, each double pancake is represented by self and mutual inductors, and series and ground capacitors. By lumping the inductance and capacitance of the turns which forms the pancake the inductance and capacitance values of a double pancake can be obtained. In following additional assumptions are made [5.6] and [5.11]:

- The dielectric constant of the insulating material does not vary with frequency.
- The thermal enclosure and the tank do not carry current, and they were represented as ground plane.
- A small value of resistor represents skin effect and eddy current losses.
- Parallel plate model is employed to calculate ground and series capacitances of each turn.
- To reduce the computing cost, each double pancake (two single pancakes) is represented by its series inductance, capacitance, mutual inductance, and ground capacitances.

The SMES coil is essentially a complex air core inductor, and there is no nonlinear behavior and saturation in the core, therefore the transient voltage response can be computed using programs which employ a linear solution methodology. A linear voltage drop is also assumed to calculate the capacitance of a winding that consists of a number of turns. Schematic representation of capacitive parameters of the entire coil is shown in Figure 5.4. It should be noted that the mutual capacitances between turns are not shown in this figure. In Figure 5.4, C_g is the Capacitance between a turn and ground, C_{ad} is the capacitance between adjacent turns within a disk coil, C_{ax} is the capacitance between axially separated turns, N is the number of turns in a single pancake, and N_{sp} is the number of single pancakes in a coil.

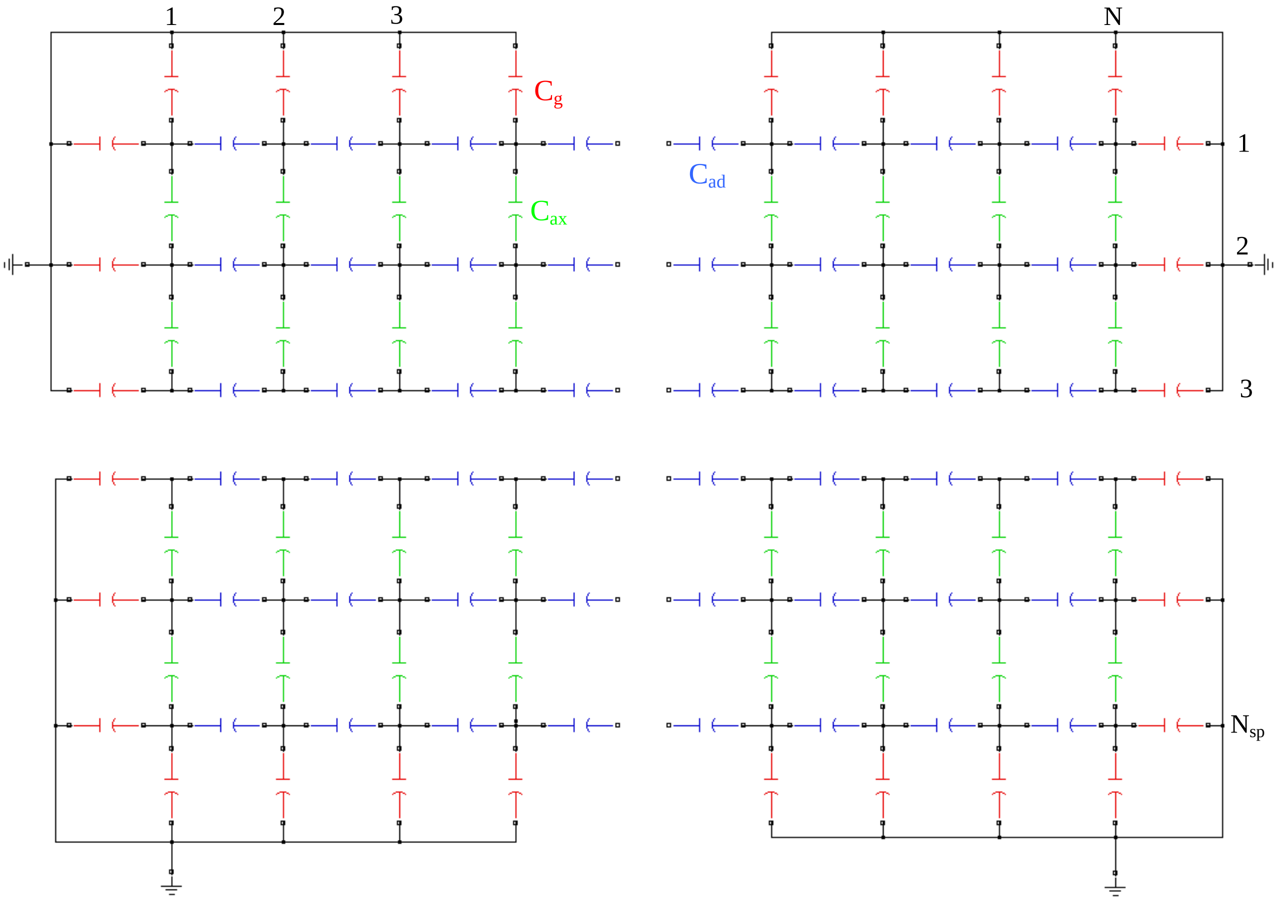

Figure 5.4 Schematic illustration of capacitive parameters in the entire coil

5.5.2. Modeling steps

Modeling of the coil in this thesis is based on [5.6]. The most detailed mathematical model for a coil can be obtained if each turn in the coil is represented by its associated self and mutual inductance and associated capacitance of each turn. However, if the coil is consists of excessive number of turns such a detailed model requires more memory and computing time [5.6]. Turns which make a double pancake can be lumped to model the coil in the level of double pancakes instead of the single turns. Step by step procedure for modeling the coil in the level of the pancake. As an example, it is considered that there is a coil with N_{sp}=20 single pancake (N_{dp}=10 double pancake) where each single pancake (SP) consists of N = 20 turns.

5.5.2.1. Forming inductance matrix

- Calculate self-inductances for each turn in a single pancake (SP) by applying the Miki's formula [5.3], and mutual inductances between each turn in a SP by applying the Lyle's method.
- Construct a $N\times N$ (20×20) matrix block (A in equation (5.7)) where N is the number of turns in a SP. The diagonal elements correspond to the self-inductances and off-diagonal elements correspond to mutual inductances between turns in a SP

$$L_{\text{turn}} = \begin{bmatrix} [A]_{N\times N} & [B]_{N\times N} & [C]_{N\times N} & . & . & . & [T]_{N\times N} \\ [B]_{N\times N} & [A]_{N\times N} & [B]_{N\times N} & . & . & . & [S]_{N\times N} \\ [C]_{N\times N} & [B]_{N\times N} & [A]_{N\times N} & . & . & . & [R]_{N\times N} \\ [D]_{N\times N} & [C]_{N\times N} & [B]_{N\times N} & . & . & . & [Q]_{N\times N} \\ [E]_{N\times N} & [D]_{N\times N} & [C]_{N\times N} & . & . & . & [P]_{N\times N} \\ . & . & . & . & & & . \\ . & . & . & & . & & . \\ . & . & . & & & . & . \\ [T]_{N\times N} & [S]_{N\times N} & [R]_{N\times N} & . & . & . & [A]_{N\times N} \end{bmatrix}_{NN_{\text{s}}\times NN_{\text{s}}} \tag{5.7}$$

- Apply Lyle's method to calculate mutual inductances between turns in the first SP and turns in the other SPs. A series of $N\times N$ (20×20) matrix blocks (B to T in the equation (5.7)) are constructed where each $N\times N$ (20×20) represents mutual inductances between the first SP and other SPs. These matrix blocks and the one constructed in previous step builds a column with a size of $N\times N_{\text{sp}}\times N$ (400×20).
- Once the first column of L_{turn} is formed, a lumped inductance matrix representing the double pancakes of the coil is computed as given in equation (5.8).

$$L_{\text{db}} = \begin{bmatrix} sum(ABAB) & sum(CBCD) & . & . & . & sum(SRST) \\ sum(CBCD) & sum(ABAB) & . & . & . & . \\ sum(EDEF) & sum(CBCD) & . & . & . & . \\ . & . & . & & & . \\ . & . & & . & & . \\ . & . & & & . & . \\ sum(SRST) & . & . & . & . & sum(ABAB) \end{bmatrix}_{2N_{\text{s}}\times 2N_{\text{s}}} \tag{5.8}$$

$$sum(ABAB) = \sum_{i=1}^{N}\sum_{j=1}^{N} A(i,j) + \sum_{i=1}^{N}\sum_{j=1}^{N} B(i,j) + \sum_{i=1}^{N}\sum_{j=1}^{N} A(i,j) + \sum_{i=1}^{N}\sum_{j=1}^{N} B(i,j) \tag{5.9}$$

5.5.2.2. Calculating capacitances for a double pancake

- Calculate capacitances between adjacent turns (C_{ad}), axially separated turns (C_{ax}) and turns to ground (C_g) shown in Figure 5.3 and Figure 5.4 using equation (5.6).
- Capacitances between adjacent turns and axially separated turns are combined in such way shown in Figure 5.5 to compute the equivalent series capacitance for a double pancake.
- Ground capacitances calculated for each turn within a double pancake are summed to obtain an equivalent ground capacitance for a double pancake.

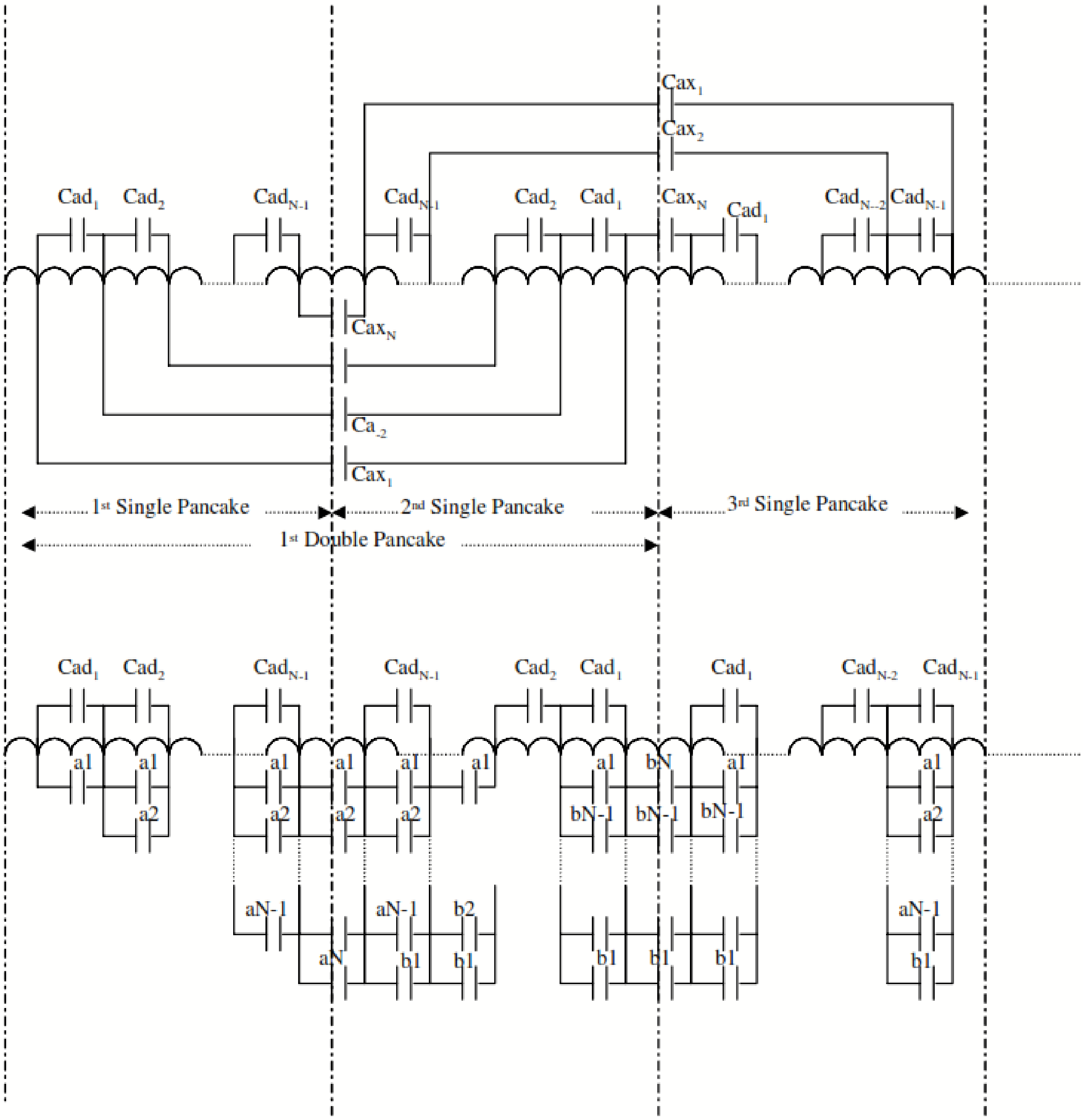

Figure 5.5 Derivation of equivalent series capacitance for a double pancake [5.6]

In Figure **5.5** $a1=(2N-1)C_{\mathrm{ax}_1}$, $b1=(2N-1)C_{\mathrm{ax}_\mathrm{N}}$, $a2=(2N-3)C_{\mathrm{ax}_2}$, $b2=(2N-3)C_{ax_{N-1}}$, $a3=(2N-5)C_{\mathrm{ax}_3}$, $b3=(2N-5)C_{\mathrm{ax}_{\mathrm{N}-3}}$, $aN-1=3C_{\mathrm{ax}_{\mathrm{N}-1}}$, $bN-1=3C_{\mathrm{ax}_2}$, $aN=1C_{\mathrm{ax}_\mathrm{N}}$, and $bN=1C_{\mathrm{ax}_1}$.

5.6. REFERENCES

[5.1] A. P. S. Meliopoulos “Power System Grounding and Transients,” Marcel Dekker Inc. 1988

[5.2] R.C. Dugan, M.F. McGranaghan, S. Santoso, and H.W. Beaty, “Electrical Power Systems Quality,” 3rd edition, McGraw-Hill, 2012

[5.3] A. M. Miri, C. Sihler, M. Droll, and A. Ulbricht, ”Modelling the Transient Behaviour of a Large Superconducting Coil Subjected to High Voltage Pulses,” The Proceedings of International Conference on Power System Transients (IPTS’95), No. 563, September 1995, pages: 57-62, http://www.ipstconf.org/papers/Proc_IPST1995/95IPST024-16.pdf

[5.4] J A.M. Miri, C. Sihler, H. Salbert, K.-U Vollmer, “Investigation of the Transient Behaviour of a Superconducting Magnetic Energy Storage (SMES) Generating High Power Pulses,” European Transactions on Electrical Power Engineering, Vol. 8, No. 1, January-February 1998, pages 13-19, http://onlinelibrary.wiley.com/doi/10.1002/etep.4450080103/abstract

[5.5] M. Steurer, C. A. Luongo, P. R. Ribeiro, and S. Eckroad, “Interaction Between a Superconducting Coil and the Power Electronics Interface on a 100 MJ SMES System,” IEEE Transactions on Applied Superconductivity, Vol. 13, No. 2, JUNE 2003, pages 1806-1809, DOI: 10.1109/TASC.2003.812895

[5.6] L. Chen, Y. Liu, A. B.Arsoy, P. F. Ribeiro, M. Steurer, and M. R. Iravani, (IEEE Task Force on Benchmark Models for Digital Simulation of FACTS and Custom-Power Controllers, T&D Committee), “Detailed Modeling of Superconducting Magnetic Energy Storage (SMES) System,” IEEE Transactions on Power Delivery, Vol. 21, NO. 2, April 2006, pages 699-710, DOI:10.1109/TPWRD.2005.864075

[5.7] P.A. Abetti and F.J. Maginniss, “Natural Frequencies of Coils and Windings Determined by Equivalent Circuit,” Transactions of the American Institute of Electrical Engineers Power Apparatus and Systems, Part III, Vol.72 No. 2, June 1953, pages: 495-504, DOI: 10.1109/AIEEPAS.1953.4498660

[5.8] P. Chowdhury, “Calculation of series capacitance for transient analysis of windings,” IEEE Transactions on Power Delivery, Vol. 2, No. 1, Jan. 1987, pages: 133–139, DOI: 10.1109/TPWRD.1987.4308083

[5.9] F. W. Grover, “Inductance Calculations: Working Formulas and Tables,” Dover Phoenix Editions, Dover Piblications Inc. USA, 2004, ISBN: 0-486-49577-9, 9780486495774

[5.10] A. Greenwood, “Electrical Transients in Power Systems,” Wiley, May 1991, ISBN: 978-0-471-62058-7

[5.11] R. C. Degeneff, “Calculating Voltage versus Time and Impedance versus Frequency for the SMES Coil,” Babcock & Wilcox by Utility Systems Technologies, Inc, 1995

PART II. HIGH TEMPERATURE SUPERCONDUCTING CABLE

6. INTRODUCTION

Future large renewable sites will install in the rural areas and far from the load centers, transmitting such a large power from those renewable like offshore wind parks over long distances (hundreds of kilometers), is accompanied by power losses caused predominantly by I^2R heating effects. Ideally, power losses in the conventional transmission and distribution network should be around 3 to 6% of the total power delivered [6.1]. Utility companies are currently interested in reducing the power losses which are associated with transmission and distribution networks.

According to International Energy Outlook in 2008, worldwide energy demand will increase by 36.8% by 2030 [6.2]. In developing countries and in large cities the power demand will increase because of the population growth and also because of the urbanization, new requirements such as electric vehicles and improvement in living standards. Continues power demand increment in highly populated urban areas raises questions such as how to deliver more power, reduce power losses, and reduce voltage drop in these critical areas. Consequently, there is increased interest in the integration of more distributed generators (DGs) into distribution networks to meet anticipated future demand [6.3]. Advantages of integrating these DGs into distribution networks include enhanced power support, reduced power losses and improved voltage profile [6.4] and [6.5], however, operating many of DGs into these networks increases issues associated with stability, power management and voltage regulation [6.6]. There are many techniques currently implemented in distribution networks to reduce the voltage excursions and power losses such as control sharing of reactive power between DGs, power factor control, capacitor placement and transformer tap changer control [6.7]. However, these techniques often increase system capital and operational costs.

High voltage DC transmission of bulk power is today a viable alternative or complement to AC transmission since it offers several advantages including reduced costs, losses and footprint, especially for long distances. However, higher voltage levels require more physical space. Therefore the need of transmitting a high amount power at lower voltage levels is necessary in areas where there is space limit. In addition, increased delivery of power to urban areas is challenging when considering conventional power system technologies such as conductors and transformers, especially in cases where space to install new cables and transformers is limited.

Transmitting power at different voltage levels in conventional distribution networks influences the amount of current that flows through the network component cables, overhead lines and transformers. By delivering power at a higher voltage level, the amount of current transmitted through the distribution network is decreased; therefore the power losses are decreased. Transmitting power at higher voltage levels increases the cost of substations. Lowering the voltage increases the power losses and reduces the investment costs [6.8] and [6.9]. Consequently, many studies have attempted to introduce a new design for conventional distribution networks that target a reduction in substation costs by reducing some voltage levels in networks [6.8]-[6.10]. Using conventional equipment at lower voltage levels causes the current increases and it is in turn increases the power losses. Discovering and using new and superior materials to improve the performance of the distribution system is a key challenge for the conventional distribution network. This could include cables and transformers with significantly lower impedance and higher power ratings to reduce power losses and substations costs in transmission and distribution levels.

Since the DC system is less expensive than the AC system with reduced power losses, DC operation is also receiving an increasing attention at the medium (MV) and the low (LV) voltage level. DC MV and LV systems cause the flexible and cost effective integration of renewable generation and storage. Furthermore, several large loads, especially in industry or IT sectors, require a low voltage DC supply for their operation. On board LV DC distribution is also considered as an effective mean for reducing fuel consumption. In essence, after one century of AC exclusive for electricity transmission and distribution, coexistence of DC is started and will increase in the future driven by the progress in power electronics [6.11].

Between DC transmission and distribution system and HTS technology a good synergy exists where no losses occur during DC operation in HTS cable. Therefore, the efficiency of DC power cables can be drastically increased, especially in the cases where the operation at very high DC current is required. Besides, using HTS makes the system compact and operation at lower DC voltage will be possible, where the current carrying capacity of the HTS material is more than the copper cable at the same size. Recently great research effort has been carried out for the development of DC HTS cables, and they are regarded as key components to penetration of DC transmission and distribution technology [6.12]-[6.27].

6.1. REFERENCES

[6.1] L. Ramesh, S. Chowdhury, S. Chowdhury, A. Natarajan, and C. Gaunt, “Minimization of Power Loss in Distribution Networks by Different Techniques,” International Journal of Electrical Power and Energy Systems Engineering, Vol. 2, 2009, http://www.waset.org/publications/939

[6.2] A need for smart energy demand and supply. Available: IBM Smart Energy–Overview-United-Kingdom, 2012 (online available) http://www.ibm.com/smarterplanet/uk/en/smart_grid/ideas/index.html

[6.3] C. Masters, “Voltage rise: the big issue when connecting embedded generation to long 11 kV overhead lines,” Power Engineering Journal, Vol. 16, No. 1, 2002, pages: 5-12, DOI: 10.1049/pe:20020101

[6.4] M. N. Marwali, J. W. Jung, and A. Keyhani, “Control of distributed generation systems-Part II: Load sharing control,” IEEE Transactions on Power Electronics, Vol. 19, No. 6, 2004, pages: 1551-1561, DOI:10.1109/TPEL.2004.836634

[6.5] K. Thyagarajan, A. Davari, and A. Feliachi, “Load sharing control in distributed generation system,” Proceedings of the Thirty-Seventh southeastemymposium on System theroy (SSST’05), 20-22 March 2005, pages: 424-428, DOI: 10.1109/SSST.2005.1460950

[6.6] T. L. Vandoorn, B. Renders, B. Meersman, L. Degroote, and L. Vandevelde, “Reactive power sharing in an islanded microgrid,” 45th International Universities Power Engineering Conference, 30 Auguts - 03 September 2010, Cardiff, Wales, pages: 1-6, http://ieeexplore.ieee.org/xpls/abs_all.jsp?arnumber=5649458

[6.7] P. Kundur, N. J. Balu, and M. G. Lauby, “Power system stability and control” McGraw-hill New York, 1994, ISBN: 0-07-035958-X

[6.8] J. Andruszkiewicz, J. Lorenc, and K. Marszalkiewicz, “Influence zones and disturbance levels in LV and MV distribution network in result of supply of industrial welder lines equipped with power conditioner,” 18th International Conference and Exhibition on Electricity Distribution (CIRED 2005), 6-9 June 2005, Turin, Italy pages: 1-4, http://ieeexplore.ieee.org/xpl/articleDetails.jsp?arnumber=5427728

[6.9] D. M. Cao, D. Pudjianto, G. Strbac, R. Ferris, I. Foster, and M. Aten, “Examination of the impact of possible distribution network design on network losses,” 20th International Conference and Exhibition on Electricity Distribution - Part 1 (CIRED 2009), 8-11 June 2009, Prague, Czech Republic, pages: 1-4, http://ieeexplore.ieee.org/xpl/articleDetails.jsp?arnumber=5255810

[6.10] S. Curcic, G. Strbac, and X. -P. Zhang, “Effect of losses in design of distribution circuits,” IEE Proceedings - Generation, Transmission and Distribution, Vol. 148, No. 4, 2001 , pages: 343-349, DOI: 10.1049/ip-gtd:20010359

[6.11] A. Morandi, “HTS DC transmission and distribution: Concepts, applications and benefits,” Topical Review - Superconductor Sience and Technology, Vol. 28, No. 12, 2015, DOI:10.1088/0953-2048/28/12/123001

[6.12] R. Hata, ““GENESIS Project” and High-Temperature Superconducting (HTS) DC Cable –Keen Use of Ultimately Sustainable New Energies–,” Sei Technical review, No. 66, April 2008, pages 14-30, http://global-sei.com/technology/tr/bn66/pdf/66-02.pdf

[6.13] P. Chowdhuri, C. Pallem, J. A. Demko, and M. J. Gouge, “Feasibility of electric power transmission by DC superconducting cables,” IEEE Transactions on Applied Superconductivity, Vol.15, No.4, December 2005, pages: 3917-3926, DOI: 10.1109/TASC.2005.859046

[6.14] P. M. Grant, “Superconducting Lines for the Transmission of Large Amounts of Electrical Power over Great Distances: Garwin–Matisoo Revisited Forty Years Later,” IEEE Transactions on Applied Superconductivity, Vol.17, No.2, June 2007, pages: 1641-1647, DOI: 10.1109/TASC.2007.899981

[6.15] W. V. Hassenzahl, S. Eckroad, P. M. Grant, B. Gregory, and S. Nilsson, “A High-Power Superconducting DC Cable,” IEEE Transactions on Applied Superconductivity, Vol. 19, No.3, June 2009, pages: 1756-1761, DOI:10.1109/TASC.2009.2017844

[6.16] “Program on Technology Innovation: a Superconducting DC Cable,” EPRI Final Report 1020458, December 2009, http://goo.gl/7zQcpD

[6.17] J. V. Minervini, L. Bromberg, P. Michael, C. Miles, N. R. LaBounty, “Superconducting DC Power Transmission and Distribution,” PSFC/RR-09-2, Engineering and Technology Division, MIT Plasma Science and Fusion Center, February 18, 2009, http://goo.gl/L2v3ou

[6.18] C. Rubbia, “The future of large power electric transmission,” Workshop on Transporting Tens of Gigawatts of Green Power to the Market, Postdam-Germany, May 2011, http://goo.gl/lxeZgo

[6.19] K. Allweins and E. Marzahn, “Feasibility of HTS DC Cables on Board a Ship,” 10th EPRI Superconductivity Conference, 2011, http://goo.gl/rAzani

[6.20] V. S. Vysotsky A. A. Nosov, S. S. Fetisov, G. G. Svalov, V. V. Kostyuk, E. V. Blagov, I. V. Antyukhov, V. P. Firsov, B. I. Katorgin, and A. L. Rakhmanov, “Hybrid Energy Transfer Line With Liquid Hydrogen and

Superconducting MgB2 Cable—First Experimental Proof of Concept," IEEE Transactions on Applied Superconductivity, Vol.23, No.3, June 2013, DOI: 10.1109/TASC.2013.2238574

[6.21] A. Morandi, G. Mazzanti and M. Marzinotto, "Feasibility of High Voltage DC superconducting cables with extruded warm dielectric," IEEE Conference on Electrical Insulation and Dielectric Phenomena (CEIDP), 19-22 October 2014, Des Moines, IA, pages: 796 - 799, DOI: 10.1109/CEIDP.2014.6995878

[6.22] V. S. Vysotsky, E. V. Blagov, V. V. Kostyuk, A. A. Nosov, S. S. Fetisov, S. Yu. Zanegin, I. V. Antyukhov, V. P. Firsov, G. G. Svalov, B. I. Katorgin, V. S. Rachuk, "New 30-m Flexible Hybrid Energy Transfer Line With Liquid Hydrogen and Superconducting MgB_2 Cable — Development and Test Results," IEEE Transactions on Applied Superconductivity, Vol. 25, No.3, June 2015, pages: 1-5, DOI: 10.1109/TASC.2014.2361635

[6.23] D. Shaotao, X. Liye, Z. Hongen, T. Yuping, L. Xuemin, S. Naihao, C. Zhicheng, Z. Zhiqin, G. Zhiyuan, M. Tao, Z. Dong, Z. Fengyuan, Z. Zhifeng, X. Xi , and L. Liangzhen, "Testing and Demonstration of a 10-kA HTS DC Power Cable," IEEE Transactions on Applied Superconductivity, Vol.24, No.2, April 2014, pages: 99-102, DOI: 10.1109/TASC.2013.2295845

[6.24] B. Yang, J. Kang, S. Lee, C. Choi, and Y. Moon, "Qualification Test of a 80 kV 500 MW HTS DC Cable for Applying Into Real Grid," IEEE Transactions on Applied Superconductivity, Vol.25, No.3, June 2015, DOI:10.1109/TASC.2015.2396683

[6.25] S. Kopylov, V. Sytnikov, S. Bemert, Yu Ivanov, I. Krivetskiy, M. Romashov, Yu Shakaryan,V. Keilin, A. Shikov, V. Patrikeev, V. Lobyntsev, and V. Shcherbakov, "HTS DC Transmission Line for Megalopolis Grid Development," IOP Publishing, Journal of Physics: Conference Series, Vol. 507, Part 3, 2014, 032047, http://iopscience.iop.org/1742-6596/507/3/032047

[6.26] S. Nishijima, S. Eckroad, A. Marian, K. Choi, W. S. Kim, M. Terai, Z. Deng, J. Zheng, J. Wang, K. Umemoto, J. Du, P. Febvre, S. Keenan, O. Mukhanov, L. D. Cooley, C. P. Foley, W. V. Hassenzahl, and M. Izumi "Superconductivity and the environment: a Roadmap, Long-distance DC transmission of green power," Superconductor Science and Technology topical review, Vol. 26, No. 11, 2013, DOI:0953-2048/26/11/113001

[6.27] S. Yamaguchi, H. Koshizuka, K. Hayashi, and T. Sawamura., "Concept and Design of 500 Meter and 1000 Meter DC Superconducting Power Cables in Ishikari, Japan" IEEE Transactions on Applied Superconductivity, Vol. 25, No. 3, June 2015, DOI: 10.1109/TASC.2015.2390045

7. LAYOUT OF THE HTS CABLE

Basically, there are two classifications of the HTS cable layout so called Cold Dielectric (CD) and Warm Dielectric (WD) which is shown in Figure 7.1 and Figure 7.2 respectively. In principle, these two configurations are possible, both for AC and DC cables; however, these configurations have been developed for AC cable rather than DC cables. Therefore, a massive conducting shield as for conventional MV, HV and EHV cables, added to HTS cable. This shield serves to equalize the electric field stress, to provide - in conjunction with a proper grounding system along the cable line - a return path for the cable neutral and fault current, and to provide shielding of electromagnetic field so as to reduce the EMI impact of the cable. To guarantee the smooth and chemically-compatible interfaces and to ensure a radial electric field profile within the insulation wall a semi-conducting layer is applied onto the inner and the outer surface of the dielectric.

7.1. COLD DIELECTRIC

In cold dielectric layout, electrical insulation is placed in the cryogenic environment. In this layout the conducting shield can be made by the superconductor since it is placed, along with the insulation, inside the cryogenic pipe. Using superconducting shield increases the required amount of SC material. In fact, depending on the connection of the shield at the cable terminals, the shielding current in AC condition can be in the same order of the transport current [7.1]. Therefore, the same amount of superconductor in the shield and the conducting core will be required. However, the superconducting shield operates with negligible losses, which is essential to keep the heat load of the cryogenic pipe within acceptable values [6.11].

In the case of the cold dielectric special insulation systems which can be operated reliably at cold environment have to use instead of the conventional insulation. Hybrid insulation based on pressurized Liquid Nitrogen (in the range 63-77 K) and Polypropylene Laminate Paper (PPLP) able to operate up to 275 kV in AC condition [7.2]-[7.6] and 80 kV in DC [6.24], have been successfully developed. The feasibility of hybrid insulation based on pressurized liquid hydrogen at 20 K and crepe paper, capable to operate up to 50 kV in DC condition, has also been demonstrated recently [6.22]. However, the fundamental investigation of breakdown characteristics of insulation under DC stress is currently in progress and is considered as one of the key factors for the development of high power HTS cable technology [6.11], [7.7] and [7.8].

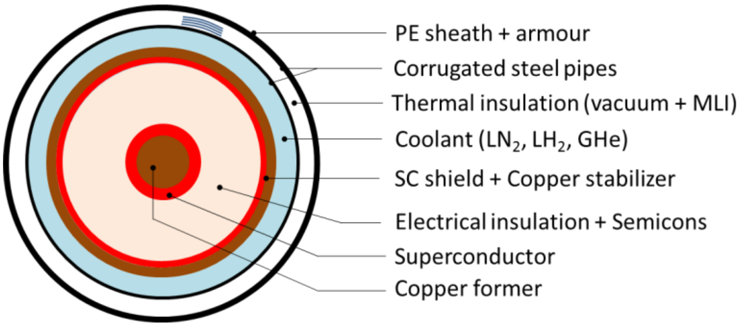

Figure 7.1 Layout of the cold dielectric superconducting cable [6.11]

7.2. WARM DIELECTRIC

In warm dielectric layout, both the insulation and the conducting shield are laid outside the cryogenic pipe and operate at ambient temperature. In this case insulation system simplifies where it can be realized with usual compounds, including extruded dielectrics [7.9]-[7.11]. Furthermore, a smaller perimeter of the cryopipe is obtained. Since the diameter of the cryopipe becomes smaller the heat radiation per unit length of the cable is lower and hence the heat load of the cable could be lower. Since the dielectric mass does not need to cool down, the cooling time will be reduced.

In the AC operation currents will be induced in the metal cryopipes and these pipes will act as the metal shield. The induced current will introduce losses in low temperature area and the efficiency of the cable will decrease greatly in turns it will make this system unsuitable for AC applications [6.15] and [7.12]. In the case of DC operation WD layout is an attractive choice for high voltage DC cables where there is no induced current, and the disadvantage of the WD layout will not relevant to the DC system. In the DC operation during the load changes transients occur, however the time duration of those transients are relatively short and significant induced current will not produce. The induced current in the cryopipes of the DC cables because of the harmonic component of the DC system due to the converters are the further source of induced currents. However, the superimposed harmonic currents have small amplitude and could be reduced further by means of the appropriate DC and AC side filters. Since the reduced harmonic component can be achieved the induced current on the cryopipe and the related losses can be kept within acceptable levels.

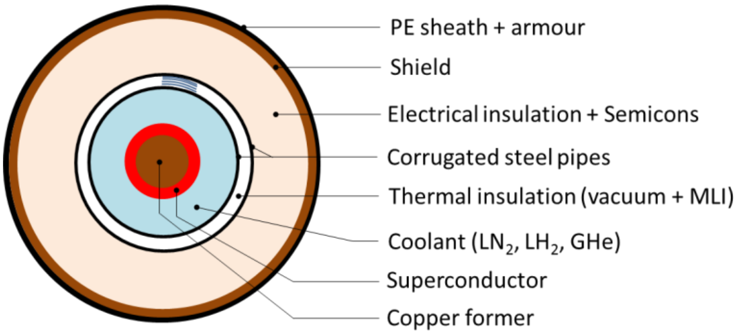

Figure 7.2 Layout of the warm dielectric superconducting cable [6.11]

7.3. TWO-STAGE COOLING

Two-stage cooling as shown in Figure 7.3 is a further possible layout of the HTS power cable. Overall cooling requirements of the MgB_2 cables can be reduced drastically with this layout, where the outer cooling stage (practically LN_2) acts as a thermal shield and the radiation heat load of the LH_2 pipe will be reduced. Additional heat must be removed from the LN_2 pipe which can be done with much higher efficiency due to the higher temperature. Concerning the dielectric it can be allocated either on the exterior of the LN_2 pipe (warm dielectric cable) or at interior of the LH_2 pipe. There is also the possibility to introduce the dielectric at the interior of LN_2 pipe. This could be an interesting solution for high voltage MgB_2 cables since reliable hybrid solid/liquid insulation technology has already been developed for LN_2 [6.11]. As it is discussed in [6.17], two-stage cooling by means of light hydrocarbons or ammonia can also be considered also for reducing the overall cooling power of LN_2 cooled cables.

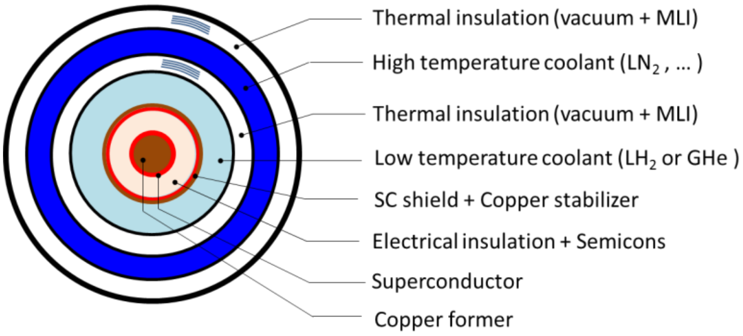

Figure 7.3 Layout of the cold dielectric superconducting cable with two stages cooling [6.11]

The main characteristics of cold and warm dielectric cables are compared in Table 7.1.

Table 7.1. Comparison of the characteristics of warm and cold dielectric SC cables [6.11]

	WARM	COLD
Perimeter of the pipe and heat load due to radiation	Low	High
Dielectric	Conventional	Special
During fault reliability of insulation	Normal	Critical (bubbling)
Amount of superconductor	Low	High
Cool down time	Short	Long
Cryostat and cooling system	High voltage	Conventional
Service Inductance	High	Low
Losses due to currents induced in the cryostat (AC operation)	High	Low

7.4. REFERENCES

[7.1] J. –H. Kim, M. Park, J. Cho, K. Sim, S. Kim, and I. –K. Yu, “Current Distribution Analysis of Conducting and Shield Layers of HTS Power Cable Under Utility Fault Condition,” IEEE Transactions on Applied Superconductivity, Vol. 19, No. 3, June 2009, pages: 1718-1721, DOI: 10.1109/TASC.2009.2018450

[7.2] J. F. Maguire, F. Schmidt, S. Bratt, T. E. Welsh, and Y. Jie, “Installation and Testing Results of Long Island Transmission Level HTS Cable,” IEEE Transactions on Applied Superconductivity, Vol. 19, No. 3, June 2009, pages: 1692 - 1697, DOI: 10.1109/TASC.2009.2018221

[7.3] H. Yumura, Y. Ashibe, M. Ohya, H. Itoh, M. Watanabe, T. Masuda, H. Ichikawa, T. Mimura, S. Honjo, T. Hara, R. Ohno, M. Shimoda, N. Nakamura, T. Komagome, and H. Yaguchi, “Update of YOKOHAMA HTS Cable Project,” IEEE Transactions on Applied Superconductivity, Vol. 23, No. 3, June 2013, DOI:10.1109/TASC.2013.2245931

[7.4] O. Maruyama, T. Ohkuma, T. Masuda, Y. Ashibe, S. Mukoyama, M. Yagi, T. Saitoh, T. Hasegawa, N. Amemiya, A. Ishiyama, and N. Hayakawa, “Development of 66 kV and 275 kV Class REBCO HTS Power Cables,” IEEE Transactions on Applied Superconductivity, Vol.23, No. 3, June 2013, DOI:10.1109/TASC.2012.2235497

[7.5] C. S. Weber, R. Lee, S. Ringo, T. Masuda, H. Yumura, and J. Moscovic “Testing and Demonstration Results of the 350 m Long HTS Cable System Installed in Albany, NY,” IEEE Transactions on Applied Superconductivity, Vol. 17, No. 2, June 2007, pages: 2038 – 2042, DOI: 10.1109/TASC.2007.899828

[7.6] M. Yagi, J. Liu, S. Mukoyama, T. Mitsuhashi, J. Teng, N. Hayakawa, W. Xudong, A. Ishiyama, N. Amemiya, T. Hasegawa, T. Saitoh, O. Maruyama, and T. Ohkuma, “Experimental Results of 275-kV 3-kA REBCO HTS Power Cable,” IEEE Transactions on Applied Superconductivity, Vol. 25, No. 3, June 2015, DOI:10.1109/TASC.2014.2385960

[7.7] In-jin Seo, Won Choi, Jae-gyu Seong, Bang-wook Lee, and Ja-yoon Koo, “Experimental and analytical study of the DC breakdown characteristics of polypropylene laminated paper with a butt gap condition considering the insulation design of superconducting cable,” Japanese Journal of Applied Physics, Vol. 53, No. 8S3, July 2014, 08NL04, http://iopscience.iop.org/article/10.7567/JJAP.53.08NL04

[7.8] W. J. Kim, S. H. Kim, H. J. Kim, J. W. Cho, J. S. Lee, and H. G. Lee, “The Fundamental Characteristics of PPLP as Insulating Material for HTS DC Cable,” IEEE Transactions on Applied Superconductivity, Vol.23, No.3, June 2013, DOI: 10.1109/TASC.2013.2244158

[7.9] M. Nassi, “Superconducting cable construction and testing,” EPRI and DOE Final Report 1000160, November 2000, http://goo.gl/LzQXRS

[7.10] M. Nassi, N. Kelley, P. Ladie, P. Corsato, G. Coletta, and D. Von Dollen, “Qualification results of a 50 m-115 kV warm dielectric cable system,” IEEE Transactions on Applied Superconductivity, Vol. 11, No. 1, March 2001, pages: 2355-2358, DOI: 10.1109/77.920334

[7.11] Ying Xin, Bo Hou, Yanfang Bi, Kunnan Cao, Yong Zhang, Songtao Wu, Huaikuang Ding, Guoling Wang, Qing Liu, and Zhenghe Han, “China's 30 m, 35 kV/2 kA ac HTS power cable project,” Superconductor Science and Technology, Vol. 17, No. 5, April 2004, DOI:10.1088/0953-2048/17/5/048

[7.12] H. Suzuki, T. Takahashi, T. Okamoto, N. Ishii, S. Mukoyama, and A. Kimura, “Verification Tests and Insulation Design Method of Cold Dielectric Superconducting Cable,” IEEJ Transactions on Power and Energy, Vol. 126-B, No. 4, April 2006, pages: 441 - 451, http://goo.gl/f5ex3T

[7.13] D. U. Gubser, “Superconductivity: an emerging power-dense energy-efficient technology,” IEEE Transactions on Applied Superconductivity, Vol. 14, No. 4, December 2004, pages: 2037-2046, DOI:10.1109/TASC.2004.838318

[7.14] N. Steve, M. Nassi, M. Bechis, P. Ladiè, N. Kelley, and C. Wakefield, “High temperature superconducting cable field demonstration at Detroit Edison,” Physica C: Superconductivity, Vol. 354, No. 1-4, May 2001, pages: 49-54, DOI:10.1016/S0921-4534(01)00021-1

[7.15] J. F. Maguire and J. Yuan, “Status of high temperature superconductor cable and fault current limiter projects at American Superconductor,” Physica C: Superconductivity, Vol. 469, No. 15-20, October 2009, pages: 874-880, DOI:10.1016/j.physc.2009.05.089

[7.16] H. X. Xi, W. Z. Gong, Y. Zhang, Y. F. Bi, H. K. Ding, H. Wen, B. Hou, and Y. Xin, “China’s 33.5 m, 35kV/2kA HTS ac power cable’s operation in power grid,” Physica C: Superconductivity, Vol. 445-448, page: 1054-1057, October 2006, DOI:10.1016/j.physc.2006.05.075

8. DESIGN METHODS OF HTS-DC CABLE SYSTEM

Simplified schematic of the DC HTS cable system is shown in Figure 8.1. The cable system with two monopoles with separate cryostat for closed loop coolant circulation is considered here. In the CD layout integration of two monopoles in a single cryostat is possible. In the latest case return path of the coolant should be integrated into the cryostat. Figure 8.2 illustrates the thermo-hydraulic system design of the cooling with two separate monopoles. The distance between the cooling stations L is one of the fundamental parameters for the design of the cable. In the case of CD layout the coolers and the cryopipes are at ground potential and are directly accessible. However, in case of WD layout they are at higher voltage with respect to the ground and cannot be accessed; high voltage insulating transformers are needed for the supply of the coolers, and high voltage maintenance should be planned [6.11].

Procedure for the HTS-DC cable design with considering the CD layout and one stage cooling is presented in this section. A simple extension in the case of WD layout or two stages cooling layout can be applied to the design procedure and it is not discussed here in detail. Extension for two monopoles in one cryostat is also possible.

The coolant at the controlled temperature T^{in} and pressure P^{in} is injected to the cryopipe at one cooling station and it is recooled at the next station (distance between the cooling station L is assumed). The outlet temperature of the cryopipe should not be more than a proper limit $T_{\text{max}}^{\text{out}}$ to assure the appropriate performance of the superconductor. Besides, the pressure at the outlet section should not be lower than the proper limit $P_{\text{min}}^{\text{out}}$ to avoid bubble formation in the coolant, therefore, appropriate heat exchange condition and appropriate performance of the insulation in case of cold dielectric design will be guaranteed [8.1]. The allowable temperature and pressure limits for the considered HTS-DC cables are listed in Table 8.1.

Table 8.1. Temperature and Pressure limits of the superconducting cable

	LN_2	LH_2
Inlet Temperature, T_{in}	65 K	20 K
Maximum Outlet Temperature, $T_{\text{max}}^{\text{out}}$	70 K	25 K
Inlet Pressure, P_{in}	20 bar	20 bar
Minimum Outlet Pressure, $P_{\text{min}}^{\text{out}}$	5 bar	5 bar

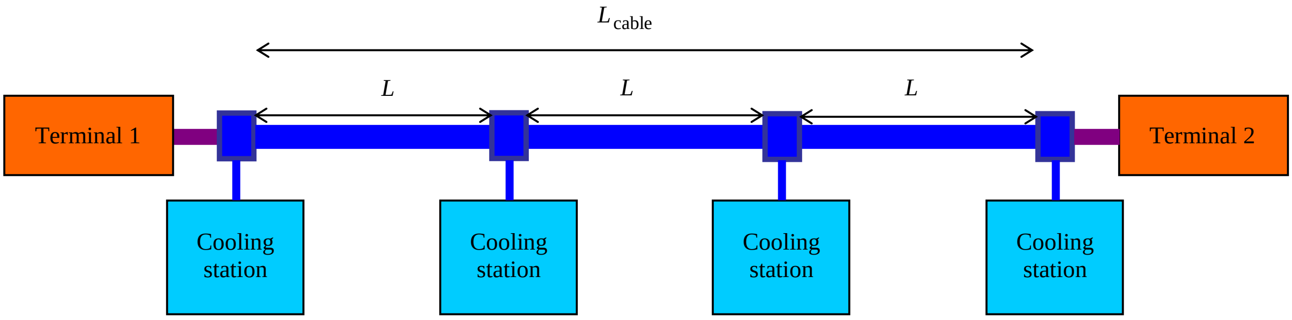

Figure 8.1 Schematic of the HTS cable system. L_{cable} is the total length of the cable and L is distance between cooling stations

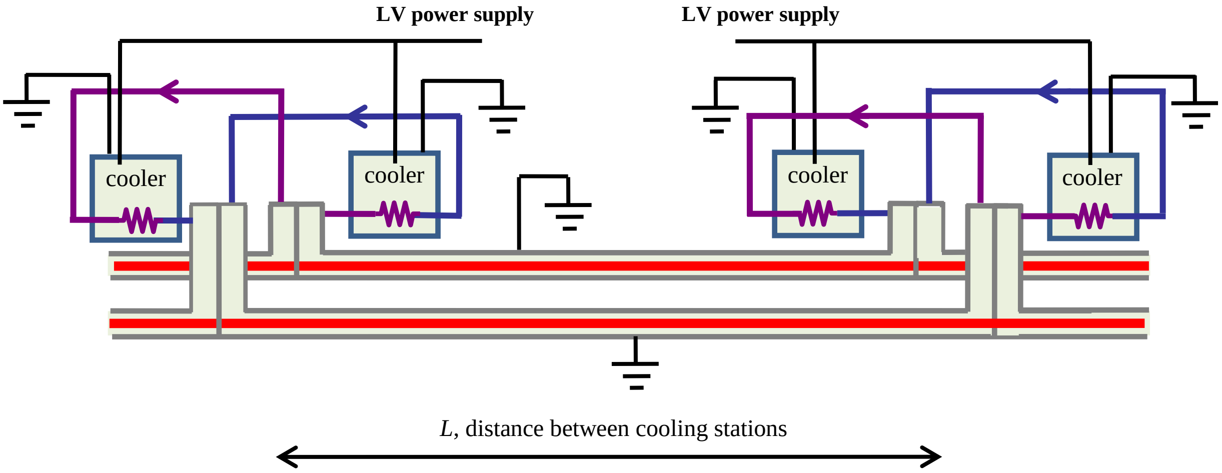

Figure 8.2 Thermo-hydraulic circuit for the cooling of the HTS cable (CD layout)

8.1. RADIUS OF THE FORMER

The former of the HTS cable is made of copper and also with possible steel reinforcement core provides the manufacturability, mechanical support, stabilizing of the cable, and fault withstands purpose [6.11]. Layers of superconducting tapes winded on a copper former makes the core of the superconducting cable. Although, the fault current flows through the former; following fault current produces heat in the former and will increase the temperature. Since the insulation in CD layout depends on the coolant, no bubble should occur in the coolant, otherwise the insulation and in turns the cable will damage. In the other word the temperature at the end of the fault should be below the boiling temperature at the operating pressure range. The higher operating pressure of the coolant allows a larger temperature margin before bubbles formation. For example a temperature increase of about 20 K (from 75 K) is admissible for liquid nitrogen at 5 bars, whereas at 1 bar the admissible increase is about 2 K [8.2]. The minimum copper area A_f of the former can be obtained by stating the adiabatic energy balance (per unit length) of during the fault:

$$A_\mathrm{f} \int_{T_\mathrm{n}}^{T_\mathrm{boiling}} c\, dT \geq \int_0^{\Delta t_\mathrm{f}} \frac{1}{\sigma} \frac{i^2}{A_\mathrm{f}} dt \qquad (8.1)$$

where c is the specific heat of copper, σ is the electric conductivity of copper, and T_n is the maximum admissible operating temperature of the cable. The area of the copper former depends on the fault current i through the former and the duration Δt_f of the fault, the latest parameter are depending on the grid where the cable is installed. Typical values of the radius of the copper former are in the range 5-20 mm [7.3], [7.6], and [8.3]. In [7.3] it is shown that a copper cross section area of 400 mm^2 is enough to tolerate 63 kArms AC fault current for 0.6 s with a temperature increase of 20 K.

8.2. THICKNESS OF SUPERCONDUCTOR

In this study, the design of the cable based on two commercially available superconductors of 2G HTS (YBCO coated conductors) and MgB_2 is considered: a YBCO tape with 12 mm width and 0.1 mm thickness produced by Superpower Inc. and an MgB_2 tape with 3 mm width and 0.5 mm thickness coated conductor produced by Columbus Superconductors SpA. Figure 8.3 shows the critical engineering current density of these conductors in the operating temperature range as a function of the magnetic field. Data of are taken from [8.4] for YBCO and from [8.5] for MgB_2.

The detailed design of the superconducting part of the cable is beyond the scope of this thesis and will not address here. Instead, the preliminary sizing criteria of the superconducting section are given with the aim to arrive at the overall dimension of the core. The dimension of the cable core is used as input for the thermo-hydraulic design of the cable in section 8.5 and for estimating the needed amount of superconducting materials. The copper former and several layers of the superconductor tapes winding around the former make the conducting core of the cable. In the case of the MgB_2, round wires are available which can be used in the alternative, along with copper wires, for manufacturing the cable core in the form of helically stranded rope [6.21].

For minimizing the AC losses and distribution of the current between the layers in the cable, different winding angles should be chosen for the different layers of superconductor [8.3] and [8.6]. The gross thickness of the superconducting part of the cable is indicated with $\delta_\mathrm{SC,core}$ here. It should be noticed that the HTS tapes only fill a fraction β of the cross section; the other fraction of the superconducting section consists of the spacing between the tapes in the layers for AC loss reduction and possible carbon paper or insulation between layers [8.3] and [8.7]. Typical values of the filling factor β, as they can be estimated from [7.4] and [8.6], are in the order of 0.6-0.7. In the following β = 0.6 is assumed. The average engineering current density of the superconductor and the maximum magnetic field acting on it can be estimated as

$$J = \frac{I_{\mathrm{dc}}}{\beta\pi((R_{\mathrm{f}} + \delta_{\mathrm{SC,core}})^2 - R_{\mathrm{f}}^2)\cos(\alpha)} \tag{8.2}$$

$$B_{\mathrm{max}} = \mu_0 \frac{I_{\mathrm{dc}}}{2\pi(R_{\mathrm{f}} + \delta_{\mathrm{SC,core}})} \tag{8.3}$$

where I_{dc} is the rated DC current of the cable, R_f is the radius of the former, α is the average winding angle of the layers. As a first approximation, it is assumed that the magnetic field is oriented in parallel to the tape. Since the winding angle is typically in the range of 10°-20° [8.3] and [8.7], the impact of the cos(α) term is in the order of few percents of the denominator and it is neglected. The thickness of the SC section is obtained by merging equations (8.2)-(8.3) and by imposing that the engineering current density is a fraction γ of the critical engineering current density of the conductor at the maximum operating field and temperature, and it can achieve by solving the following equation.

$$\frac{I_{\mathrm{dc}}}{\beta 2\pi R_{\mathrm{f}}\, \delta_{\mathrm{SC}}} = \gamma J_c\left(\mu_0 \frac{I_{\mathrm{dc}}}{2\pi(R_{\mathrm{f}} + \delta_{\mathrm{SC}})}, T_{\mathrm{max}}^{\mathrm{out}}\right) \tag{8.4}$$

where $T_{\mathrm{max}}^{\mathrm{out}}$ is specified in Table 8.1 and the dependence of J_{c} on B is illustrated in Figure 8.3. In the following γ = 0.7 is assumed. Given the thickness $\delta_{\mathrm{SC,core}}$ the corresponding length L_{SCcore} of SC conductor needed per unit length of cable is obtained by dividing the effective cross section of superconductor by the area of the tape, i.e.

$$L_{\mathrm{SC,core}} = \frac{\beta 2\pi R_{\mathrm{f}}\, \delta_{\mathrm{SC,core}}}{S_{\mathrm{tape}}} \tag{8.5}$$

In the following S_{tape} = 12×0.1 mm^2 for YBCO and S_{tape} = 3×0.5 mm^2 for MgB_2 is assumed. This does not mean that the cable has to be manufactured with these conductors. In fact, tapes with different size, all with the same *J-B* performance of Figure 8.3, can be manufactured and used. Hence equation gives the equivalent amount of tape with 12×0.1 mm^2 or 3×0.5 mm^2 section which is needed for the manufacturing of the YBCO and the MgB_2 cable respectively.

As mentioned before the described procedure only gives a preliminary estimation which needs to be verified with more accurate calculation of the magnetic field by numerical methods. Accurate calculation is particularly important in the YBCO case where the critical current density rapidly deteriorates if the perpendicular magnetic field to the tape exists [6.11]. Nevertheless, after verification even if it is found that the effective *J*/*J*c margin is not sufficient and some more SC should be added the overall dimension of the geometry of the cable core, and consequently the thermo-hydraulic design of the cable discussed in section 8.5 does not change appreciably [6.11].

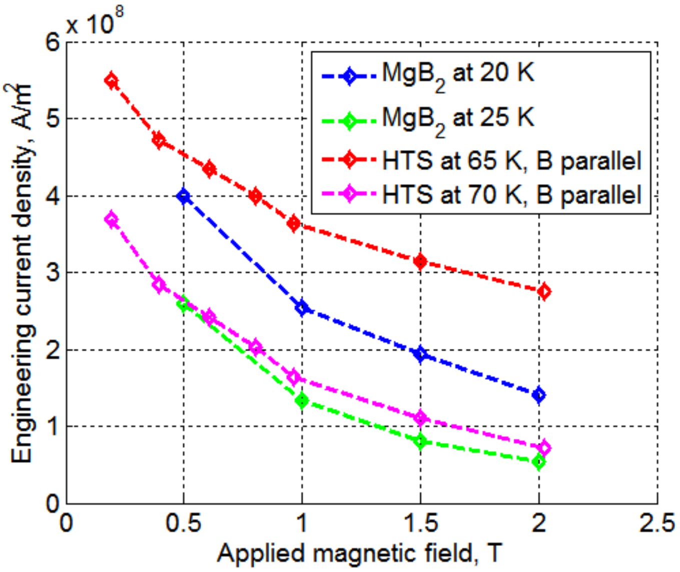

Figure 8.3 Critical engineering critical current density J_e of commercial

8.3. THICKNESS OF INSULATION

The thickness δ_{ins} of the insulation needed to withstand a rated voltage V_{dc} can be calculated as [8.6]:

$$\delta_{\text{ins}} = (R_{\text{f}} + \delta_{\text{SC,core}})\left(e^{\frac{V_{\text{dc}}}{\eta E_{\text{b}} (R_{\text{f}} + \delta_{\text{SC,core}})}} - 1\right) \tag{8.6}$$

where E_b is the breakdown voltage of the insulation and η is an appropriate safety margin. A breakdown voltage E_b = 20 kV / mm can be assumed for LN_2/PPLP [8.6] in AC condition and has also been assumed for LH_2/paper insulation subject to DC operation [6.22], so this value is assumed. A conservative safety margin $\eta = 0.3$ is assumed due to the DC operation [6.11].

8.4. THICKNESS OF HTS SHIELD AND COPPER STABILIZER

The same cross section area of superconductor as in the conducting core of the cable (see section 8.2) is used for the shield as well. The thickness $\delta_{\mathrm{SC,shield}}$ is derived accordingly. Similarly, the same cross section area of copper as for the former (see section 8.1) is used for the shield's stabilizer as well. The thickness $\delta_{\mathrm{cu,shield}}$ is derived accordingly.

8.5. THERMO-HYDRAULIC DESIGN OF THE CRYOPIPE

Based on the balance of mass, momentum and energy the accurate coolant flow equations inside the cryogenic pipe can be derived [8.8] and [8.9]. Since the length of the pipe is more than the transversal dimension a 1D model can be used [6.11]. By assuming the incompressible fluid in the cryogenic pipes, the gradients of pressure and temperature along the length of the line are given as follows [8.8]-[8.10]:

$$\frac{\partial P}{\partial x} = -\frac{f}{D_{\mathrm{h}}}\frac{\rho v^2}{2} \tag{8.7}$$

$$\frac{\partial T}{\partial x} = \frac{f}{D_{\mathrm{h}}}\frac{v^2}{2c_{\mathrm{p}}} + \frac{q}{\dot{m}c_{\mathrm{p}}} \tag{8.8}$$

where v and $\dot{m}$ are the velocity and the mass flow rate of the fluid respectively, ρ is the mass density, c_{p} is the specific heat at constant pressure, D_{h} is the equivalent hydraulic diameter and f is the friction factor. For the concentric cable geometries of Figure 7.1-Figure 7.3 the hydraulic diameter (i.e. the ratio between the cross section of the coolant and total inner and outer perimeter) is given by $D_{\mathrm{h}} = D_{\mathrm{o}} - D_{\mathrm{i}}$ where D_{i} and D_{o} are the inner and the outer diameter of the coolant cross section respectively. The inner diameter D_{i} is obtained from the electromagnetic design of the cable (see sections 8.1-8.4) as

$$D_{\mathrm{i_{CD}}} = 2\left(R_{\mathrm{f}} + \delta_{\mathrm{SC,core}} + \delta_{\mathrm{ins}} + \delta_{\mathrm{SC,shield}} + \delta_{\mathrm{SC,shield}}\right) \tag{8.9}$$

$$D_{\mathrm{i_{WD}}} = 2\left(R_{\mathrm{f}} + \delta_{\mathrm{SC,core}}\right)$$

In equation (8.9) $D_{\mathrm{i_{CD}}}$ is the inner diameter of coolant cross section in CD layout and $D_{\mathrm{i_{WD}}}$ is the inner diameter of coolant cross section in WD layout. In equation (8.8) the term q is the total heat load of the unit length of the cable (W/m), which can be expressed as

(8.10) $$q = \lambda \pi D_\mathrm{o} + q_\mathrm{em}$$

where λ is the heat load per unit surface ($\mathrm{W/m^2}$) due to radiation and q_em is the heat load per unit length due to the electromagnetic loss occurring in the cable. In DC operation of the cable, the first contribution is dominant and the electromagnetic loss can be neglected. The typical data of the radiation heat load which can be obtained with the present state of the art hybrid (vacuum + multilayer) thermal insulation technology are listed in Table 8.2 for different operating temperatures [6.18]. From Table 8.2 it is clear that the heat load depends very little on the cold temperature T_2 and reduces drastically with the decrease of the hot temperature T_1. In particular, it can be seen that two stages LN_2/LH_2 cooling is able to drastically reduce the heat load of LH_2.

Table 8.2. Heat load λ per unit surface due to radiation ($\mathrm{W/m^2}$) through hybrid vacuum + multilayer (30 layers) thermal insulation [6.18]

	T_1, K	T_2, K	λ, $\mathrm{W/m^2}$
from room temperature to LN_2	300	77	1.195
from room temperature to LH_2	300	21	1.235
from LN_2 to LH_2	77	21	0.040

The friction factor f in equations (8.7)-(8.8) depends both on the flow velocity and the hydraulic diameter. It can be estimated by solving the following Colebrook-White implicit equation [8.8]

(8.11) $$\frac{1}{\sqrt{f}} = -2\log_{10}\left(\frac{\varepsilon / D_\mathrm{h}}{3.71} + \frac{2.52}{N_\mathrm{Re}\sqrt{f}}\right) \quad \text{with} \quad N_\mathrm{Re} = \frac{\rho v D_\mathrm{h}}{\mu}$$

where ε the roughness of the pipe, N_Re is the Reynolds's number and μ is the dynamic viscosity. For corrugated stainless steel pipes the friction factor can be assumed as four times the one of the smooth pipe ($\varepsilon = 0$) with the same diameter [8.8]. This implies that the friction factor of corrugated pipes can be obtained by solving the following implicit equation

(8.12) $$\frac{1}{\sqrt{f}} = -\log_{10}\left(\frac{5.02}{N_\mathrm{Re}\sqrt{f}}\right) \quad \text{with} \quad N_\mathrm{Re} = \frac{\rho v D_\mathrm{h}}{\mu}$$

Equations (8.7), (8.8) and (8.12) should be solved numerically since the specific heat c_p, the density ρ and the dynamic viscosity μ are depending both on temperature and pressure. However, by choosing the average values for the $\bar{c}_p$, $\bar{\rho}$ and $\bar{\mu}$ within the operating temperature and pressure range and substituting them in equations (8.7), (8.8) and (8.12) the following expression of the average temperature and pressure gradients can be obtained by considering $D_\mathrm{h} = D_\mathrm{o} - D_\mathrm{i}$ and $v = \dot{m} / \bar{\rho}\pi(D_\mathrm{o}^2 - D_\mathrm{i}^2)$, and can be used for the preliminary design of the pipes

(8.13) $$\frac{\Delta P}{\Delta x} = -\frac{f\,\dot{m}^2}{2\pi^2\bar{\rho}\left(D_\mathrm{o} - D_\mathrm{i}\right)\left(D_\mathrm{o}^2 - D_\mathrm{i}^2\right)^2}$$

(8.14) $$\frac{\Delta T}{\Delta x} = \frac{f\,\dot{m}^2}{2\pi^2\,\bar{c}_\mathrm{p}\,\bar{\rho}^2\left(D_\mathrm{o} - D_\mathrm{i}\right)\left(D_\mathrm{o}^2 - D_\mathrm{i}^2\right)^2} + \frac{\lambda\,\pi\,D_\mathrm{o} + q_\mathrm{core}}{\dot{m}\,\bar{c}_\mathrm{p}}$$

(8.15) $$\frac{1}{\sqrt{f}} = -\log_{10}\left(\frac{5.04\bar{\mu}\,\pi\left(D_\mathrm{o} + D_\mathrm{i}\right)}{\dot{m}\,\sqrt{f}}\right)$$

The average mass density, specific heat and dynamic viscosity of LN_2 and LH_2 in the operating temperature and pressure intervals are listed in Table 8.3 those data are drawn from [8.8]-[8.10]. Equations (8.13)-(8.15) points out that two degrees of freedom can be used for regulating the average pressure and temperature gradients in the cryopipe: the outer diameter D_o and the mass flow $\dot{m}$ of the liquid coolant (as mentioned before, the inner diameter is fixed by the electromagnetic design of the cable core, see equation (8.9)).

Table 8.3. Average physical properties of LN_2 and LH_2 in the operating temperatue and pressure range (see Table 8.1)

	LN_2	LH_2
Mass density, kg/m^3	839	72.23
Specific heat, J/kg K	2662	9169
Dynamic viscosity, μPa*s	25.08	15.70

The isogradient curves of LN_2 in the D_o - $\dot{m}$ are shown as an example in Figure 8.4. Similar curves are obtained for LH_2. As mentioned before the length of the cryogenic pipes which is the distance between the cooling stations is indicated by the L, thus, the maximum allowable gradient of pressure and temperature are given by

(8.16) $$\left.\frac{\Delta P}{\Delta x}\right|_\mathrm{max} = \frac{P^\mathrm{in} - P^\mathrm{out}_\mathrm{min}}{L}$$

(8.17) $$\left.\frac{\Delta T}{\Delta x}\right|_\mathrm{max} = \frac{T^\mathrm{out}_\mathrm{max} - T^\mathrm{in}}{L}$$

For any assigned distance L the choice of D_o and $\dot{m}$ the average gradient given by equations (8.13)-(8.15) should be well below the admissible values expressed by equations (8.16)-(8.17). The final choice of outer diameter and mass flow can be made by means of the following procedure which is further explained in Figure 8.5:

- Minimum $D_{\mathrm{o\,min}}$ and $\dot{m}_{\mathrm{min}}$ are found at the intersection of the curves with maxim allowable pressure and temperature gradients.
- The reference outer diameter $D_{\mathrm{o\,ref}}$ is chosen with an appropriate safety margin (i.e. $D_{\mathrm{o\,ref}} = \xi D_{\mathrm{o\,min}}$; ξ=1.3 is used in the following).
- An admissible interval of mass flow is obtained corresponding to $D_{\mathrm{o\,ref}}$. The reference mass flow $D_{\mathrm{o\,ref}}$ is chosen in the middle of this interval.

It is should be noted here that both the reference outer diameter and mass flow increase with the distance L between the cooling stations.

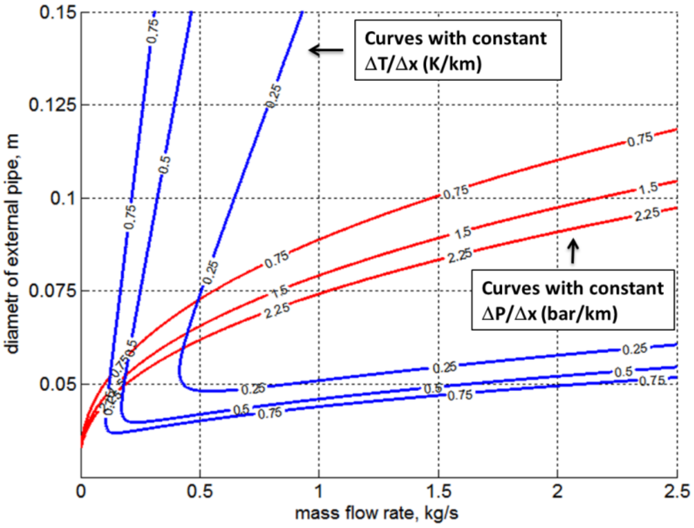

Figure 8.4 Examples of isogradient curves for LN_2 obtained from equations (8.13)-(8.15) with D_i= 30 mm [6.11]

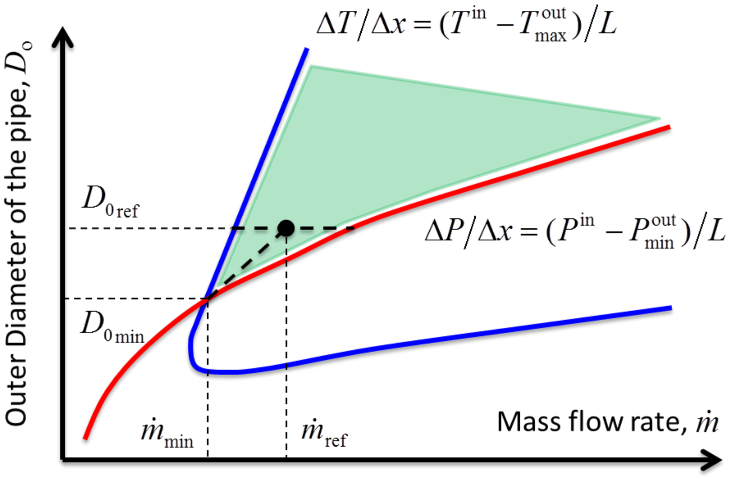

Figure 8.5 Choice of the outer diameter and mass flow for a given distance L between the cooling stations [6.11]

8.6. TERMINATIONS

A further contribution to the overall heat load comes from the terminations which are schematically shown in Figure 8.6 for the YBCO and the MgB_2 cable. In the latter case an intermediate section made of 1G or 2G HTS materials is introduced between the copper lead and the cable core in order to reduce the heat invasion at low temperature. A heat inrush occurs through the copper lead to HTS stage, which operates at 77 K and is cooled by closed loop circulation of liquid nitrogen. A dedicated cooling system for the termination is appropriate also in case of LN_2 / YBCO system [6.17]. The typical value of the heat load of one single termination is around 50 W/kA from 300 K to 77 K and 0.5 W/kA from 77 K to 20 K [6.19].

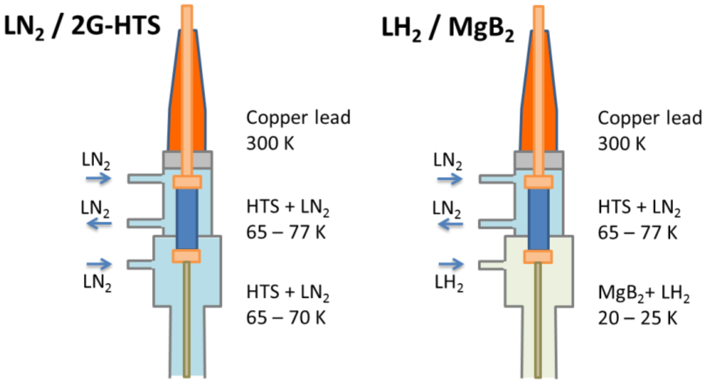

Figure 8.6 Scheme of the terminations of the YBCO and the MgB_2 cable [6.11]

8.7. TOTAL COOLING POWER

The total power required for the cooling of the DC cable is given by

$$P_{\text{cooling}} = COP_{\text{cryopipe}} \lambda \pi D_o(L) L_{\text{cable}} + COP_{\text{terminations}} P_{\text{terminations}} \quad (8.18)$$

As mentioned before, since the electromagnetic losses of the cable core in DC operation is not significant enough, this loss is neglected in equation (8.18). It is should be mentioned that, since the outer diameter of the cryopipe increases with the distance *L* between the cooling station, the cooling power per unit length of cryopipe increases as well. The values of the COP that are assumed in the following for evaluating the cooling power of the cable are listed in Table 8.4. The corresponding percentage of Carnot efficiency is also reported.

The last point which should be mentioned here is that the transport current of the cable, and hence the transmitted power at the considered voltage level, only affect the thickness of the required superconductor. This has a very small influence on the overall dimension of the cable and hence, on the heat load. In the other word, the cooling power of the HTS-DC cable is practically independent of the transmitted power.

Table 8.4. Coefficient of performance of the cooling system

	COP	% of Carnot
from LN_2 to room temperature	22	15%
from LH_2 to room temperature	110	10%
from LH_2 to LN_2	21	10%

8.8. REFERENCES

[8.1] F. Schmidt and A. Allais "Superconducting cables for power transmission applications-a review", Workshop on Accelerator Magnet Superconductors (WAMS 2004), 22-24 March, Archamps, France, 2004, http://goo.gl/lwk8l5

[8.2] H. –M. Chang, Y. S. Choi, S. W. Von Sciver, and K. D. Choi, "Cryogenic cooling system of HTS transformers by natural convection of subcooled liquid nitrogen," Cryogenics, Vol. 43, No. 10-11, October-November 2003, pages: 589–596, DOI:10.1016/S0011-2275(03)00168-1

[8.3] Y. Wang, Y. Zheng, L. Hongwei, D. Shaotao, Z. Huiyuan, G. Xiaojin, T. Yi, Z. Lianqi, X. Jiping, and L. Liangzhen, "A Novel Approach for Design of DC HTS Cable", IEEE Transactions on Applied Superconductivity, Vol. 21, No. 3, June 2011, pages: 1042-1045, DOI: 10.1109/TASC.2010.2089595

[8.4] D. W. Hazelton, "SuperPower 2G HTS Conductor," 1st Workshop on Accelerator Magnets in HTS (WAMHTS-1) - Hamburg, Germany, May 21, 2014, http://goo.gl/k7AnGG

[8.5] G. Grasso - Columbus Superconductors, "In field performance of MgB_2 wires", April 2014, private communication

[8.6] S. S. Kalsi "Applications of High Temperature Superconductors to Electric Power Equipment," Wiley-IEEE Press, April 2011, pages: 219-259, ISBN: 978-0-470-16768-7

[8.7] N. Amemiya, J. Zhenan, M. Nakahata, M. Yagi, S. Mukoyama, N. Kashima, S. Nagaya, and Y. Shiohara, "AC Loss Reduction of Superconducting Power Transmission Cables Composed of Coated Conductors," IEEE Transactions on Applied Superconductivity, Vol. 17, No. 2, June 2007, pages: 1712-1717, DOI:10.1109/TASC.2007.898442

[8.8] L. Trevisani, "Design and simulation of Large scale energy storage and power transmission system for remote renewable source exploitation," Doctoral Thesis, University of Bologna, 2006, Online: http://goo.gl/f97DyO

[8.9] L. Trevisani, M. Fabbri, and F. Negrini, "Long distance renewable-energy-sources power transmission using hydrogen-cooled MgB2 superconducting line," Cryogenics, Vol. 47, No. 2, February 2007, Pages 113-120, DOI:10.1016/j.cryogenics.2006.10.002

[8.10] A. M. Wolsky, "HTS Cables: Status, Challenge and Opportunity," IEA Report, December 2004, http://goo.gl/P05y9w

PART III. APPLICATION OF THE SUPERCONDUCTIVITY IN POWER SYSTEM: CASE STUDIES

9. MULTIFUNCTIONAL 1 MW - 5 S SMES SYSTEM

In this chapter the feasibility of a real scale 1 MW - 5s SMES based on state of the art HTS materials is investigated. Second generation HTS materials (YBCO coated conductors) are considered since they offer high in-field performance and their cost is expected to reduce substantially in the near future. Feasibility of SMES based on magnesium diboride (MgB_2) is also considered, since this material, despite the lower performance, is promptly available at industrial length (wire length up to 4 km and global productivity of 3000 km/year) and at competitive costs [9.1].

The design of the SMES coil and the power electronic interface of the SMES are discussed previously in chapter 3 to 5. The design of the SMES system should be done simultaneously by considering the coil design and power electronics interfaces, since they have great interaction between each other. Especially for insulation design of the SMES where the voltage transients because of the normal and abnormal operation of the SMES coil could cause failure.

9.1. MAIN SPECIFICATIONS OF THE SMES SYSTEM

A SMES system able to deliver a power of 1 MW for time duration of 5 s is considered. This system can be used for several applications in the industry, including the voltage sag protection of critical loads and the leveling of large impulsive load. The relatively long supply time (5 s) can also be exploited for bridging the time required by offline power reserve like, for example, diesel generators. A further application is the increase of the transient peak power capacity of energy intensive storage systems (batteries). Additional network service such as power factor correction and harmonic compensation can also be carried out by means of the SMES system during normal condition (though the storage capacity is not strictly exploited for this purpose). SMES systems with this rating are also considered by other research groups. More details on the application of the considered SMES are given in section 9.5.3.

The SMES consists of a superconducting coil connected to the grid by means of a solid state power conditioning system (PCS). The details of the power conditioning system and the control algorithm are discussed in section 9.5.1. The coil is connected to a DC capacitor bus by means of a two quadrant chopper. The insulation level of the coil should be able to withstand the voltage chosen for the DC bus. Since a conduction-cooling system is considered for the coil, a hybrid solid/vacuum insulation system (Kapton with Epoxy impregnation) is to be used. Voltage withstands capability up to 10 kV has been reported for conduction-cooled coils with solid/vacuum insulation [9.2] and [9.3]. The nominal voltage of 1 kV is chosen in the following for the DC bus, which is typical for MW level power electronic equipment and is well below withstand capability of dry coil. The minimum current which allows the SMES to deliver the required power P is given by $I_{\mathrm{min}} = P/V_{\mathrm{dc}}$, which in the present case gives $I_{\mathrm{min}} = 1$ kA. This means that the coil cannot be discharged below I_{min} if the delivery of the power P has to be guaranteed (it should be noted that the coil can be completely discharged but at a lower power). The main design parameters of the SMES are resumed in Table 9.1.

Table 9.1. Main characteristics of the SMES

Deliverable Power, P	1 MW
Duration of delivery, Δt	5 s
Deliverable Energy, ΔE	5 MJ
Voltage of the DC bus, V_{dc}	1 kV
Minimum Current, I_{min}	1 kA

9.2. SMES COIL DESIGN

The design procedure of the magnet which is discussed in section 4.2 is used for the design of the three following SMES systems

- 1 MW / 5 s SMES system with 3 T reference field based on MgB_2
- 1 MW / 5 s SMES system with 3 T reference field based on YBCO
- 1 MW / 5 s SMES system with 8 T reference field based on YBCO

The main characteristics of the conductors (i.e. YBCO and MgB_2) are discussed in details in section 4.1.

As it is discussed in section 4.2 and depicted in Figure 4.3 - Figure 4.6, for a reasonable compromise a maximum current $I_{\mathrm{max}} = 3$ kA is chosen. With this maximum current the required deliverable energy $\Delta E = 5$ MJ can be met with a number of turns $N = 2660$ and a thickness $\delta_{\mathrm{sol}}= 23.4$ mm in the case of 3 T reference field based on MgB_2. The corresponding maximum storable energy is $E_{\mathrm{max}} = 5.6$ MJ (see Figure 4.3). The required length of MgB_2 wire is 159.6 km (see Figure 4.4). Note that if a maximum current $I_{\mathrm{max}} = 2$ kA were chosen the values $N = 4249$ and $\delta_{\mathrm{sol}}= 29.0$ mm would have been obtained, corresponding to the maximum storable energy of 6.6 MJ and a length of MgB_2 wire of 199.2 km. On the contrary, if a maximum current $I_{\mathrm{max}} = 4$ kA were chosen the values N = 1954 and δ_{sol}= 21.9 mm would have been obtained, corresponding to the maximum storable energy of 5.3 MJ and a length of MgB_2 wire of 149.5 km.

By applying the discussed procedure in section 4.2 the input parameters and the output characteristics of the solenoid coil designed for these three SMES systems are listed in Table 9.2. A filling factor of 0.9, which apply for coils made of circular wires with hexagonal winding pattern, is assumed for the MgB_2 SMES. A filling factor of 0.75, which is typical for practical Roebel cables, is assumed for the YBCO SMES.

Table 9.2. Main characteristics and designed characteristics of the 1 MW / 5s SMES System

Voltage of the DC bus, V_{dc}	1 kV
Minimum Current, I_{min}	1 kA
Operating temperature of the superconductor	16 K
Aspect ratio of the solenoid	4
Filling factor of the solenoid	0.9 for MgB_2 and 0.75 for YBCO
J/J_c ratio of the SC conductor	0.65

SC material	MgB_2	YBCO	
Reference magnetic field	3 T	3 T	8 T
Diameter of the solenoid	763 mm	763 mm	397 mm
Height of the solenoid	3052 mm	3052 mm	1587 mm
Thickness of the solenoid	23.4 mm	5.7 mm	22.1 mm
Maximum Current, I_{max}	3 kA	3 kA	3 kA
Magnetic field of the solenoid at I_{max} (*axial component at the center*)	3.19 T	3.24 T	8.37 T
Max axial field on the conductor at I_{max}	3.20 T	3.25 T	8.39 T
Max radial field on the conductor at I_{max}	2.40 T	3.18 T	5.53 T
Max tensile stress on the conductor	15.8 MPa	52.8 MPa	73.5 MPa
Number of turns	2660	2713	3661
Inductance	1.25 H	1.25 H	1.25 H
Total energy of the solenoid at I_{max}	5.62 MJ	5.62 MJ	5.62 MJ
Deliverable energy ($I_{max} - I_{min}$)	5.0 MJ	5.0 MJ	5.0 MJ
Length of SC cable	6.6 km	6.6 km	4.8 km
Length of SC conductor	159.6 km	53.9 km	59.2 km

The main characteristics of the three designed SMES systems are listed in Table 9.2. It can be seen from the table that in all cases the maximum tensile stress is well below the critical tensile stress of the materials reported in Table 4.1 and Table 4.2, so no mechanical concerns exists for the proposed solutions. As expected, for operation at the same field level (3 T), the amount of material needed is much higher (about 3 times) for MgB_2 due to its lower J_c-B performance. Nevertheless, since a factor of about 1/8 exists between the costs per unit length of the considered MgB_2 and YBCO conductors today, the overall cost of the material is about 160 % higher for YBCO. If the high field design (at 8 T) is chosen for the YBCO a reduced overall size of the coil is obtained which requires less amount of the conductor. On the other hand, more ampere-turns at reduced J_c

are needed which require more conductor. In conclusion, an increase of the amount of conductor (of about 10 %) is eventually obtained if the high field is chosen as it can be seen from Table 9.2. Furthermore, as it is discussed in section 4.3 (the result is discussed in section 9.3), severe limitations exist for the high field design due to the increase of AC losses. Also numerical calculation verifies that the amount of conductor increases with the aspect ratio of the solenoid, which is one of the degrees of freedom of the design. However, as the stray field also increases with the aspect ratio, a compromise value of 4 was chosen. Note that, no matter the material or the field level chosen, the inductance of the SMES is 1.25 H, if the proper switching frequency is chosen.

9.3. AC LOSS CALCULATION IN THE COIL

AC loss is the major concern for HTS-SMES technology. In order to reduce the AC losses subdivision of the HTS section of the conductors in a number of fine twisted filaments is essential [4.14]-[4.16]. MgB_2 conductors made of tens or hundreds of twisted filaments can easily be produced by means of the PIT technique [4.14]. As for the YBCO, multifilamentary architecture can be obtained by means of, e.g., striations and electroplating [4.15] and [4.16]. No twisting is possible, however in this case. For the present study, it is assumed that the MgB_2 and the YBCO conductor are made of 361 and 10 filaments respectively. These conductors can be manufactured by means of nowadays industrial processes [4.14]-[4.16]. The discussed methods for calculating the AC losses are applied for full power discharge / charge cycle is depicted in Figure 4.7. The 2D modeling of the superconductor which is discussed in [4.17] is used.

Only the losses within the superconductor due to transport current and applied field (with given orientation) were considered. The E-J power law was used to model both the superconductors. n-values of 30 and 20 were assumed for the YBCO and the MgB_2 respectively. The possible dependence of the n-value on the operating conditions of the SMES (field level, mechanical strength) is not taken into account [9.4]. The dependence of the critical current density on the magnetic field was taken into account. Possible losses due to coupling between the filaments and eddy currents in the normal conducting matrix were not considered. No additional losses in metallic parts (e.g. copper plates or braids for the thermal connection of the coil with the cryocoolers) were taken into account. Furthermore, losses were calculated under the assumption that the total current is equally shared between the conductors of the assembled cable (Rutherford or Roebel), which is realistic due to continuous transposition. It was also assumed, as a first approximation, that the current of each of the conductors is equally shared between the filaments. This latter assumption might not be accurate in the case of YBCO coated conductors since filaments are untwisted.

Corresponding value of losses should hence only be used as estimation. 3D modeling of a wide portion of the coil is need for more accurate prediction.

The total loss of the coil is obtained by integrating the distribution of Figure 4.8 and is reported in Table 9.3 as well. The heat capacity per unit length of the conductor at the operating temperature of the SMES is also reported in Table 9.3. This was obtained by taking the weighted average of the heat capacities of the constituent materials of the composite conductor. Data for YBCO tape were taken from [4.13]. Data for the MgB_2 wire were taken from the CRYOCOMP database. In the case of YBCO at 3 T very high losses (434 mJ/m) are obtained at the end of the coil due to the perpendicular component of the field. The losses in the central part of the coil are in the range of 0.5-2 mJ/m. In case of MgB_2 losses are in the range 2-6 mJ/m and are rather uniformly distributed since they only depend on the magnitude of the field. The local temperature increment in one cycle in adiabatic condition (no longitudinal or transversal heat diffusion is considered) corresponding to the maximum local value of losses is also reported in Table 9.3. This temperature increment is quite moderate for MgB_2 (0.1 K) whereas it is very high for YBCO (10.3 K). This requires a very careful design of the cooling connections of the terminal parts of the coil. In order to obtain stable operation of the SMES all the heat produced in the coil must be promptly removed, otherwise the rise of temperature may become non tolerable within a few cycles. If continuous operation (complete charge/discharge cycling) is required the whole amount of heat produced must be removed within 10 s. This is about 0.78 kJ for MgB_2 and 1.51 kJ for the YBCO at 3 T, which corresponds to an average power loss of 78 W and 151 W at 16 K. This requires an input power in of 13.9 kW and 26.9 kW respectively, for the cooling system in order to be removed (P_{input} = COP P_{loss}; an actual COP of 178 is assumed which corresponds to 10% of the ideal Carnot efficiency). In case of YBCO at 8T the total loss per cycle is about 4 kJ, which is much higher than the corresponding value at 3 T. The average power loss at 16 K and the input power of the cooling system are 395 W and 70 kW respectively. The average power loss discussed so far refers to AC losses only. Additional losses at 16 K occur due to eddy currents in metallic parts and heat invasion due to radiation and current leads. The cooling power of the SMES for the various cases is resumed in Table 9.3. It is to be considered that loss occurs in the converter during the charge and discharge of the SMES. As a double AC-DC and DC-DC conversion is carried out an overall efficiency of 98 % (corresponding to 99% each) can be assumed. The round trip efficiency of the SMES can be defined as the ratio between energy output energy and the energy input in one cycle. If a symmetric discharge/charge cycle at full power is considered the round trip efficiency is given by

(9.1) $$\eta = \frac{P\,\Delta t_{\text{discharge}}}{P\,\Delta t_{\text{discharge}} + \Delta P_{\text{conv}}\,\Delta t_{\text{charge}} + \Delta P_{\text{conv}}\,\Delta t_{\text{discharge}} + P_{\text{cooling}}\,(\Delta t_{\text{discharge}} + \Delta t_{\text{charge}})}$$

where P is the power effectively delivered to the power network. Converter losses, cooling power and efficiency values for the considered SMES systems are listed in Table 9.4. Note that the theoretical limit of the round trip efficiency, which would occur if no cooling power were required, is 96 % due to the loss of the converters. It can be seen that, due to the greater cooling power, the efficiency of the high-field YBCO SMES is much lower. It is worth to point out that the average power loss and the input power of the cooling system decreases if the charge/discharge cycling is not continuous. In Figure 9.1 the input power of the cooling system is plotted as a function of the number per cycle per hours for the three considered SMES. It is clear that, even though continuous operation is possible, limitation on the maximum allowable number of cycles allows higher efficiency. Indeed, for non-continuous cycling is considered losses occurs in the DC-DC converter during the idling phase (due to the free-wheeling of the SMES current) which should be included in the calculation of the efficiency [1.2].

Table 9.3. AC losses of the 1 MW / 5s SMES System during one discharge – charge cycle

	MgB_2 - 3 T	YBCO - 3 T	YBCO - 8 T
Max loss per unit length, mJ/m	6.0	434.5	551.6
Total energy loss of the coil, kJ	0.78	1.51	3.95
Average power loss, W	78	151	395
Heat capacity per unit length of conductor at 16 K, mJ/m.K	56	42	42
Maximum local temperature increment in adiabatic condition, K	0.1	10.3	13.1

Table 9.4. Round trip efficiency of the 1 MW - 5 s SMES System during one discharge/charge cycle

	MgB_2 - 3 T	YBCO - 3 T	YBCO - 8 T
Power delivered to the power network during discharge	1 MW	1 MW	1 MW
Power loss of the converters during discharge	20 kW	20 kW	20 kW
Power loss of the converters during charge	20 kW	20 kW	20 kW
Input power of the cooling system	13.9 kW	26.9 kW	70.3 kW
Round trip efficiency	93.6 %	91.4 %	84.7 %

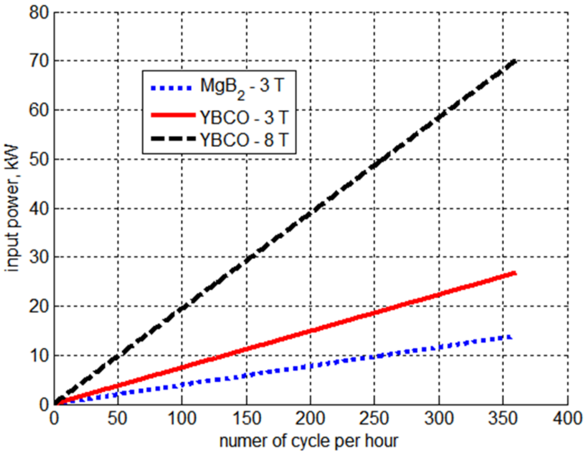

Figure 9.1 Input power of the cooling system for removal of AC losses versus number of complete charge/discharge cycles per hour. The maximum number of cycles per hour is 360 (10 s cycle)

9.4. ANALYSIS OF TRANSIENT BEHAVIOR OF THE COIL

Transient behavior of the coil with the power electronic interface is important, since exciting one of the resonance frequencies of the coil by switching of the PCS can cause over voltage on the coil so the insulation and in turns the coil will fail.

Calculating electrical lumped parameter model of the coil is discussed in section 5.4 and section 5.5. When the electrical lumped parameter of the coil is obtained, the next task is to determine the frequency response of the coil in order to assess the coil resonance frequencies.

The SMES coil of the MgB_2 is considered here. Here it is considered that the 2660 turns of the coil winding contains 532 layers. Each layer has 5 turns along the thickness of the coil. Each cable has 125 μm of electrical insulation and the coil in the insulated by 1.2 mm outside warped. Here, the extra insulation is not considered for the coil. For calculating the transient response of the coil each layer is considered as a single pancake. In the other word the coil made by 532 single pancakes where each pancake has 5 turns is considered. Based on the discussion in sections 5.4 and 5.5 the lumped parameter of the coil for 266 double pancakes is calculated and then for reducing the simulation time and complexity of the simulation the parameters are lumped to 14 double pancakes. The calculated parameters of the coil are reported in Table 9.5 and Table 9.6. The impedance of the coil versus the frequency without considering the AC loss resistance is depicted in Figure 9.2.

Table 9.5. Parameter of studied coil

	Series capacitance	Shunt capacitance
Double pancake	4.78 nF	1.38 nF
First and last double pancake	3.52 nF	3.11 nF
Entire coil	17.91 pF	371.16 nF

Table 9.6. Lumped coil inductance

$$L_{\text{coil}} = \begin{bmatrix}
0.0362 & 0.0167 & 0.0069 & 0.0035 & 0.0019 & 0.0012 & 0.0007 & 0.0005 & 0.0003 & 0.0003 & 0.0002 & 0.0001 & 0.0001 & 0.0001 \\
0.0167 & 0.0362 & 0.0167 & 0.0069 & 0.0035 & 0.0019 & 0.0012 & 0.0007 & 0.0005 & 0.0003 & 0.0003 & 0.0002 & 0.0001 & 0.0001 \\
0.0069 & 0.0167 & 0.0362 & 0.0167 & 0.0069 & 0.0035 & 0.0019 & 0.0012 & 0.0007 & 0.0005 & 0.0003 & 0.0003 & 0.0002 & 0.0001 \\
0.0035 & 0.0069 & 0.0167 & 0.0362 & 0.0167 & 0.0069 & 0.0035 & 0.0019 & 0.0012 & 0.0007 & 0.0005 & 0.0003 & 0.0003 & 0.0002 \\
0.0019 & 0.0035 & 0.0069 & 0.0167 & 0.0362 & 0.0167 & 0.0069 & 0.0035 & 0.0019 & 0.0012 & 0.0007 & 0.0005 & 0.0003 & 0.0003 \\
0.0012 & 0.0019 & 0.0035 & 0.0069 & 0.0167 & 0.0362 & 0.0167 & 0.0069 & 0.0035 & 0.0019 & 0.0012 & 0.0007 & 0.0005 & 0.0003 \\
0.0007 & 0.0012 & 0.0019 & 0.0035 & 0.0069 & 0.0167 & 0.0362 & 0.0167 & 0.0069 & 0.0035 & 0.0019 & 0.0012 & 0.0007 & 0.0005 \\
0.0005 & 0.0007 & 0.0012 & 0.0019 & 0.0035 & 0.0069 & 0.0167 & 0.0362 & 0.0167 & 0.0069 & 0.0035 & 0.0019 & 0.0012 & 0.0007 \\
0.0003 & 0.0005 & 0.0007 & 0.0012 & 0.0019 & 0.0035 & 0.0069 & 0.0167 & 0.0362 & 0.0167 & 0.0069 & 0.0035 & 0.0019 & 0.0012 \\
0.0003 & 0.0003 & 0.0005 & 0.0007 & 0.0012 & 0.0019 & 0.0035 & 0.0069 & 0.0167 & 0.0362 & 0.0167 & 0.0069 & 0.0035 & 0.0019 \\
0.0002 & 0.0003 & 0.0003 & 0.0005 & 0.0007 & 0.0012 & 0.0019 & 0.0035 & 0.0069 & 0.0167 & 0.0362 & 0.0167 & 0.0069 & 0.0035 \\
0.0001 & 0.0002 & 0.0003 & 0.0003 & 0.0005 & 0.0007 & 0.0012 & 0.0019 & 0.0035 & 0.0069 & 0.0167 & 0.0362 & 0.0167 & 0.0069 \\
0.0001 & 0.0001 & 0.0002 & 0.0003 & 0.0003 & 0.0005 & 0.0007 & 0.0012 & 0.0019 & 0.0035 & 0.0069 & 0.0167 & 0.0362 & 0.0167 \\
0.0001 & 0.0001 & 0.0001 & 0.0002 & 0.0003 & 0.0003 & 0.0005 & 0.0007 & 0.0012 & 0.0019 & 0.0035 & 0.0069 & 0.0167 & 0.0362
\end{bmatrix}$$

As can be seen from Figure 9.2, the coil resonances occur between the frequency-ranges of 400-12000 Hz. If a coil is excited at one of these resonant frequencies, we expect over-voltages.

9.5. POWER CONDITIONING SYSTEM CONTROL ALGORITHMS AND APPLICATIONS

The power conditioning system (PCS) for the interconnection of the superconducting coil with the power grid is shown in Figure 9.3. It consists of a two quadrant chopper, a voltage source inverter and a transformer. Both the chopper and the inverter are based on IGBT. It is worth to point out that IGBTs modules exist today with a voltage rating of several kV and current rating up to 4.8 kA which can be used for high power converters that previously could be implemented by GTOs only [9.8]. An LC filter is also added to reduce the harmonic content at the AC side. A capacitor is used as intermediate (low capacity) storage element for leveling the voltage of the DC bus. The state of charge of the capacitor is regulated by the SMES which continuously injects or extracts current from the DC bus by means of the PWM controlled chopper. With this architecture of the PCS the SMES is able to perform full compensation of the voltage sag and the leveling of impulsive load. Harmonic compensation and power factor correction can also be performed with the same system, though for this operation the use of the SMES is not required.

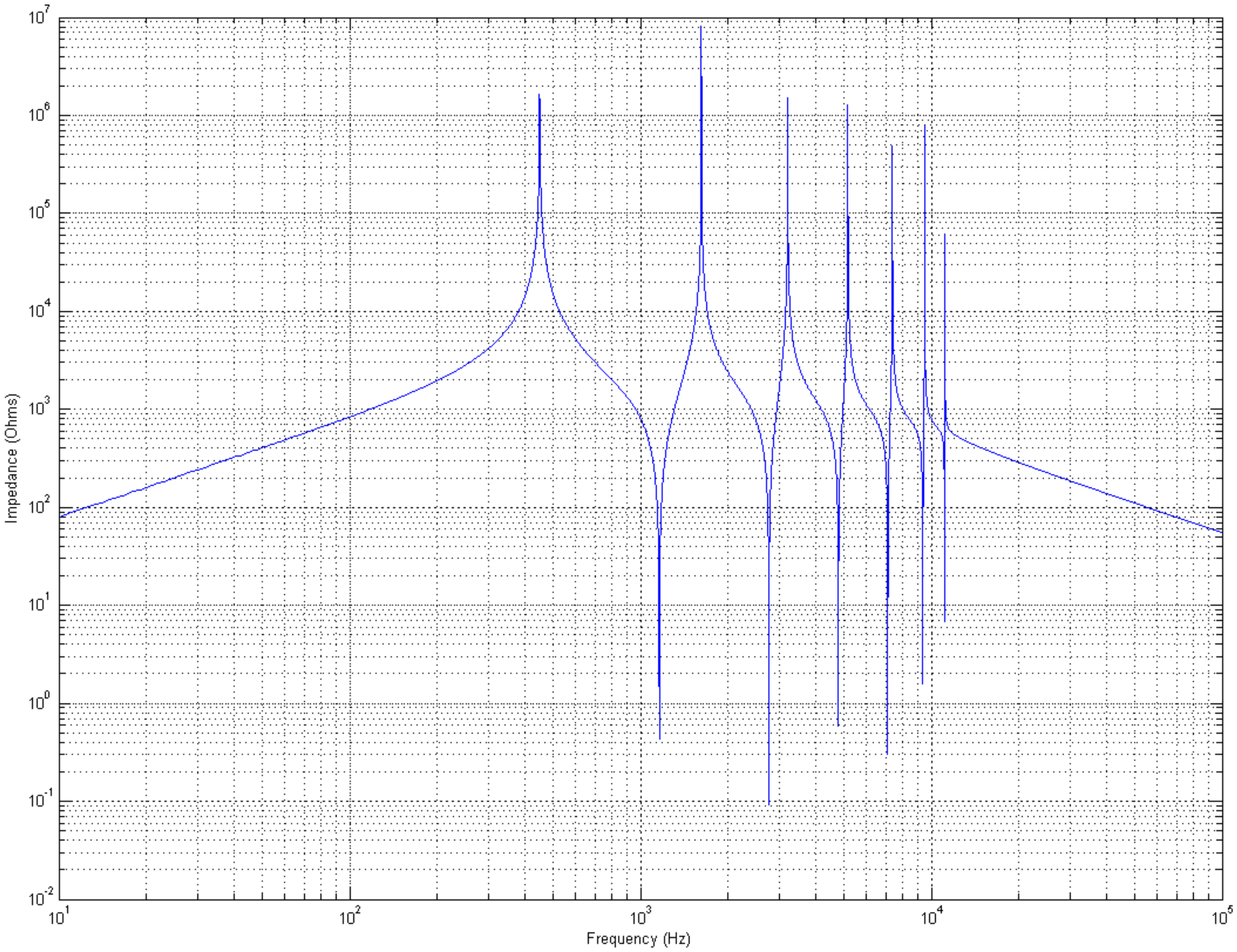

Figure 9.2 Frequency response of the coil

In this section the performance of the SMES during compensation of voltage sags, leveling of impulsive load and harmonic compensation / power factor correction, is numerically investigated. Two control algorithms are introduced for this purpose. A current control algorithm, developed in [9.9], is used to perform leveling of impulsive load. The same algorithm, with modified parameters is also used in normal network condition for harmonic compensation and power factor correction. A voltage control algorithm is used instead for voltage sag compensation. If a voltage sag is detected the control method is switched from the current control mode to the voltage control mode. The voltage sag detection method proposed in [9.10] is implemented for this purpose. The *dq* transformation of the three phase quantities is carried in order to implement the control algorithms. The main scheme of the control system is shown in Figure 9.4, along with the scheme of the power system. The hierarchy of the functions implemented by the control algorithm is as follows

- In normal condition reactive power compensation and harmonic compensation are routinely carried out. The current control algorithm is used during this phase.

- Load leveling is carried out if an input signal is received from the user. The current control algorithm with modified parameters is used during this phase.
- Voltage compensation is carried out if a voltage sag is detected. The voltage control algorithm is used during this phase. The grid is disconnected during this phase by means of the switch SW.
- The recharge of the SMES to its maximum stored energy is carried out after voltage sag. The current control algorithm with modified parameters is used during this phase.

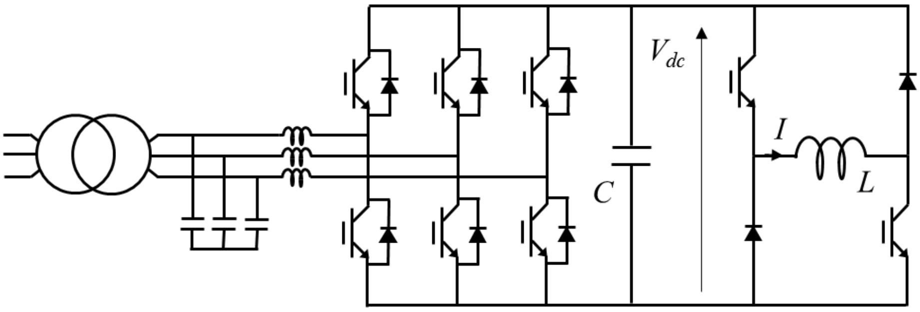

Figure 9.3 Power conditioning system

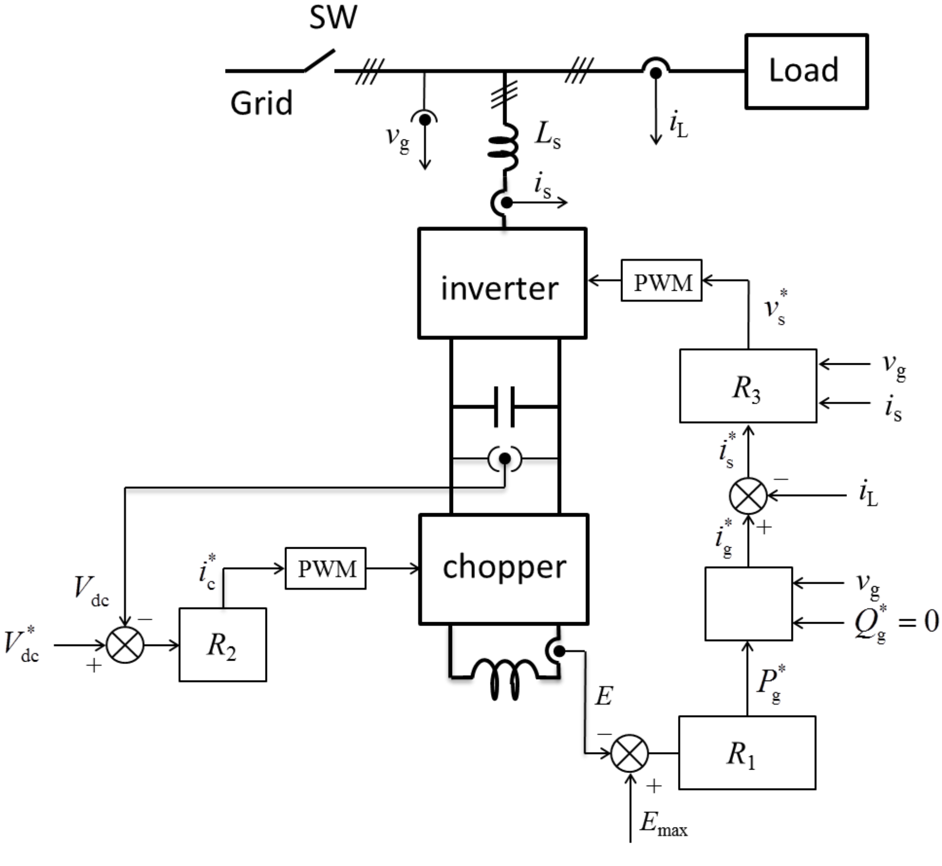

Figure 9.4 Schematic of the control and the power system

9.5.1. Control Algorithms

9.5.1.1. Current Control Algorithm

Three control loops can be distinguished within the current control algorithm [9.9]:

- the control loop of the energy E stored by the superconducting coil,
- the control loop of the voltage V_{dc} of the DC bus
- and the control loop of the output current i_{s} of the inverter

These three loops are illustrated in Figure 9.5.

The current i_{L} of the load and the voltage v_{g} of the grid are continuously measured. The real power P_{L} of the load is calculated accordingly. The current i_s of the inverter is continuously measured as well. The reference real power P_{g}^* that the grid is to supply is calculated from the control loop of the energy E of the SC coil. In practice P_{g}^* is obtained from the difference between the maximum value E_{max} and the actual energy E by means of the PI regulator R_1. In this way the more the coil energy is close to its maximum value the more the grid can be exempted to deliver power to the load. From Figure 9.5 (a) it can be deduced that a low-pass transfer function is established between the power P_{g}^* of the grid and the power P_{L} of load, which means that the SMES systems smoothens the power fluctuation of the load. The voltage of the DC bus is controlled by means of the chopper. The reference value of the current i_c^* of the chopper is obtained from the difference between the reference value V_{dc}^* and the current value V_{dc} of the voltage of the DC bus by means of the PI regulator R_2, as it is shown in Figure 9.5 (b). From the value of i_{c}^* the PWM control signals of the chopper are derived. Finally, the inverter is controlled in order to add to i_{L} a reference correcting current i_{s}^* so that a reference sinusoidal current i_g^* in phase with the voltage v_{g} is set on the grid, that is $i_{\mathrm{s}}^* = i_{\mathrm{g}}^* - i_L$. The current i_{g}^* is calculated based on the reference real power P_{g}^* that the grid is to supply and by adding the condition $Q_{\mathrm{g}}^* = 0$ (unit power factor is required). The reference value of the output voltage of the inverter is obtained from the discrete approximation of the voltage equation $v_{\mathrm{s}}^* = L_{\mathrm{s}}\, di_{\mathrm{s}}/dt + v_{\mathrm{g}}$ (see Figure 9.5 (c)). More specifically the value of term $L_{\mathrm{s}}\, di_{\mathrm{s}}/dt$ is deduced at each time interval from the difference between the reference value i_s^* and the actual value i_{s} by means of the proportional regulator R_3, and then the grid voltage v_{g} is added. From the value of v_{s}^* the PWM control signals of the inverter are derived. The parameters of the three control loops of the current control algorithms as well as the PWM frequency used for the chopper and the inverter are listed in Table 9.7. The PWM frequency of the chopper is chosen based on the frequency response of the coil (see Figure 9.2). The selected frequency and the multiples of this frequency is not excited the resonance frequencies of the coil.

Table 9.7. Parameters of the current and the voltage control algorithm

	Normal operation condition		Voltage sag compensation	
	Power factor correction	Load leveling	Discharge	Charge
k_{p1}	50	50	–	35
k_{i1}	1	1	–	9
k_{p2}	50	50	50	50
k_{i2}	5	5	5	5
k_{p3}	1.474	3	–	5
PWM frequency of chopper	0.75 kHz			
PWM frequency of inverter	2.00 kHz			

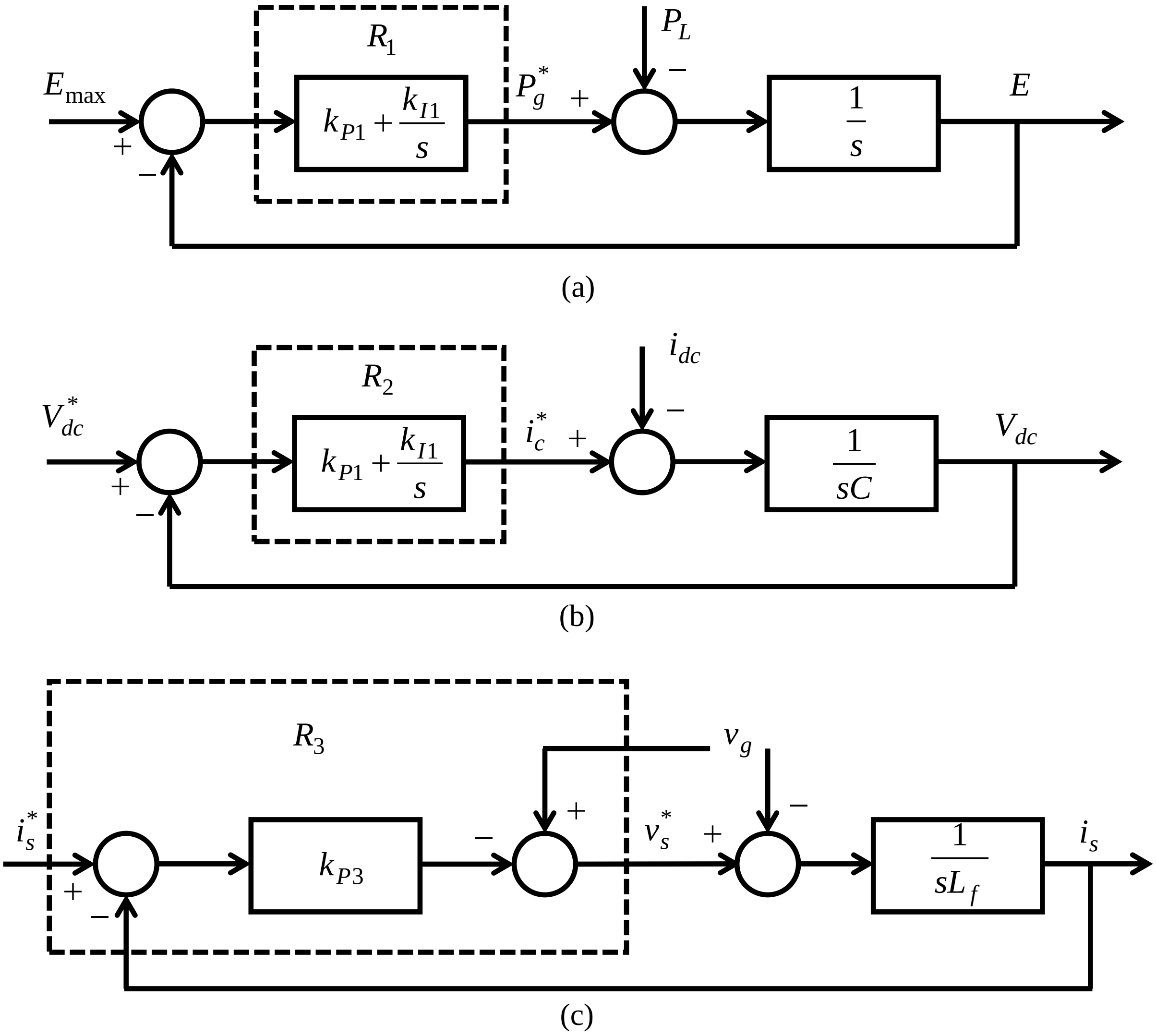

Figure 9.5 Current control algorithm (a) Control loop of the energy E stored by the superconducting coil (b) Control loop of the voltage V_{dc} of the DC bus (c) Control loop of the output current of the inverter

9.5.1.2. Voltage Control Algorithm

The inverter is used in order to provide a sinusoidal voltage with nominal frequency and amplitude to the passive load. A PWM control is carried out in this phase. The impedance of the load determines the power which is absorbed during this phase. The control of the chopper is the same as for the current control algorithm so as to maintain the voltage of the DC bus constant. The parameters of the voltage control algorithms are also listed in Table 9.7.

9.5.1.2.1. Voltage sag detection algorithm

As a definition voltage sag is brief reductions in voltage magnitude lasting from one cycle to a second [5.2]. The voltage sag is a common undesirable power quality phenomena and cause malfunction of sensitive load and may even damage them. To protect sensitive load and suppress the effect of this phenomenon the time response of voltage sag detection is crucial [9.10].

The simplest way to detect voltage sag is monitoring the rms value of the voltage and using a threshold. But monitoring the rms value of the load voltage will not lead to the fast enough response. The other possible ways to understanding voltage dip is monitoring voltage amplitude and/or monitoring the voltage change rate. The monitoring voltage amplitude has a drawback that is needed more time is some cases, especially when the voltage sag occurred in between the two peaks of the sinusoidal waveform, and monitoring the voltage change rate near the peak value of the voltage do not have good performance to detect the voltage sag. The other way of detecting voltage sag is a using PLL and *dq* transformation. Using the PLL and *dq* transform is a common way to fast detecting voltage sag and in more cases it takes about 1 to 2 ms to detecting voltage sag. The other way of detecting voltage sag is using *αβ* transform (Clarck transformation) without using a PLL. In [9.10] it is reported that, in the worst case voltage sag can be detected in 0.68 ms. In this algorithm the *αβ* component of the single phase voltage is calculated as fallows [9.10]:

$$\begin{aligned} v_{\mathrm{grid},\alpha}(t) &= v_{\mathrm{grid}}(t)\cdot\sin(\omega t) = 0.5\cdot V_{\mathrm{m}}\left[\cos(\theta)-\cos(2\omega t+\theta)\right] \\ v_{\mathrm{grid},\beta}(t) &= v_{\mathrm{grid}}(t)\cdot\cos(\omega t) = 0.5\cdot V_{\mathrm{m}}\left[\sin(2\omega t+\theta)+\sin(\theta)\right] \\ v_{\mathrm{grid}}(t) &= V_{\mathrm{m}}\cdot\sin(\omega t+\theta) \end{aligned} \tag{9.2}$$

where V_{m} is the voltage peak value, $\omega = 2\pi f$, f is the system frequency, and θ is the phase angle of the voltage. By calculating the derivation of the *αβ* components the DC value can be eliminated and the derivation of *αβ* components can be written as follows:

$$v'_{\mathrm{grid},\alpha}(t) = \omega V_{\mathrm{m}} \sin(2\omega t + \theta) \tag{9.3}$$
$$v'_{\mathrm{grid},\beta}(t) = \omega V_{\mathrm{m}} \cos(2\omega t + \theta)$$

The peak value of the grid voltage can be detected instantly as follows:

$$\left(v'_{\mathrm{grid},\alpha}(t)\right)^2 + \left(v'_{\mathrm{grid},\beta}(t)\right)^2 = (\omega V_{\mathrm{m}})^2 \cdot \underbrace{\left((\sin(2\omega t + \theta))^2 + (\cos(2\omega t + \theta))^2\right)}_{=1} \tag{9.4}$$

$$V_{\mathrm{m}} = \sqrt{\left(v'_{\mathrm{grid},\alpha}(t)\right)^2 + \left(v'_{\mathrm{grid},\beta}(t)\right)^2} \Big/ \omega \tag{9.5}$$

This method has a drawback in non-sinusoidal voltage condition and it needs harmonic filter delay to drive the fundamental voltage amplitude. But in this case because of the harmonic compensating function of the proposed algorithm and assuming the sinusoidal network voltage the drawback does not affect the sag detection performance.

Figure 9.6 shows the structure of the proposed method to detecting voltage sag. In the proposed algorithm by using equations (9.2)-(9.5) instantaneous value of the maximum voltage is calculated. The minimum value of the three phases is calculated and compared with the reference value. Using T_{step} = 50 μs time step simulation and assuming the sinusoidal voltage, voltage sag is detected in 0.3 ms after fault.

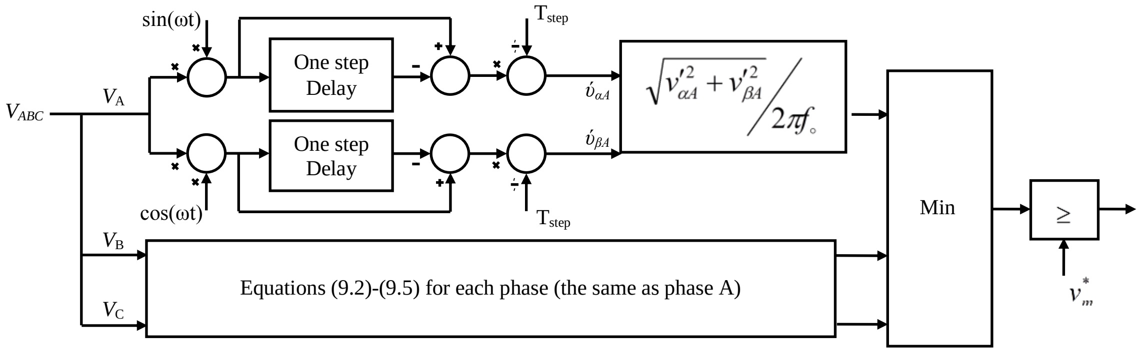

Figure 9.6 Voltage sag detection algorithm, in this figure the details just shown to one of the phases and for other phases the same algorithm is used

9.5.1.2.2. Reference voltage calculation

The output voltage of the inverter should be in the phase with the network and has the same amplitude. In the proposed control algorithm by using PLL, network voltage phase is calculated and updated in each cycle of the line frequency. When the control signal was detected the updating process ignored and the stored value is used as a reference value. With using mathematical equation a sinusoidal waveform with the stored voltage phase and rms value are produced as a reference voltage waveform. Figure 9.7 illustrates the reference voltage calculation part. In the proposed algorithm after clearance of the voltage sag new voltage phase will follow in order to prevent the short term voltage decay during the transferring process to the network.

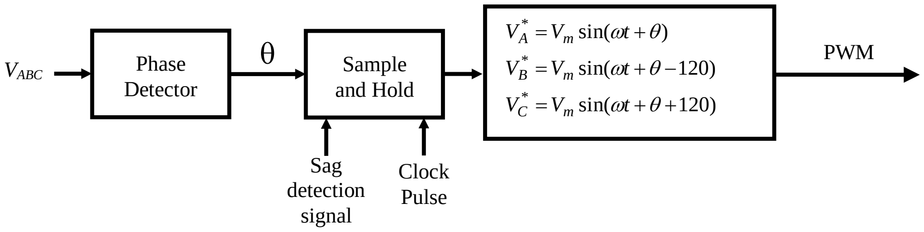

Figure 9.7 Reference voltage calculation for voltage control part of the algorithm

9.5.2. Design of the power electronic interface of the SMES system

As discussed in chapter 3 two different interfaces for the PCS is available; the most common topology is the VSI, on the other hand, CSI has simple configuration, good output waveform and high fault-tolerant capability [9.11]. Since the SMES is the current source it is attracted that be implemented by current source inverter. By using a current source inverter one can be avoided the DC-DC chopper and can deliver more reactive power to the network. However, on the other hand CSI needs a significant output capacitor filter (0.3 to 0.6 pu) for commutation process.

As mentioned before for having full reactive power control, independently to the coil current and the other features which is summarized in Table 3.1 VSI inverter connected to the two quadrants chopper in DC side is chosen.

The Asymmetric Integrated Gate Commutated Thyristor (IGCT) 5SHY 55L4500 [9.12] with Fast Recovery Diode 5SDF 28L4520 [9.13] of the ABB products is considered for constructing the DC-DC chopper and the VSI interface with proper snubber parameters which are reported in [9.12] and [**9.13**]. The operating frequency of the chopper and the VSI is reported in Table 9.7.

The on state resistance of the IGCT is 0.28 mΩ per device [9.12] and the on state resistance of the diode is 0.47 mΩ [9.13], and since the withstand voltage of the devices are more than 1 kV and the current carrying capacity of them is more than the maximum current of the coil [9.12] and [9.13], so parallel or series connected device is not required. Single phase DC-DC chopper is assumed in this study and a regular 2 level VSI with output filter and coupling transformer with X_{cc} = 0.13 pu is considered. Low on state resistance and low switching loss of the IGCT, comparing to the IGBT modules, improves the round trip efficiency of the SMES system.

9.5.3. Applications

9.5.3.1. Compensation of voltage sag

The operation of SMES during voltage sag compensation is shown in Figure 9.8. The considered case consists of a manufacturing plant with 1 MW power which is extremely sensitive to voltage quality. The allowed deviation of the voltage is from −10% to + 5%. A reduction of the voltage below 70% of the nominal value can only be tolerated for half a cycle (10 ms). Longer lasting voltage sag causes interruption of the process. A voltage sag lasting 5 s due to a fault on the grid side is considered. As it is shown in the figure the SMES is able to completely cancel the sag (the residual voltage of the never falls below 70 % of the nominal voltage) and to provide full power to the load during the 5 s grid interruption. At the reclosing of the grid the SMES recharges at full power and reaches the nominal value of stored energy after 5 s.

9.5.3.2. Load leveling of impulsive or rapidly fluctuating loads

The operation of the SMES during load leveling is shown in Figure 9.9. A linear load which absorbs 1 MW power during 20 % of the working cycle (1 s in total) is considered. An average power of about 200 kW with ±110 kW fluctuation is provided by the grid during the whole cycle, which greatly simplifies the supply apparatus. The extra-power required by the load during the active phase is supplied by the SMES which recharges at about 200 kW during the rest of the cycle. Note that SMES is the enabling element for this application, since the high number of charge/discharge cycles required for continuous operation cannot be dealt with by means of other storage technologies.

9.5.3.3. Power factor correction

The operation of the SMES system during power factor correction is shown in Figure 9.10. A linear RL load with 1 MW real power and 0.84 lag power factor is considered. As it can be appreciated from the Figure 9.10 the SMES is able to provide the reactive power required by the load, thus raising to 1 the power factor on the grid side. It is worth to note that, since no significant power is supplied by the SMES, the DC side of the system (SC coil + chopper) is not strictly needed during this operation.

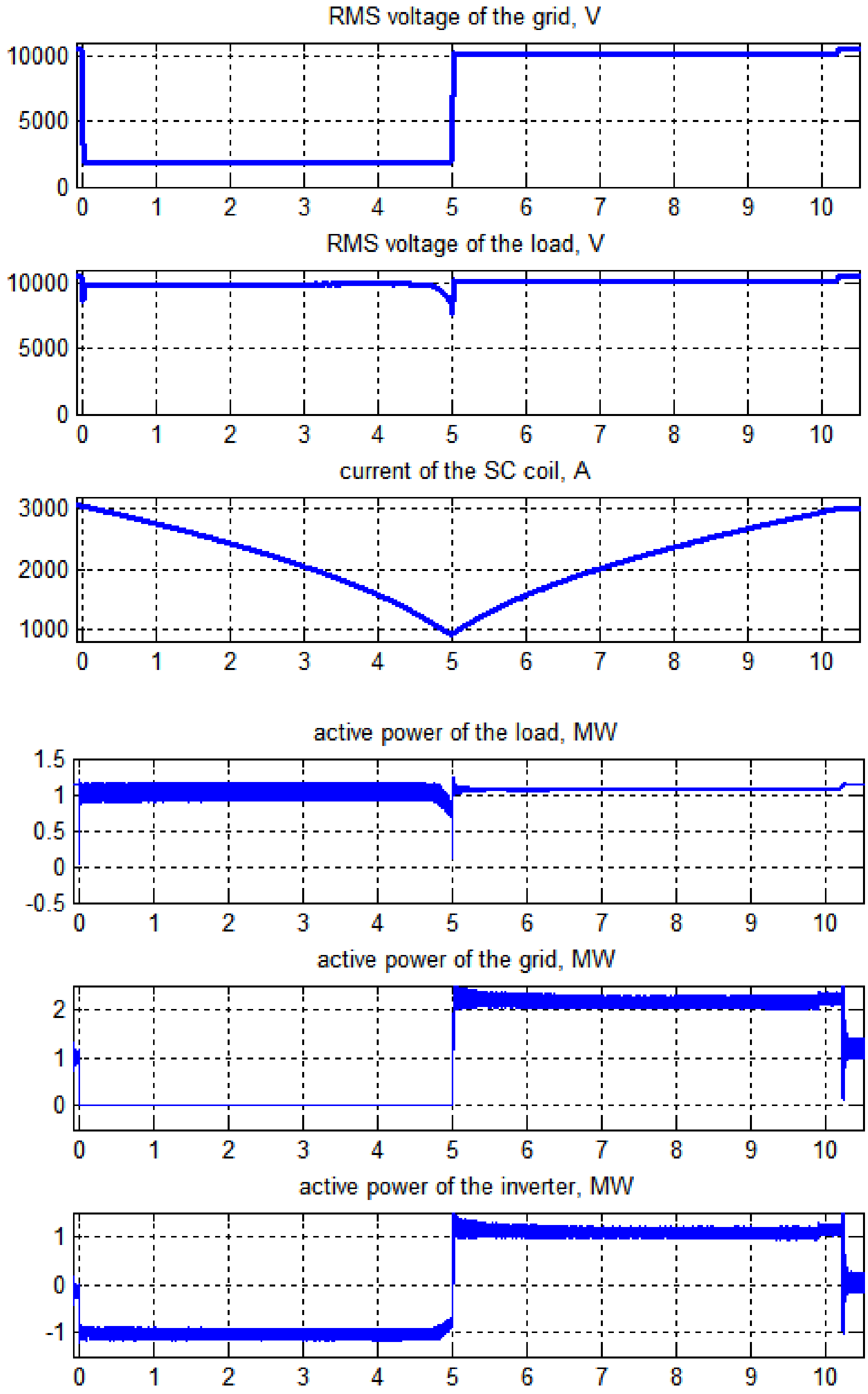

Figure 9.8 SMES system operation during voltage sag compensation

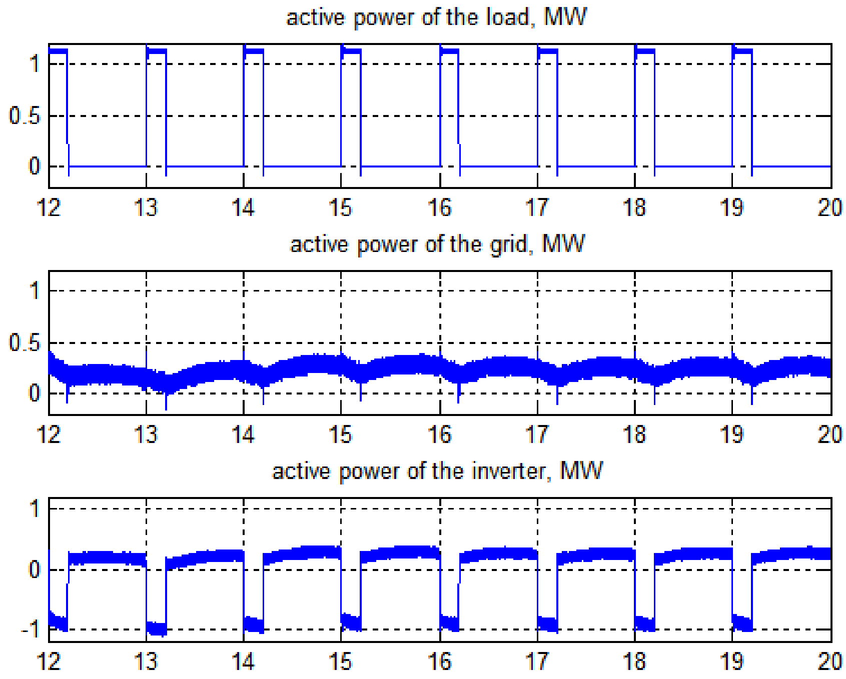

Figure 9.9 SMES system operation during load leveling

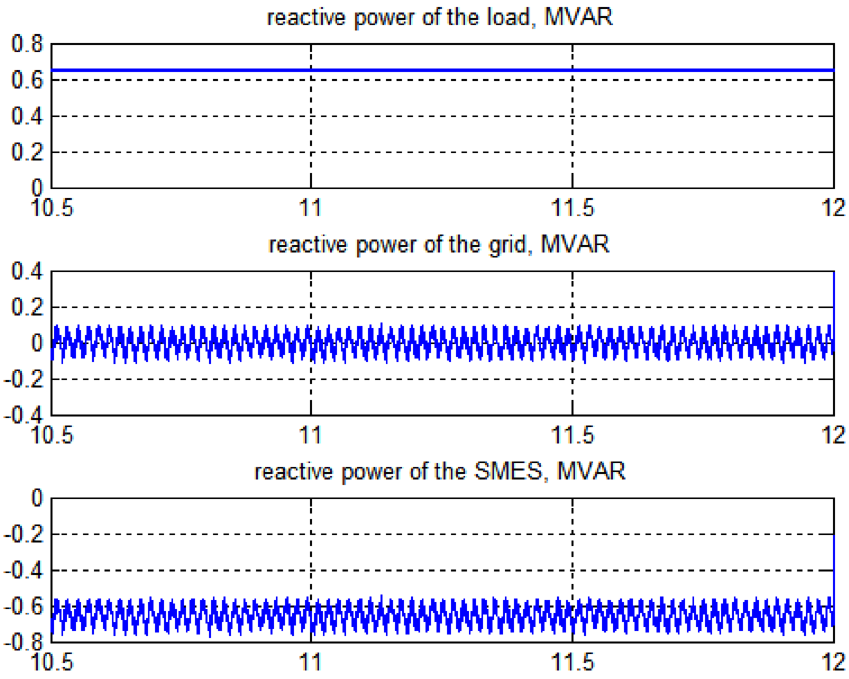

Figure 9.10 SMES system operation during power factor correction

9.6. REFERENCES

[9.1] G. Grasso, “MgB_2 ten years after”, Workshop on Transporting Tens of Gigawatts of Green Power to the Market, Postdam-Germany, May 13th, 2011, on line: http://goo.gl/G9jt3r

[9.2] N. Hayakawa, H. Kojima, M. Hanai, and H. Okubo, “Recent Progress in Electrical Insulation Techniques for HTS Power Apparatus,” Physics Procedia, Vol. 36, 2012, pages 1305-1308, DOI:10.1016/j.phpro.2012.06.295

[9.3] S.W. Schwenterly, E.F. Pleva, “HTS Transformer Development,” DOE Peer Review, Washington-DC, August 7, 2007, online: http://goo.gl/AWUTAm

[9.4] N. Amaro, J. Šouc, M. Vojenčiak, J. M. Pina, J. Martins, J. M. Ceballos, and F. Gömöry, “AC Losses and Material Degradation Effects in a Superconducting Tape for SMES Applications,” in Technological Innovation for Collective Awareness Systems, Vol. 423 of the series IFIP Advances in Information and Communication Technology, pages: 417-424, DOI:10.1007/978-3-642-54734-8_46

[9.5] A. Malagoli, C. Bernini, V. Braccini, C. Fanciulli, G. Romano, and M. Vignolo, “Fabrication and superconducting properties of multifilamentary MgB_2 conductors for AC purposes: twisted tapes and wires with very thin filaments”, Superconductor Science and Technology, Vol. 22, No. 10, 2009, 105017 (6pp), http://iopscience.iop.org/article/10.1088/0953-2048/22/10/105017

[9.6] I. Kesgin, G. Majkic, V. Selvamanickam, “Fully filamentized HTS coated conductor via striation and selective electroplating,” Physica C: Superconductivity, Vol. 486, March 2013, pages: 43–50, DOI:10.1016/j.physc.2013.01.016

[9.7] S. Terzieva, M. Vojenčiak, F. Grilli, R. Nast, J. Šouc, W. Goldacker, A. Jung, A. Kudymow, and A. Kling, “Investigation of the effect of striated strands on the AC losses of 2G Roebel cables,” Superconductor Science and Technology, Vol. 24, No. 4, January 2011, 045001 (5pp), http://iopscience.iop.org/article/10.1088/0953-2048/24/4/045001

[9.8] T. Fujihira, H. Kaneda, and S. Kuneta, “Fuji electric’s semiconductors: current status and future outlook,” Fuji Electric Review, Vol. 51, No. 2, 2006, Online: http://www.fujielectric.com/company/tech/pdf/r52-2/01.pdf

[9.9] D. Casadei, G. Grandi, U. Reggiani, G. Serra, “Analysis of a power conditioning system for superconducting magnetic energy storage (SMES)”, IEEE International Symposium on Industrial Electronics (Proceedings ISIE ’98), Vol. 2, 7-10 July 1998, pages: 546-551, DOI: 10.1109/ISIE.1998.711612

[9.10] A. K. Sadigh, K. M. Smedley “Fast voltage sag detection method for single-/three-phase application,” Twenty-Eighth Annual IEEE Applied Power Electronics Conference and Exposition (APEC), 2013, 17-21 March 2013, Long Beach, CA, USA, pages: 881-888, DOI: 10.1109/APEC.2013.6520315

[9.11] Z. Wang, L. Jiang, Z. Zou, and M. Cheng “Operation of SMES for the Current Source Inverter Fed Distributed Power System under Islanding Mode,” IEEE Transactions on Applied Superconductivity, Vol. 23, No. 3, JUNE 2013, DOI: 10.1109/TASC.2012.2232703

[9.12] Asymmetric Integrated Gate Commutated Thyristor “5SHY 55L4500”, ABB public documents and data sheet, online: https://goo.gl/D1yrzW or

[9.13] Fast Recovery Diode “5SDF 28L4520”, ABB public documents and data sheet, online: https://goo.gl/zbbDch or https://library.e.abb.com/public/bab0610f408b183d83257b280033a656/5SDF%2028L4520_5SYA1185-02Feb%2013.pdf

10. SUPERCONDUCTING DISTRIBUTION SYSTEM (WIND PARK COLLECTOR SYSTEM)

The connection system of offshore wind parks with the onshore power grid can have a crucial impact on the overall energy yield. The most common solution used for the connection system is by means of a medium-voltage AC collector grid, which directs the energy of the turbines to the point of common coupling at the center of the park, followed by a high voltage AC transmission link to the shore. Though simple and very well established this approach has some disadvantages such as the high losses of the AC cables and the loss of the power-electronic converters needed to adapt the generator voltage with the grid voltage with regard to the amplitude and frequency. A possible alternative, which is receiving increasing attention, are medium-voltage DC (MVDC) collector grids instead of AC that are followed by a high-voltage DC (HVDC) transmission link and a subsequent onshore DC-AC conversion. Indeed, several architectures can be conceived for the connection system depending on the type of operation (AC or DC) and the voltage level of the collector grid and the transmission link, respectively. Multiple voltage levels can also be used within the collector grid in order to optimize performance and costs. The number of converters and related platforms that are required depends on the chosen architecture of the collector grid. The architecture also has a strong impact on the overall loss and on the cost of the connection system. However, in case of DC operation, losses of the cables are negligible if high temperature superconductor (HTS) cables are used. Moreover, a medium-voltage DC transmission link becomes feasible by means of a HTS cable due to its very high current capacity and high efficiency. The use of the medium voltage transmission eliminates the voltage conversion stage and thus further reduces both the loss and the capital cost of the connection system.

In this chapter possible AC and DC connection systems for offshore wind parks are investigated in detail and are compared both in terms of cost and losses. Both conventional (copper) cables and high temperature superconductor cables are considered in case of DC systems. The layout of the various connections systems and the architecture of the converters will discuss in detail. And the main characteristics of the DC HTS cables designed for application to the connection systems will discuss. The cost and loss calculation methods for the possible connection will carry out. And finally, the economical comparison will discuss in detail. Both the capital costs and the missed income resulting from the losses during the whole lifetime of the wind park are considered for this scope.

10.1. DESCRIPTION OF THE OFFSHORE WIND PARK AND CONNECTION SYSTEM

An offshore wind park consisting of 72 turbines with 5 MW peak power each is considered as a case study. The peak power capacity of the whole park is 360 MW. The turbines are arranged in 4 clusters of 18 turbines each [10.1]. The turbines of each cluster are arranged in three lines of six turbines each. The layout of the wind park and the connection system to the onshore AC grid are schematically shown in Figure 10.1. The connection system consists of three main parts: the cluster collector grid, the park collector grid and the park-to-shore link. The details are discussed in the following.

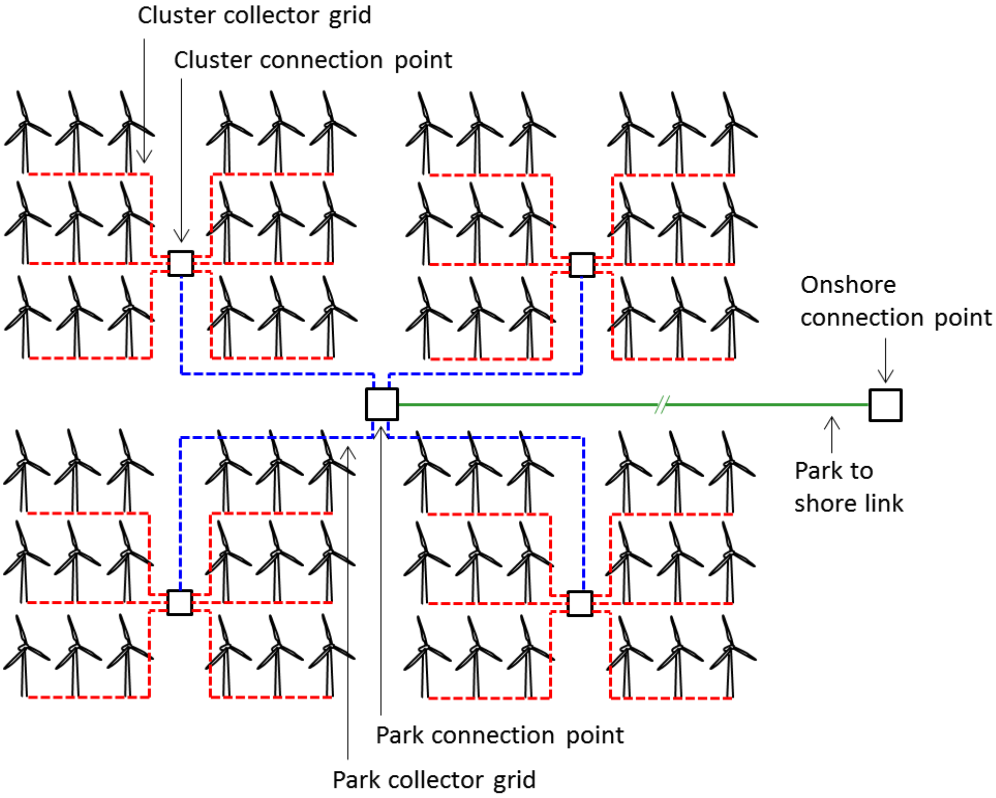

Figure 10.1 Schematic of the offshore wind park and connection system

10.1.1. Power output of the wind turbines

Each turbine is equipped with a 5 MW permanent-magnet synchronous generator (PMSG). The final rated voltage output of the turbine can be AC at 3.3 kV / 50 Hz or DC at ± 2.5 kV, depending on the architecture chosen for the connection system. In both cases, the AC output of the PMSG is first converted to ± 2.5 kV DC by means of a three-level neutral-point clamped (3L-NPC) converter which allows effective maximum-power point tracking (MPPT) of the wind turbine with variable speed operation. More details on the characteristics and the performance of the considered 5 MW 3L-NPC AC-DC converter can be found in [10.1]. A further DC-AC conversion is applied if an AC output is required for the turbine. This is realized with a second 3L-NPC inverter connected back-to-back to the machine-side converter. This is the approach exploited, for example, in the AREVA M5000 commercial system [10.2]. A lower overall efficiency of the wind turbine is obtained in case of AC output due to this additional DC-AC conversion step.

10.1.2. Productivity of the wind park

The productivity of the wind park is shown in Figure 10.2 in terms of number of hours in one year versus percentage of the available power generation [10.3] and [10.4]. The shown data are deduced from wind speed measurements performed on Fino 1 [10.5], a German research platform in the North Sea, which is located close to the wind farm Alpha Ventus. The yearly energy produced by the generators using the wind data results in 1630 GWh.

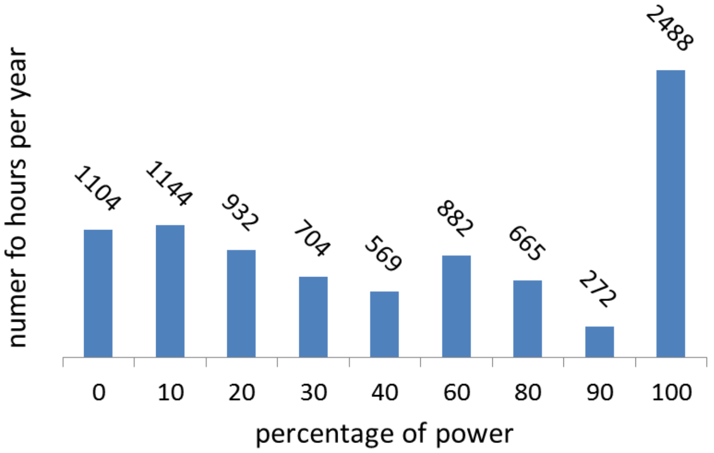

Figure 10.2 Productivity of the offshore wind park deduced from weather measurements at Fino 1 research platform [10.5]

10.1.3. Cluster collector

The cluster collector grid connects each single turbine within the cluster to the connection point located at the center of the cluster (see Figure 10.1). The conventional implementation of the cluster collector grid is 33 kV AC [10.6] and [10.7]. In this case, the output of the wind turbine is 3.3 kV

AC and an additional transformer is required to step up the voltage to the required level of 33 kV. A possible alternative is a DC collector grid that can be directly connected to the DC output of the machine-side power-electronic converter. Given the output voltage of 3.3 kV AC for the turbine drive train, a voltage level of ± 2.5 kV DC can be implemented for the DC collector grid [10.1]. The vertical and the horizontal distance between the wind turbines of the cluster is an important parameter. A large distance is desirable since it reduces the shadowing wake effect thus improving the productivity of each turbine. However, a longer cabling length is required which increases both the capital cost and the losses, especially for large parks. In the following we assume a compromise distance of 1 km both in the horizontal and the vertical [10.1].

10.1.4. Park collector

The park collector grid links the connection point of each cluster to the park connection point, located at the center of the park (see Figure 10.1). A length of 8 km is considered for each of the four connections. The park collector can be either AC or DC. The options that will be investigated in the following are AC at 33 kV and DC at ± 20 kV. It is worthwhile to point out that, if AC operation at 33 kV is considered, there is no difference between the cluster and the park collector. They are in fact merged in a unique grid made of multiple cables, which directly connect the turbines to the park connection point [10.7], and no platform is required at the center of each cluster. A 33 kV AC cable with 15 MW rating is considered in this case. This is used to link three turbines to the park connection point. In this case, 24 of these cables are required with an average length of 8 km.

10.1.5. Park–to-shore link

The park-to-shore link connects the park connection point to the onshore AC grid which operates at 220 kV. The length of the link is considered to be 50 km. The link can be operated either in AC or DC. The options that will be investigated in the following are AC at 220 kV and DC at ± 20 kV and ± 150 kV.

10.1.6. Power-Electronic Converters

The possible converter options (and related platforms) needed for connecting the cluster-collector, the park-collector and the park-to-shore link depend on the type (AC or DC) and the voltage level of each of them. If both the cluster and the park collectors operate in DC but at different voltages, then a DC-DC conversion is required at the cluster connection point. In this case the system is referred to as two-stage collector system. Also, a DC-DC conversion is needed at the park connection point to step up the DC voltage to the level of the park-to-shore link. These DC-DC conversions are realized with the modular arrangement (parallel connected at low-voltage side / series connected at high-voltage side) of multiple dual-active bridge (DAB) DC-DC converters, as it is schematically shown in Figure 10.3.

A DAB consists of two full-bridge converters connected via a medium-frequency transformer with each other that provides galvanic isolation [10.8]. The two full-bridge converters modulate a six-step voltage waveform with a frequency of 1 kHz. More details on the design, control and performance of the considered DAB converter system can be found in [10.1] and [10.9]-[10.12].

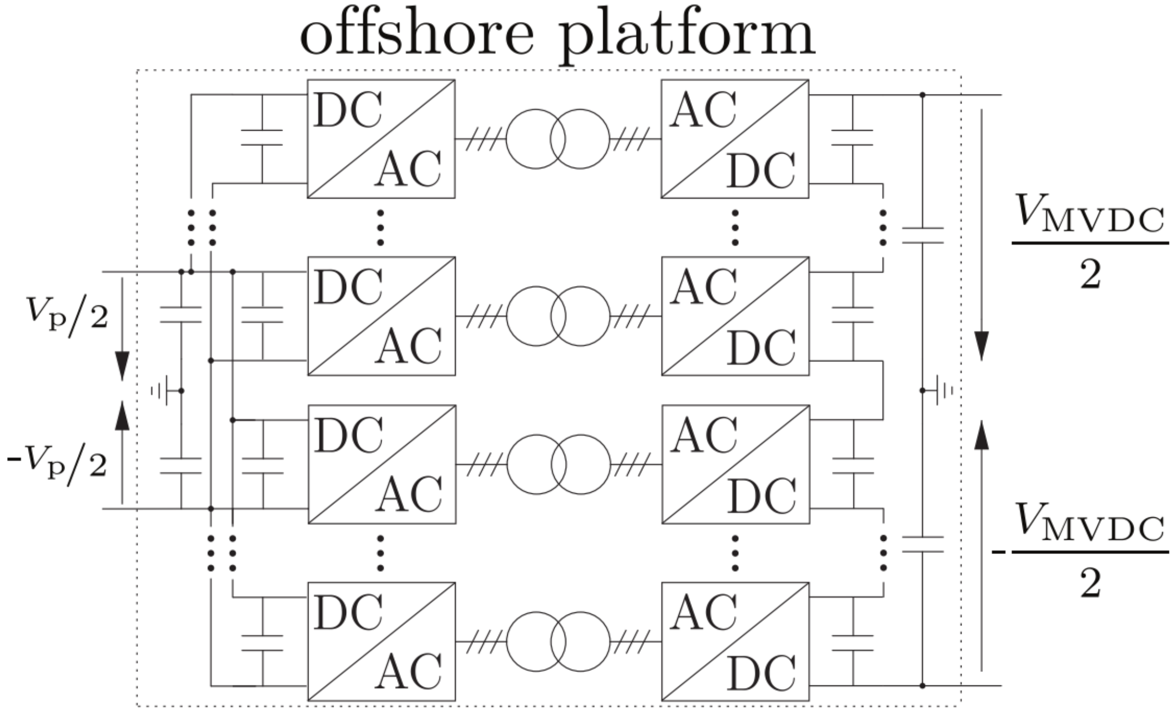

Figure 10.3 Block diagram of the DAB converter system for DC voltage conversion [10.1]

10.2. DC HTS CABLES

The schematic of a DC HTS power cable is shown in Figure 10.4. The cable's core is made of several layers of HTS tapes helically wound on a copper former. The former is used to provide manufacturability and mechanical support and also for stabilization and fault withstand purpose. Electric insulation is applied onto the HTS layers and operates at low temperature. The cooling is provided by the circulation of pressurized liquid Nitrogen (LN_2), with a temperature range of 65 K - 77 K, contained in the enveloping pipe made of corrugated stainless steel. A further and outermost pipe is added to create a vacuum space in between. This vacuum space, filled with multilayer low emissivity materials (MLI), has the purpose of reducing the heat invasion due to radiation. A polyethylene sheath with steel armor is finally added to provide chemical and mechanical protection. As for conventional cables, a conducting shied is added at the outermost part of the cable to equalize the electric field stress, reduce the EMI impact and provide a return path for the fault current. Based on present state of the art hybrid vacuum/MLI thermal-insulation technology, the heat load per unit surface λ at 77 K due to radiation from 300 K (ambient temperature) can be kept below 1.2 W/m^2 [6.18]. A further source of heat load for the HTS cable is the termination, i.e. the copper current-lead, which is used to connect the cold core of the cable to the power circuit at ambient temperature. Nowadays, terminations are optimized to minimize heat invasion, and the typical level of heat load *k* when the two ends are at 300 K and 77 K, respectively, is 50 W/kA [6.19]. Thanks to the DC operation no significant electromagnetic loss occurs in the core of the cable due to the transport current [10.13]. A detailed discussion on design methods, application and benefits of DC HTS cables can be found in [6.11].

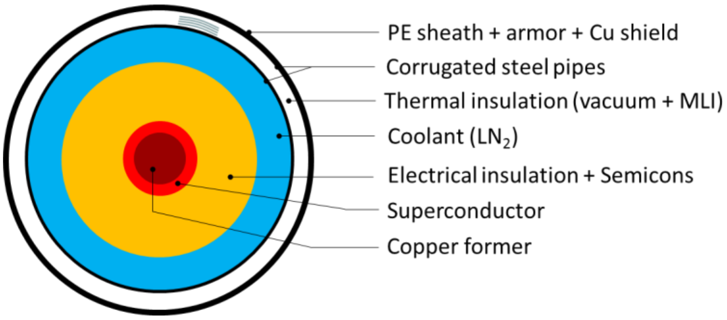

Figure 10.4 Layout of the DC HTS cable

The design of the HTS cables for possible application to the connection system of the offshore wind park is carried out in chapter 8. However, a commercially-available second-generation HTS conductor (YBCO coated conductor) is considered [8.4]. The main characteristics of the tape are listed in Table 10.1.

The critical engineering current density is shown in Figure 10.5 as a function of the applied magnetic field. The cable is designed by assuming that at full power the current density of the superconductor does not exceed 65 % of the critical value. Also, a cable system made of two monopoles with distinct cryostats for closed-loop circulation of the coolant is considered.

Table 10.1. Main characteristics of the HTS tape (YBCO coated conductor)

Manufacturer	Superpower
Type	flat tape
Nominal Width	12 mm
Nominal thickness	0.1 mm
YBCO thickness	1 μm
Stabilizer (Copper)	2×20 μm
Substrate (Hastelloy)	50 μm
Critical tensile strength	550 MPa
Critical current, 77 K – self field	330 A

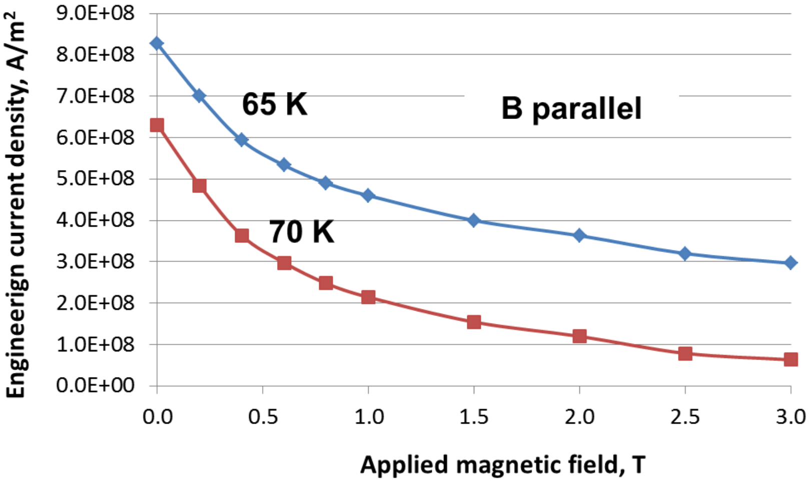

Figure 10.5 Critical current density of the HTS tape versus applied field parallel to the wide side of the tape

The operating temperature range is 65 K – 70 K. Furthermore, a minimum pressure of 2 bar for the LN_2 as a design constraint is assumed to increase the temperature margin before bubble formation starts. This would be detrimental for the insulation of the cable. The total heat load $\dot{Q}$ of the cable in W is given by:

$$\dot{Q} = 2(\lambda \pi D L_{\text{cable}} + 2k I_{\text{cable}}) \tag{10.1}$$

where λ is the heat load per unit surface (W/m^2) due to radiation, L_{cable} is the length of the cable, D is the diameter of the innermost cryopipe, k is the heat load from each termination in W/kA and I_{cable} is the current of the cable in kA. The factor 2 before the parenthesis at the right hand side of equation (10.1) is needed to take into account the heat load of the two monopoles, which also serve as go and return path for the coolant. Electromagnetic losses of the cable's core are neglected due to the DC operation. The diameter D of the cryopipe is one of the outputs of the thermo-hydraulic design of the cable and increases with the distance between the cooling stations [6.11]. Here it is assumed that, no intermediate re-cooling of LN_2 is carried out along the cable (which would require dedicated cooling apparatus with additional platforms), so the distance between the cooling stations coincides with the length of the cable. It must be pointed out that, as far as relatively low voltage is considered, optimization can be achieved by integrating the electric core of the two monopoles in one single cryostat and by providing a return path for the coolant within the same cryostat [6.15] and [10.14]. Though more complex in terms of manufacturing and maintenance, this approach has the potential to reduce the total heat load of the cable. Therefore, the results reported in the following, in terms of heat load, should be considered as a higher limit as they refer to two distinct monopoles.

The main characteristics of the HTS cables designed for application at the cluster collector, the park collector and the park–to-shore link are listed in Table 10.2. Results shown are obtained based on the assumptions detailed in [6.11]. One single HTS cable of the cluster collector grid connects three turbines to the cluster connection point (see Figure 10.1). Hence, it has three terminations; its power rating changes from 5 MW to 15 MW along the cable's length depending on the number of turbines connected upstream. The current and the amount of superconductor change accordingly. The total heat load from radiation is relatively moderate for the park collector due to the small diameter needed for the cryogenic pipe whereas it becomes much greater for the park to shore link. Despite the small diameter of the cryopipe the overall radiated heat is large also for the cluster collector due to the total cabling length. Heat load due to terminations is in general much lower than the part due to radiation on the whole cable length, with the exception of the cluster collector where it is comparable due to the high number of terminations needed. Note that the heat load from terminations increases with the current, and hence with the power. Values reported in Table 10.2 refer to full power. Lower heat load from terminations is obtained at reduced load. Heat load due to radiation is instead independent of the power transfer in the HTS cable. The related cooling power must continuously (24/7) be provided, also in no load condition, in order to assure the availability of the cable. Concerning the park-to-shore link it can be seen that the operating voltage does not have a strong impact on the total heat load. In fact only a 10 % increase is obtained when passing from ± 20 kV to ± 150 kV. However, the voltage has a drastic impact on the amount of superconductor needed due to the lower current; superconducting material can be reduced by 88 % when increasing the voltage from ± 20 kV to ± 150 kV. The amount of the materials (superconductor, copper, electrical insulation, stainless steel and MLI) needed for the manufacturing of the HTS cables is also given in Table 10.2 as it will be used as input for estimating the costs in section 10.5. A thickness of 1 mm is considered for the stainless steel pipes.

Table 10.2. Main characteristics of the DC HTS cables installed within the offshore wind park

	Custer collector at ± 2.5 kV	Park collector at ± 20 kV	Park to shore link at ± 20 kV	Park to shore link at ± 150 kV
Rated power, MW	5 – 15	90	360	360
Current of the cable, kA	1 – 3	2.25	9	1.2
Total cabling length, km	76 (19 × 4)	32 (8 × 4)	50	50
Radius of the copper former, mm	6	6	12	6
Diameter of the inner cryopipe, mm	37.4	41.9	157	170
Temperature of LN_2 at inlet section, K	65	65	65	65
Temperature of LN_2 at outlet section, K	70	70	70	70
Pressure of LN_2 at inlet section, bar	5	5	20	20
Pressure of LN_2 at outlet section, bar	2	2	2	2
Mass flow rate of LN_2, kg/s	0.15	0.18	3.2	3.5
Total heat load due to the radiation (all cables, whole length), kW	28.6	13.1	64.0	68.8
Total heat load due to all terminations (at full power), kW	14.4	1.8	1.8	0.24
Total heat load, kW	43.0	14.9	65.8	69.4
Amount of copper per km of cable (one pole), ton	1.0	1.0	4.1	1.0
Amount of electrical insulation per km of cable (one pole), kg	3.9	37.3	65.0	1000.0
Amount of thermal insulation (MLI) per km of cable (one pole), m^2	117	132	494	534
Amount of stainless steel (cryopipes) per km of cable (one pole), kg	3030	3240	8750	9350
Amount of 12×0.1 mm^2 HTS tape per km of cable (one pole), km	4.7 (average)	6.3	27.9	3.3

10.3. LOSS CALCULATION

The losses of the connection system of the wind park occur in the copper cables, the transformers and the converters. If HTS technology is used no significant losses occur in the cable. However, cooling power is required for the operation of HTS cables which must be taken into account instead. The losses of the various components are examined in detail here.

10.3.1. Losses of AC and DC Copper cables

24 AC cables with 33 kV rated voltage and 15 MW rated power are considered for the AC cluster collector and park collector, respectively. An AC cable with 220 kV rated rms voltage and 360 MW rated power is considered for the park-to-shore link. A three-core submarine cable with XLPE insulation is considered in the first case. Three single core cables are considered in the second case.

The main part of the losses of the AC cable occurs due to the ohmic dissipation of the copper core. Further loss components, which can be comparable to the core's loss, are due to current induced in the metallic shield and the armor, respectively, and to dielectric losses. It is pointed out that losses occur also in no-load conditions (p_{nl}) due to the flow of the reactive power produced by the cable.

According to the model developed in [10.15] the overall loss of the three-phase AC cable is given by:

$$P_{\mathrm{ACcable}} = p_{\mathrm{nl,a}}\, L_{\mathrm{cable}} + p_{\mathrm{nl,b}}\, L_{\mathrm{cable}}^{3} + p_{\mathrm{l}}\, L_{\mathrm{cable}} \left(\frac{S}{S_{\mathrm{n}}} \right)^{2} \tag{10.2}$$

where P_{ACcable} is the total loss of the three phase cable in W, L_{cable} is the length of cable in km, S is the transmitted apparent power in VA and S_{n} is the nominal rating in VA. This model takes into account all the loss phenomena. The parameters of the model were obtained from the physical parameters of actual commercial 33 kV [10.16] and 220 kV [10.17] cables and are listed in Table 10.3 for the voltage rating of interest.

Table 10.3. Parameters of the loss model of AC cables

	$p_{\mathrm{nl,a}}$, W/km	$p_{\mathrm{nl,b}}$, W/km^3	p_{l}, W/km
33 kV – 15 MW	21.48	0.42	62000
220 kV – 360 MW	530.30	0.30	51000

Concerning the conventional (copper) DC cable only the Joule loss of the core needs to be considered since the other dissipative phenomena do not occur during DC operation. Therefore, the total loss of a DC bipole (2 conductors) operating at ± V_{n} (in V) can be expressed as:

(10.3) $$P_{\mathrm{DCcable}} = \rho\, J_{\mathrm{n}} \frac{P_{\mathrm{n}}}{V_{\mathrm{n}}} L_{\mathrm{cable}} \left(\frac{P}{P_{\mathrm{n}}} \right)^2$$

where P_{DCcable} is the total loss of the bipole in W, ρ is the resistivity of Copper in Ωm, P is the transmitted power in W, P_{n} the nominal power in W and J_{n} is the design current density in A/m^2 at nominal power. The design current density J_{n} changes depending on the spacing between the monopoles and the climate. In the following we assume J_{n} = 1 A/m^2 which is a typical value. As for the resistivity of the copper, we assume ρ = 2.1 Ωm, which is the value corresponding to 70 °C.

10.3.2. Losses of the transformers

Loss of transformers can be estimated as follows:

(10.4) $$P_{\mathrm{transformer}} = p_{\mathrm{nl}}\, S_{\mathrm{n}} + p_{\mathrm{l}}\, S_{\mathrm{n}} \left(\frac{S}{S_{\mathrm{n}}} \right)^2$$

where p_{nl} and p_{l} are the no-load and load losses in per unit, S_{n} is the nominal rating of the transformer in VA and S is the input apparent power of the transformer in VA. Equation (10.4) is based on the assumption that losses of the ferromagnetic core and the input voltage of the transformer do not depend on the load condition. The parameters of the model were deduced from the data of actual power transformers [10.18] and are listed in Table 10.4 for the rating of interest.

Table 10.4. Parameters of the loss model of the transformers

	p_{nl}	p_l
5 MVA- 3.3 kV / 33 kV	0.09 %	0.69 %
360 MVA 33 kV / 220 kV	0.05 %	0.40 %

10.3.3. Losses of the converters

The efficiency of the three-level neutral-point clamped AC-DC converter with 5 MW rating installed at the output of PMSG generator is shown in Figure 10.6 as a function of the input power. The efficiency of the DAB with 5 MW rating is also shown in Figure 10.6. These curves were obtained after detailed design and simulation of the converters and take into account conduction losses, switching losses, losses of the clamping circuit and losses of the DAB transformer [10.1]. The efficiency curve of the 3L-NPC AC-DC converter reported in Figure 10.6 also applies for the cascade DC-AC converter which is used in back-to-back if an AC output is required for the wind turbine (see 10.1.1). However, in this case, additional losses due to the grid-side filter also need to be taken into account. In the following it is assumed that the filter losses amount to 1.0 % of the converted power. It is pointed out that if a larger DC-DC converter is built using a modular assembly of 5 MW DAB modules, the same efficiency curve applies, because the control is assumed to balance the power sharing of all modules. Concerning the HV DC-AC conversion station required at the shore connection point with the power grid in case of DC operation of the park-to-shore link the efficiency of 97.8 % is assumed according to [10.15].

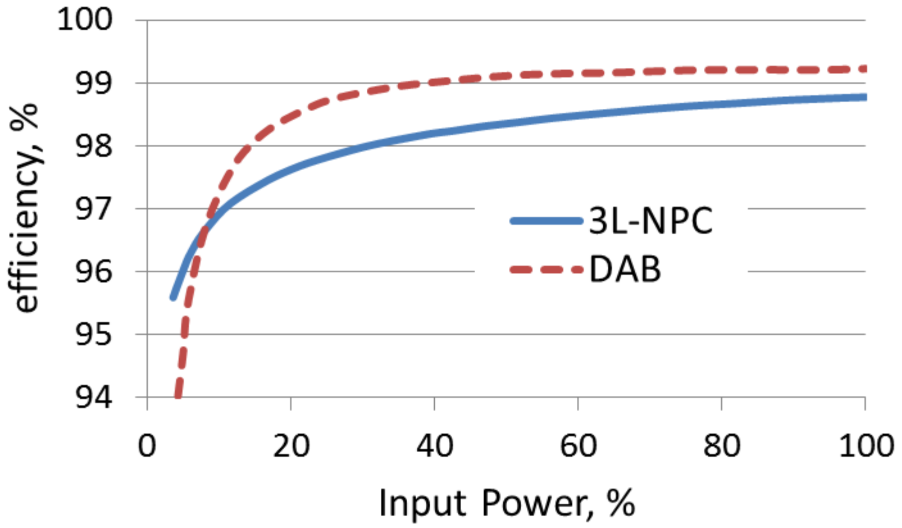

Figure 10.6 Efficiency of machine-side three-level neutral-point clamped (3L-NPC) converters and dual-active bridge (DAB) converters [10.1]

10.3.4. Cooling power of HTS cables

The cooling power, which is needed to transfer the total heat load $\dot{Q}$ from the liquid nitrogen at 70 K (the temperature at the outlet section of the cable) to the external ambient at 300 K, is given by:

$$P_{\text{cooling}} = COP \cdot \dot{Q} \tag{10.5}$$

where *COP* is the coefficient of performance of the cooling system [6.11]. In the following *COP* = 22 is assumed, which corresponds to 15% of the theoretical (Carnot) efficiency for heat transfer from 70 K to 300 K. This value of *COP* is typical for real cooling machines with cooling capacity in the kW range operating in the considered temperature interval [6.11]. The heat load $\dot{Q}$

can be calculated from equation (10.1) and the values for the considered cables are listed in Table 10.2.

10.4. COST OF CONVENTIONAL (NON-HTS) COMPONENTS

The model developed in [10.1] and [10.15] is used for estimating the cost of the components. The main results are summarized below.

10.4.1. Cost of copper cables and transformers

he cost per unit length of the conventional AC and DC cables in k€/km is given by equations(10.6) and (10.7), respectively:

$$C_{\mathrm{AC\,cable}} = a + b e^{\alpha S_{\mathrm{n}}} \quad (10.6)$$

$$C_{\mathrm{DC\,cable}} = a + b P_{\mathrm{n}} \quad (10.7)$$

where S_n is the rated apparent power (in VA) of the AC cable or the transformer and P_n is the rated power (in W) of the DC cable. The parameters of the cost model are listed in Table 10.5. Concerning the transformers, a cost of 18 €/kVA both for the turbine and the park transformers is assumed.

Table 10.5. Parameters of the cost models for AC cables, DC cables and transformers [10.15]

	a	b	α
AC cables			
33 kV	4.34 k€/km	62.9 k€/km	4.1×10^{-8} 1/VA
220 kV	335.5 k€/km	11.6 k€/km	1.16×10^{-8} 1/VA
DC cables			
± 2.5 kV	–36.5 k€/km	4.3×10^{-5} k€/km/W	
± 20 kV	–33.1 k€/km	6.5×10^{-6} k€/km/W	
± 150 kV	30.2 k€/km	1.0×10^{-6} k€/km/W	

10.4.2. Cost of the converters

The cost of the converters is given by

$$C_{\mathrm{converter}} = (c_{\mathrm{sw}} + c_{\mathrm{aux}}) P_{\mathrm{n}} \tag{10.8}$$

with P_n the rating of the converter in VA. Equation (10.8) applies both for DC-DC converters (made of DAB blocks), and for the AC-AC converter (made of 3L-NPC blocks). Coefficient c_sw is the cost per unit VA of the power-electronic switches. c_aux is the cost per unit VA of auxiliary components such as filters and snubber circuits. In case of a DC-DC converter c_aux also includes the medium-frequency transformer of the DAB. A value of c_sw = 40 €/kVA is assumed for both the AC-DC and DC-DC converter. Furthermore, c_aux = 5 €/kVA is assumed for the AC-DC converter and c_aux = 0.86 €/kVA is assumed for the DAB converter. The low value of the latter case comes from the fact that, differently than for the AC-DC converter where a sine-wave AC output voltage is aimed at (which requires heavy filtering), no demanding requirements exist on the waveform of the voltage at the AC stage of the DAB-based DC-DC converter (see Figure 10.3).

10.4.3. Cost of the platform

Additional platforms may be required for placing power-electronic converters and transformers depending on the layout chosen for the park connection system. The cost of these platforms must be included in the cost comparison of the various connection systems. The cost in € of the platform is given by:

$$C_{\mathrm{platform}} = a + b\,P \tag{10.9}$$

where P is the overall power (in W) of the converters installed on the platform. As indicated in [10.15], here, a value of 2.2×10^6 € for the offset coefficient a and a value of 0.07 € / VA for the slope coefficient b is assumed. If HTS cables are used, a cooling system is also required and is to be installed on the platforms. In this case we assume that equation (10.9) still valid with P indicating the sum of the power of the converters and the power of the cooling system.

10.5. COST EVALUATION OF HTS CABLE SYSTEM

The cost of the DC HTS cable system is given by the sum of the cost of the cable itself, the cost of the cooling apparatus and the cost of the terminations. The cost of HTS cables largely depends on the cost of the raw materials. In fact, as for conventional Cu/XLPE cables, the costs of manufacturing are rather marginal and can be estimated as a 25 % of the cost of the materials [6.16]. As for the cryopipe, however, a higher manufacturing cost can be expected, which here it is assumed to be 60 % of the cost of the stainless steel. The amount of each material (copper, superconductor, electrical insulation, stainless steel and MLI) needed per km of the considered cables is listed Table 10.2. The unit costs of the materials are listed in Table 10.6 [10.20]. The cost of the 2G-HTS today is 100 €/kA/m for operation in self-field at 77 K [10.21] and [10.22]. This implies that the cost per unit length of the reference 12×0.1 mm^2 tape (which carries 330 A in self-field at 77 K, see Table 10.1) is 33 €/m. However, cost reduction down to at least 20 €/kA/m can be expected for this material in the very near future due to both technology advances and increase of demand [10.22] and [10.23]. This corresponds to a cost of the reference 12×0.1 mm^2 tape of 6.6 €/m. Both of these cost data are considered in the following analysis for the HTS tape. The unit cost (per watt of heat load) of the cooling system operating from 70 K to 300 K is also reported in Table 10.6 [10.24]. This data is realistic today and is expected to be reduced in the future due to technology and market developments.

Table 10.6. Unit cost of HTS cable materials and cooling system

HTS tape	33 €/m (corresponding to 100 €/kAm) 6.6 €/m (corresponding to 20 €/kAm)
Stainless steel for cryopipes	5.5 €/kg
Electrical insulation (wrapped PPLP)	10 €/kg
Copper	5.6 €/kg
Multilayer insulation	27 €/m^2
Cooling system	100 €/W_{cold}

The costs of materials, manufacturing and cooling per unit length of DC HTS cables are reported in Table 10.7. They are obtained by combining the amount of materials given in Table 10.2 with unit costs given in Table 10.6. The overall cost per unit length of the cables is also reported in the Table 10.7. It should point out that the present cost analysis does not include the terminations. However, since the length of the considered cables is several km, the cost of terminations is not expected to have a high impact to the final cost. It can be seen from Table 10.7 that, based on today’s quotation of 100 €/kAm, the cost of HTS completely overwhelms the cost of other components for high-current cables. For example, the incidence of HTS on the total cost is 80 % for the park collector at ± 20 kV, whereas it reduces to 31 % for the park-to-shore link at ±150 kV due to the lower operating current (it must be considered that the amount of HTS needed increases much more than linearly with the transport current of the cable due to strong decrease of the tape’s performance with the magnetic field, see Figure 10.5). However, a drastic reduction of the incidence of the HTS and, hence, of the overall cost of the cable is obtained when the near-term unit cost of 20 €/kAm is considered. For example a reduction of about 58 % (from 289.9 k€/km to 122.4 k€/km) is obtained for the cost of the DC park collector at ± 20 kV when passing from 100 €/kAm to 20 €/kAm. The comparison of the costs of HTS cables and conventional AC and DC cables is carried out in section 10.6.2.

Table 10.7. Cost of materials, manufacturing and cooling and overall cost per unit length of DC HTS cables (one pole). All data are in k€/km. Terminations neglected

	Custer collector at ± 2.5 kV	Park collector at ± 20 kV	Park–to-shore link at ± 20 kV	Park–to-shore link at ± 150 kV
HTS tape (with 100 €/kAm unit cost)	155.6	209.3	922.0	107.1
HTS tape (with 20 €/kAm unit cost)	31.1	41.9	184.4	21.4
Copper	5.7	5.7	22.7	5.7
Electrical insulation	0.0	0.4	0.7	10.0
thermal insulation (MLI)	3.2	3.6	13.3	14.4
Stainless steel (cryopipes)	16.7	17.8	48.1	51.5
Manufacturing	12.2	13.1	38.1	38.4
Cooling system	28.3	23.3	65.8	69.0
Total cost with HTS at 100 €/kAm	**221.7**	**273.2**	**1110.7**	**296.1**
Total cost with HTS at 20 €/kAm	**97.2**	**105.7**	**373.1**	**210.4**

10.6. LOSS AND COST COMPARISON OF WIND PARK CONNECTION SYSTEMS

10.6.1. Loss comparison

The losses in one year of the various connection systems taken into account for the wind park are shown in Table 10.8. Seven different cases are considered. Each case is distinguished by means of the type of operation (AC or DC), the type of material (Cu or HTS) and the voltage level which are used for the cluster and the park collector, respectively, and for the park-to-shore link. The yearly loss of each of the components is obtained by taking the time integral over one year of the instantaneous loss discussed in section10.3. The time-dependence of the input power of the components is obtained from the productivity data of the wind park presented in section 10.1.2. Values of Table 10.8 are given in GWh. The total loss of each solution is also given in Table 10.8 as a percentage of the total energy produced by the generators in one year, which is 1630 GWh. The all-AC solution (cluster/park collector at 33 kV and park to shore link at 220 kV) has a total loss of 138.9 GWh, corresponding to 8.5 % of the production. A significant share of this loss is due to the Joule heating of the 33 kV cables. Copper-based DC solutions are able to reduce the loss of the cluster and the park collector cables, though an additional conversion is required which adds losses. Furthermore, it is to be considered that the conversion losses at the turbine are much greater for the AC solution (623 GWh vs. 23.4 GWh) due to the double power-electronic conversion needed. As a final result, the three-stage Cu-based DC solution (with the cluster collector at ± 2.5 kV, park collector at ± 20 kV and shore link at ± 150 kV), has in practice lower total losses then the AC solution (120.4 GWh vs 138.9 GWh) in the particular scenario analyzed and with the assumptions mentioned above. In contrast, though appealing because one conversion is not required, the Cu-based DC solution with park to shore link at ± 20 kV is not practical due to the large level of losses (69.1 GWh) occurring in this cable.

Table 10.8. Losses in one year of the Wind Park connection systems (all data are in GWh)

Cluster collector	Cu-AC 33 kV	Cu-DC ± 2.5 kV	Cu-DC ± 2.5 kV	Cu-DC ± 2.5 kV	Cu-DC ± 2.5 kV	HTS-DC ± 2.5 kV	HTS-DC ± 2.5 kV
Park collector	Cu-AC 33 kV	Cu-DC ± 20 kV	Cu-DC ± 20 kV	HTS-DC ± 20 kV	HTS-DC ± 20 kV	HTS-DC ± 20 kV	HTS-DC ± 20 kV
Park to shore link	Cu-AC 220 kV	Cu-DC ± 20 kV	Cu-DC ± 150 kV	HTS-DC ± 20 kV	HTS-DC ± 150 kV	HTS – DC ± 20 kV	HTS-DC ± 150 kV
Joule loss of cluster collector cables	46.4	11.7	11.7	11.7	11.7	0.0	0.0
Joule loss of park collector cables		11.1	11.1	0.0	0.0	0.0	0.0
Joule loss of park to shore link	10.2	69.1	9.2	0.0	0.0	0.0	0.0
loss of turbine transformers	12.5	0.0	0.0	0.0	0.0	0.0	0.0
loss of park transformers	7.5	0.0	0.0	0.0	0.0	0.0	0.0
loss of turbine converters	62.3	23.4	23.4	23.4	23.4	23.4	23.4
loss of converters at the cluster connection point	0.0	14.6	14.6	14.6	14.6	14.6	14.6
loss of converters at the park connection point	0.0	0.0	14.6	0.0	14.6	0.0	14.6
loss of converters at the shore connection point	0.0	35.9	35.9	35.9	35.9	35.9	35.9
Cooling loss of cluster collector cables	0.0	0.0	0.0	0.3	0.3	0.3	0.3
Cooling loss of park collector cables	0.0	0.0	0.0	0.1	0.1	0.1	0.1
Cooling loss of park to shore link	0.0	0.0	0.0	0.6	0.6	0.6	0.6
Total losses	**138.9**	**165.7**	**120.4**	**86.6**	**101.2**	**74.9**	**89.6**
Total Losses in % of yearly production	**8.5 %**	**10.2 %**	**7.4 %**	**5.3 %**	**6.2 %**	**4.6 %**	**5.5 %**

The performance of the DC solution is greatly improved, if HTS technology is used since Joule losses of the cables are completely cancelled. Additional cooling power which must be provided for the operation of the HTS is in the range 0.1-0.6 GWh and hence is negligible with respect to the losses avoided. As a result, the overall losses of the three voltage-level DC solution (cluster collector at ± 2.5 kV, park collector at ± 20 kV and shore link at ±150 kV) change from 120.4 GWh to 89.6 GWh. Moreover, a DC connection system to the shore at ± 20 kV becomes possible, and furthermore this is the best-performing solution with an overall loss of 4.6 %, since the losses of the converters at the park connection point are avoided without having the drawback of the large losses in the transmission cable. However, it should be pointed out that a limit in overall loss reduction exists also in case of HTS since the losses of the converters cannot be avoided. In fact, as it can be seen from the table, the limiting factor that is common to all the DC solutions (both Cu or HTS) is the relevant loss of 35.9 GWh occurring the DC-AC conversion station at shore.

10.6.2. Cost comparison

The costs of the various connection systems considered for the wind park are shown in Table 10.9. A unit cost of superconductor of 100 €/kA/m is considered for the evaluation of the cost of the HTS cables. The total cost of the loss in one year is also reported Table 10.9. T This data is deduced from the values reported in Table 10.8 by assuming a unit cost of energy of 100 €/MWh. All values of Table 10.9 are in M€. For comparison purposes, the capital cost of the connection system and the missed income due to the losses during the whole lifetime of the wind park must be merged together. For this scope the following net present value in M€ of the connection system is introduced:

$$NPV = C_{\mathrm{TOT}} + E\sum_{i=1}^{N}\frac{1}{(1+v)^{i}} \tag{10.10}$$

where C_{TOT} is the total capital cost of the connection system (in M€), E is the cost of the loss in one year, N is the active life time of the wind park in years, and v is the discount rate. By using (10.10) it is implicitly assumed that the productivity and the cost of the losses do not change during the lifetime of the wind park. In the following a lifetime of 25 years and a discount rate of 6 % are considered. We point out that no claim is made in this section to provide investment indications. The only purpose is to have a comparative indication of the economic impact of the loss of the various connection systems.

As it can be seen from Table 10.9 the smallest capital cost (158.0 M€) is obtained with the AC connection system. A comparable cost (172.5 M €) is obtained with the conventional (Cu) DC solution with the shore link at ±150 kV. Much higher capital costs (up to 269.4 M€) are obtained with full HTS DC solutions, and in particular if an HTS park-to-shore link at ±20 kV is considered. This is due to the large amount of HTS tape which is required for the manufacturing of this cable (see Table 10.7). However, based on today’s quotation of 100 €/kA/m, despite the greater capital costs, the HTS solutions are competitive in terms of net present value. In fact, if a full HTS solution with shore link at ±150 kV is considered, an NPV of 317.1 M€ is obtained, which is aligned with that of the Cu-based AC and DC solutions (335.5 M€ and 326.4 M€, respectively).

Table 10.9. Costs of the Wind Park connection systems. A unit cost of 100 €/kAm is assumed for the HTS. All data are in M€

Cluster collector	Cu-AC 33 kV	Cu-DC ± 2.5 kV	Cu-DC ± 2.5 kV	Cu-DC ± 2.5 kV	Cu-DC ± 2.5 kV	HTS-DC ± 2.5 kV	HTS-DC ± 2.5 kV
Park collector	Cu-AC 33 kV	Cu-DC ± 20 kV	Cu-DC ± 20 kV	HTS-DC ± 20 kV	HTS-DC ± 20 kV	HTS-DC ± 20 kV	HTS-DC ± 20 kV
Park to shore link	Cu-AC 220 kV	Cu-DC ± 20 kV	Cu-DC ± 150 kV	HTS-DC ± 20 kV	HTS-DC ± 150 kV	HTS – DC ± 20 kV	HTS-DC ± 150 kV
Turbine transformers	6.5	0.0	0.0	0.0	0.0	0.0	0.0
Park transformers	6.5	0.0	0.0	0.0	0.0	0.0	0.0
Turbine converters	36.3	14.7	14.7	14.7	14.7	14.7	14.7
Converters at the cluster connection point	0.0	14.7	14.7	14.7	14.7	14.7	14.7
Converters at the park connection point	0.0	0.0	14.7	0.0	14.7	0.0	14.7
Converters at the shore connection point	0.0	16.2	16.2	16.2	16.2	16.2	16.2
Platforms at the cluster connection point	0.0	34.0	34.0	34.0	34.0	34.1	34.1
Platform at the park connection point	27.4	27.4	27.4	27.4	27.4	27.4	27.4
Cables of the cluster collector	30.7	13.6	13.6	13.6	13.6	33.7	33.7
Cables of the park collector cables		17.7	17.7	17.5	17.5	17.5	17.5
Cables of the park to shore link	54.5	115.3	19.5	111.1	29.6	111.1	29.6
Total cost	**158.0**	**253.6**	**172.5**	**249.2**	**182.4**	**269.4**	**202.6**
Total cost of the losses in one year	**13.9**	**16.6**	**12.0**	**8.7**	**10.1**	**7.5**	**9.0**
Net Present Value	**335.5**	**465.4**	**326.4**	**359.9**	**311.8**	**365.1**	**317.1**

Cost data of the connection systems which are obtained if a unit cost of 20 €/kAm is considered for the superconductor are shown in Table 10.10. As it can be seen the competitiveness of the HTS solution is drastically increased in this case. In fact, with the exception of the conventional DC solution with a shore link at ± 20 kV, the capital costs of all other solution are comparable in this case. This is true in particular for the full-HTS solution with a shore link at ± 20 kV, which is the one with the least overall loss. This implies that the lowest NPV of 261.7 M€ is obtained with this solution, which hence is the most appealing in economic terms. Note that also the other HTS or hybrid Cu-HTS DC solutions have a net present value lower than the one of the Cu AC solution.

A hybrid (HTS and Cu) DC connection system with two-stage DC collector grids (Cu at ± 2.5 kV and HTS at ± 20 kV) and HTS DC transmission at ± 150 kV offers reduced losses and is cost competitive with respect to AC connection systems based on today's quotation of HTS material of 100 €/kA/m. In the near future, as soon as the foreseen reduction of the cost of HTS material down to 20 €/kA/m is achieved, a full HTS DC connection system comprising a two-stage collector (HTS at ± 2.5 kV and HTS at ± 20 kV) and HTS DC transmission at ± 20 kV becomes the most cost-effective solution.

Table 10.10. Costs of the Wind Park connection systems. A unit cost of 20 €/kAm is assumed for the HTS. All data are in M€

Cluster collector	Cu-AC 33 kV	Cu-DC ± 2.5 kV	Cu-DC ± 2.5 kV	Cu-DC ± 2.5 kV	Cu-DC ± 2.5 kV	HTS-DC ± 2.5 kV	HTS-DC ± 2.5 kV
Park collector	Cu-AC 33 kV	Cu-DC ± 20 kV	Cu-DC ± 20 kV	HTS-DC ± 20 kV	HTS-DC ± 20 kV	HTS-DC ± 20 kV	HTS-DC ± 20 kV
Park to shore link	Cu-AC 220 kV	Cu-DC ± 20 kV	Cu-DC ± 150 kV	HTS-DC ± 20 kV	HTS-DC ± 150 kV	HTS – DC ± 20 kV	HTS-DC ± 150 kV
Turbine transformers	6.5	0.0	0.0	0.0	0.0	0.0	0.0
Park transformers	6.5	0.0	0.0	0.0	0.0	0.0	0.0
Turbine converters	36.3	14.7	14.7	14.7	14.7	14.7	14.7
Converters at the cluster connection point	0.0	14.7	14.7	14.7	14.7	14.7	14.7
Converters at the park connection point	0.0	0.0	14.7	0.0	14.7	0.0	14.7
Converters at the shore connection point	0.0	16.2	16.2	16.2	16.2	16.2	16.2
Platforms at the cluster connection point	0.0	34.0	34.0	34.0	34.0	34.1	34.1
Platform at the park connection point	27.4	27.4	27.4	27.4	27.4	27.4	27.4
Cables of the cluster collector	30.7	13.6	13.6	13.6	13.6	14.8	14.8
Cables of the park collector cables		17.7	17.7	6.8	6.8	6.8	6.8
Cables of the park to shore link	54.5	115.3	19.5	37.3	21.0	37.3	21.0
Total cost	**158.0**	**253.6**	**172.5**	**164.7**	**163.1**	**166.0**	**164.4**
Total cost of the losses in one year	**13.9**	**16.6**	**12.0**	**8.7**	**10.1**	**7.5**	**9.0**
Net Present Value	**335.5**	**465.4**	**326.4**	**275.4**	**292.5**	**261.7**	**278.9**

10.7. REFERENCES

[10.1] M. Stieneker, B. J. Mortimer,N. R. Averous, H, Stagge, and R. W. De Doncker, “Optimum Design of Medium-Voltage DC Collector Grids Depending on the Offshore-Wind-Park Power,” 2014 IEEE Symposium Power Electronics and Machines for Wind and Water Applications (PEMWA), 24-26 July 2014, Milwaukee, WI, pages: 1-8, DOI:10.1109/PEMWA.2014.6912218

[10.2] Areva, (2013, November), Technical description, Documentation, Areva, online available at: http://de.areva.com/EN/areva-wind-313/m5000-technical-data.html

[10.3] C.Meyer, “Key components for future offshore dc grids,” PhD Thesis, RWTH Aachen University, Aachen, Germany, Institute for Power Generation and Storage Systems, E.ON Energy Research Center, 2007

[10.4] K. Argyriadis, G. Fischer, P. Frohbose, D. Kindler, and F. Reher: “Forschungsplattform FINO 1 – einige Messergebnisse,” InfoPlus-Jahresbilanz Borkum 9, 2005, available online: http://goo.gl/uxK0y3

[10.5] http://www.fino1.de/en/

[10.6] E.H. Camm and et. al. “Wind power plant collector system design considerations: IEEE PES wind plant collector system design working group,” IEEE Power & Energy Society General Meeting , PES’09, 26-30 July 2009, Calgary AB, pages: 1-7, DOI: 10.1109/PES.2009.5275322

[10.7] P. Bresesti, W. L. Kling, R. L. Hendriks, R. Vailati, "HVDC Connection of Offshore Wind Farms to the Transmission System," IEEE Transactions on Energy Conversion, Vol.22, No.1, pages: 37-43, March 2007, DOI: 10.1109/TEC.2006.889624

[10.8] R. W. De Doncker, D. M. Divan, M. H. Kheraluwala, "A three-phase soft-switched high-power-density DC/DC converter for high-power applications," IEEE Transactions on Industry Applications, Vol. 27, No. 1, 1991, pages: 63-73, DOI: 10.1109/28.67533

[10.9] S. P. Engel, N. Soltau, H. Stagge, and R. W. De Doncker, "Dynamic and balanced control of three-phase high-power dual-active bridge dcdc converters in dc-grid applications," IEEE Transactions on Power Electronics, Vol. 28, No. 4, 2013, pages: 1880–1889, DOI: 10.1109/TPEL.2012.2209461

[10.10] N. Soltau, H. Siddique, and R. De Doncker, "Comprehensive modeling and control strategies for a three-phase dual-active bridge," in Renewable Energy Research and Applications (ICRERA), 2012 International Conference on, 11-14 November 2012, Nagasaki, pages: 1-6, DOI: 10.1109/ICRERA.2012.6477408

[10.11] R. Lenke, H. van Hoek, S. Taraborrelli, R. W. De Doncker, J. San Sebastian, I. Etxeberria-Otadui, "Turn-off behavior of 4.5 kV asymmetric IGCTs under zero voltage switching conditions," Proceedings of the 2011-14th European Conference on Power Electronics and Applications (EPE 2011), Aug. 30 2011-Sept. 1 2011, Birmingham, pages: 1-10, Available Online: http://ieeexplore.ieee.org/stamp/stamp.jsp?arnumber=6020319

[10.12] R. Lenke, "A Contribution to the Design of Isolated DC-DC Converters for Utility Applications," PhD Thesis, RWTH Aachen University, Aachen, Germany, Institute for Power Generation and Storage Systems, E.ON Energy Research Center, 2012

[10.13] M. Hirose, T. Masuda, K. Sato, and R. Hata, "High-Temperature Superconducting (HTS) DC Cable," SEI Technical review, January 2006

[10.14] V.E. Sytnikov, S. E. Bemert, Y. V. Ivanov, S. I. Kopylov, I. V. Krivetskiy, D. S. Rimorov, M. S. Romashov, Y. G. Shakaryan, R. N. Berdnikov, Y. A. Dementyev, Y. A: Goryushin, and D. G. Timofeev, "HTS DC Cable Line Project: On-Going Activities in Russia," IEEE Transactions on Applied Superconductivity, Vol.23, No.3, June 2013, DOI:10.1109/TASC.2013.2245280

[10.15] S. Lundberg, "Performance comparison of wind park configurations," Göteborg, 2003, online available at: http://webfiles.portal.chalmers.se/et/Reports/PCWPC_Reports.pdf

[10.16] Submarine Power Cables, Nexans technical Brochure, on line, available at: http://goo.gl/REmmnk

[10.17] High Voltage Cables, Prysmian technical Brochure, on line, available at: http://goo.gl/9bdDqM

[10.18] "HV / MV power transformers", ENEL distribuzione Technical Document DT 1083 (in Italian)

[10.19] J. W. Kolar, "Future Challenges for Research and Teaching in Power Electronics", available online: http://www.powerelectronics.ac.uk/power-electronics/documents/prof-dr-johann-w-kolar.pdf

[10.20] "Program on Technology Innovation: a Superconducting DC Cable", EPRI 1020458, Final report, December 2009, online available at: http://goo.gl/7zQcpD

[10.21] X. Obradors and T. Puig, "Coated conductors for power applications: materials challenges", Superconductor Science and Technology, Vol. 27 No. 4, 2014, http://goo.gl/R85Sj1

[10.22] S. H. Moon, "HTS Development and Industrialization at SuNAM", 1st Workshop on Accelerator Magnets in HTS, DESY, 21-23 May 2014, https://goo.gl/rASiY6

[10.23] V. Matias and R. H. Hammond, "HTS superconductor wire: $5/kAm by 2030?", International Workshop on Coated Conductor s for Applications, Jeju Island, Korea, December 2014, http://goo.gl/6gUXBO

[10.24] Navigant Consulting, Inc., "High Temperature Superconductivity Market Readiness Review", August 2006, available on line at: http://goo.gl/uqi311

11. TRANSIENT BEHAVIOR OF SUPERCONDUCTING HVDC LINK

Increasing the penetration of the renewable energy resources is the most important issue for the future power system. The renewable generations, unlike the conventional energy generation, need more space and they install in the rural areas which are far from the load centers, e.g. domestic and industrial loads. Transmitting higher amount of the energy in long distance is a challenge for the future power systems.

Several research studies show the performance of the high voltage direct current (HVDC) links over the high voltage alternative current (HVAC) in longer distance technically and economically. Line commutated converters (LCC) based HVDC systems are in use since 1970s. Recently, thanks to the improvement in high frequency power electronic switches and modular converters, voltage source converters (VSC) based HVDC is coming to the market (HVDC plus by Siemens or HVDC light by the ABB). However, for large power transmission, LCC based HVDC system is the solution where the high-power and high-voltage, VSC based HVDC system is not feasible regards to the state of the art.

Superconducting cables with higher current carrying capacity compared to the normal conductor cable at the same size, and also zero resistivity of the superconductors in DC applications makes the superconducting DC cable a suitable candidate for increasing the power transmission in the power systems.

High temperature superconductors have smaller cooling requirements compared to the low temperature superconductors; therefore the cost of the high temperature devices is less than the low temperature devices. The performance of the HTS materials for manufacturing the cables are proven by several prototype worlds wide.

In this chapter, an HVDC transmission link using 12-pulse thyristor based converter and an HVDC system based on voltage source converter will be discussed in details for the same power rating. For both of the systems, transient behavior of the HVDC transmission link with HTS cable by applying different perturbation will be studied, which is crucial for stability of the system. These perturbations are programmed and/or unplanned changes in the steady state condition of the HVDC link. AC and/or DC side short circuit is the main perturbation in the system.

Transient currents and steady state current ripples may introduce AC loss in the HTS cable. The AC loss and the relevant temperature rise in the superconducting materials are affecting the performance of the HTS cable. Understanding the transient current and current ripple in the HTS is the preliminary study for calculating the AC losses in the cable.

11.1. DESCRIPTION OF THE HVDC TRANSMISSION SYSTEM

11.1.1. Thyristor based HVDC system

A 6400 MW (±320 kV, 10 kA) DC link is used to transmit power from a 500 kV, 20000 MVA, and 50 Hz system to a 345 kV, 20000 MVA, and 50 Hz system. The AC systems are represented by the lumped L-R equivalents.

The rectifier and the inverter are 12-pulse converters which consist of two series connected 6-pulse three phase thyristor base converter on DC side. Three winding transformers with Wye grounded/Wye/Delta makes phase difference in the AC side three phase voltage of the converters and these two 6-pulse converters is seen as 12-pulse, by the network and DC side of the converter. The rectifier and inverter of the HVDC link are interconnected through a 2000-km line and 0.5 H smoothing reactors. The transformer tap changers considered as a fixed position determined by a multiplication factor applied to the primary nominal voltage of the converter transformers.

From the AC side point of view, an HVDC converter acts as a source of harmonic currents. And from the DC side point of view, it is a source of harmonic voltages. The order h of these characteristic harmonics is related to the pulse number p of the converter configuration: $h_{AC} = k \times p \pm 1$ for the AC current and $h_{DC} = k \times p$ for the DC voltage, k being any integer. In the studied case, $p = 12$, so that injected harmonics on the AC side are 11, 13, 23, 25, and on the DC side are 12, 24.

For compensating the odd characteristic harmonics of the converters, AC filters are used in the connection point of the converters in the AC system in order to prevent spreading out the harmonic currents on the AC system. The filters also appear as large capacitors at the fundamental frequency, thus providing reactive power compensation for the rectifier consumption due to the firing angle α. The AC filters contains the tuned filters at the 11th and 13th harmonics and the damped filter used to eliminate the higher order harmonics, i.e. 24th and up. Extra reactive power is also provided by capacitor banks.

11.1.2. Voltage source converter based HVDC system

The principal characteristic of VSC-HVDC transmission is its ability to independently control the reactive and real power flow at each of the AC systems to which it is connected, at the point of common coupling (PCC). In contrast to line-commutated HVDC transmission, the polarity of the

DC link voltage remains the same with the DC current being reversed to change the direction of power flow.

A 6400 MW (±320 kV, 10 kA) DC interconnection is used to transmit power from a 500 kV, 20000 MVA, and 50 Hz system to a 345 kV, 20000 MVA, and 50 Hz system. The AC systems are represented by the lumped L-R equivalents. The VSC converters are three-level natural point clamp converter (3L-NPC) using the model of IGBT/diodes. The IGBT can be controlled and it is suitable for high-frequency switching, therefore this device is the better choice over GTO and thyristors. However, as discussed before in 3.1, IGCT is another suitable device for the VSC.

A converter transformer (Wye grounded /Delta) is used to permit the optimal voltage transformation. The winding arrangement blocks triplen harmonics produced by the converter. The transformer tap changers considered in a fixed position determined by a multiplication factor applied to the primary nominal voltage of the converter transformers. The multiplication factors are chosen to have a modulation index around 0.85. The converter reactor and the transformer leakage reactance permit the VSC output voltage to shift in phase and amplitude with respect to the AC system, and allow control of converter active and reactive power output.

To meet AC system harmonic specifications, AC filters have been connected as shunt elements on the converter side of the converter transformer. Since there are only high frequency harmonics, shunt filtering is therefore relatively small compared to the converter rating. In this configuration a high pass filter is sufficient and the tuned filters are not needed. The AC harmonic generation [11.1] mainly depends on the:

- Type of modulation (e.g. single-phase or three-phase carrier based, space vector, etc.)
- Frequency index p = carrier frequency / modulator frequency (e.g. p = 1350/50 = 27)
- Modulation index m = fundamental output voltage of the converter / pole to pole DC voltage

The principal harmonic voltages are generated at and around multiples of p.

The reservoir DC capacitors are connected to the VSC terminals. They have an influence on the system dynamics and the voltage ripple on the DC side. The size of the capacitor is defined by the time constant τ corresponding to the time it takes to charge the capacitor to the base voltage if it is charged with the base current.

The DC side filters blocking high-frequency are tuned to the 3rd harmonic, i.e., the main harmonic present in the positive and negative pole voltages. It is shown that a reactive converter current generates a relatively large third harmonic in both the positive and negative pole voltages [11.2] but not in the total DC voltage. The DC harmonics can also be zero-sequence harmonics (odd multiples of 3) transferred to the DC side (e.g., through the grounded AC filters). A smoothing reactor is connected in series at each pole terminal. To keep the DC side balanced, the level of the difference between the pole voltages has to be controlled and kept to zero.

The rectifier and the inverter are interconnected through a 2000 km cable. The use of underground cable is typical for VSC-HVDC links.

11.2. CONTROL ALGORITHMS

11.2.1. Thyristor based HVDC system

The rectifier and inverter controllers of the HVDC system generate reference currents for the each of the converters respectively, besides initiating the starting and stopping of the DC power transmission in the HVDC system. At the inverter pole, extinction angle Gamma of the 6-pulse thyristor converters measured by the gamma measurement unit.

The protection systems are implemented in both rectifier and inverter side. The DC fault protection at the rectifier side detects the DC fault on the DC line and takes the necessary action to clear the fault. To discriminate between an AC fault and a DC fault, the low AC voltage detection system is implemented at the rectifier and the inverter side controller. At the inverter, the commutation failure prevention's control system [11.3] mitigates commutation failures due to AC voltage dips.

11.2.1.1. Synchronization and firing system

12-pulse firing control system performs the synchronization and generation of the 12 firing pulses. According to the computed alpha firing angle pluses generate and synchronize with the primary side voltages of the converter transformer by the controller, because the primary side voltages are less distorted. A phase locked loop (PLL) is used to generate three voltages synchronized on the fundamental component of the positive-sequence voltages. So, the firing pulse generator is synchronized to the three voltages generated by the PLL. At the zero crossings of the commutating voltages (AB, BC, CA), a ramp is reset and a firing pulse is generated whenever the ramp value becomes equal to the desired delay angle provided by the controller.

11.2.1.2. Steady-state V-I characteristic

In normal operation, the rectifier controls the current at the $I_{\mathrm{d\_ref}}$ reference value, whereas the inverter controls the voltage or gamma at the $V_{\mathrm{d\_ref}}$ or *Gamma_min* reference value.

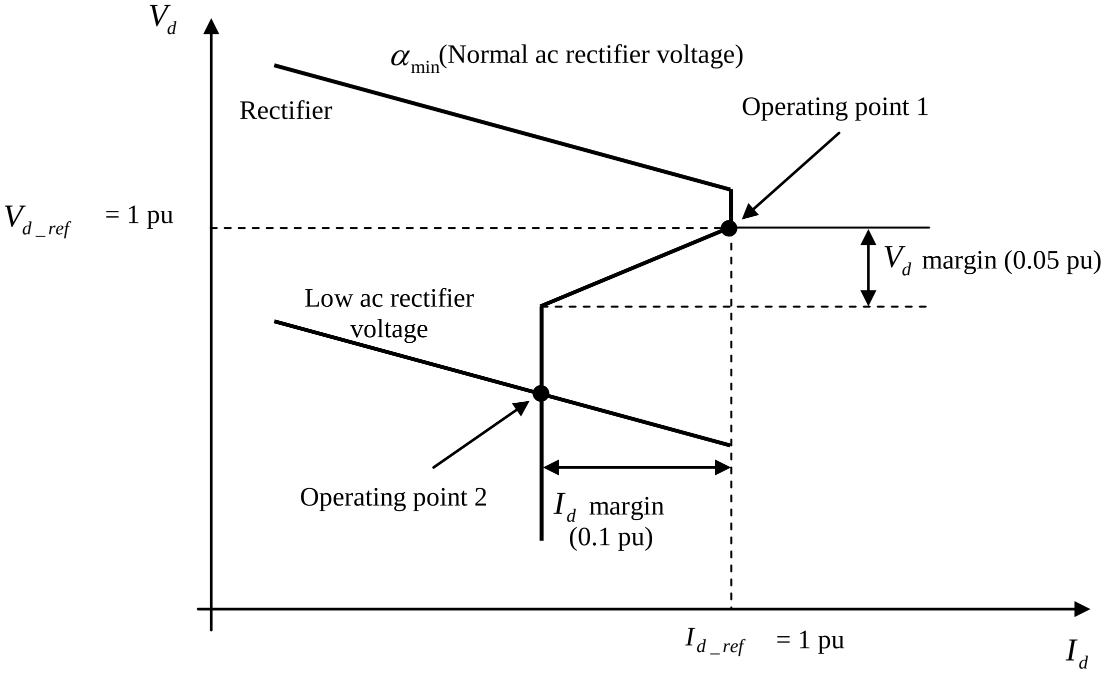

Figure 11.1 Rectifier and inverter steady-state characteristics and voltage dependent current order limiter (VDCOL) function

The system normally operates at point 1 as shown in the Figure 11.1. However, during a severe contingency producing a voltage drop on the rectifier side AC system, the operating point moves to point 2. The rectifier, therefore, is forced to a minimum α mode and the inverter is in the current control mode. Similarly, a voltage drop on the AC system feeding the inverter will force a control mode change to gamma regulation to limit the extinction angle to $\gamma_{\min}$. During severe contingency, a faster response is necessary to increase the commutation margin and consequently to reduce the probability of a commutation failure. The commutation failure prevention’s control generates a signal that decreases the maximum limit of the delay angle during the voltage drop (e.g., during an AC fault).

11.2.1.3. Voltage dependent current order limiter function

Another important control function is implemented to change the reference current according to the value of the DC voltage. This control, named voltage dependent current order limiter (VDCOL), automatically reduces the reference current ($I_{\mathrm{d\_ref}}$) set point when V_{dL} decreases (as, for example, during a DC line fault or a severe AC fault). Reducing the I_{d} reference currents also reduces the reactive power demand on the AC system, helping to recover from the fault. The VDCOL parameters are illustrated in Figure 11.2.

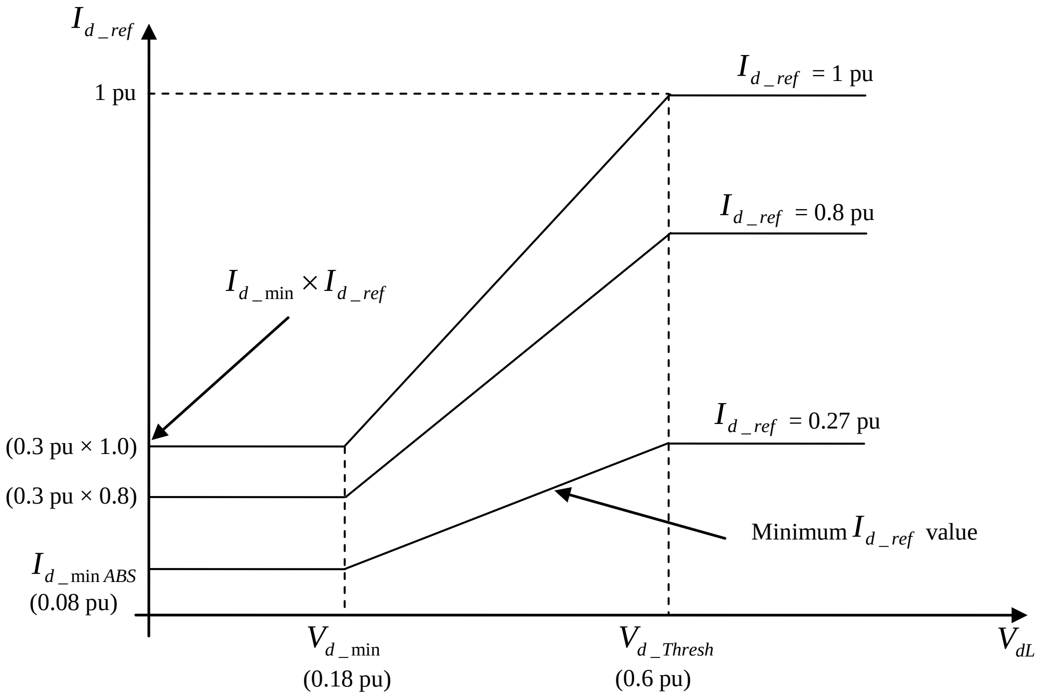

Figure 11.2 VDCOL Characteristic; $I_{\mathrm{d\_ref}} = f(V_{\mathrm{dL}})$

The $I_{\mathrm{d\_ref}}$ value starts to decrease when the V_{d} line voltage falls below a threshold value $V_{\mathrm{d\_Thresh}}$. When the DC line voltage falls below the $V_{\mathrm{d\_Thresh}}$ value, the VDCOL drops instantaneously to $I_{\mathrm{d\_ref}}$. However, when the DC voltage recovers, VDCOL limits the $I_{\mathrm{d\_ref}}$ rise time with a defined time constant.

11.2.1.4. Current, voltage, and gamma regulators

Both rectifier and inverter controls have a current regulator calculating firing α_i. At the inverter, operating in parallel with the current regulator is the voltage and/or gamma regulators calculating firing angles α_v and/or α_g. The effective α angle is the minimum value of α_i, α_v and/or α_g. All regulators are of the proportional-integral type. They should have high enough gains for low frequencies (<10 Hz) to maintain the current, voltage, or gamma response equal to the reference current ($I_{\mathrm{d\_ref\_lim}}$), reference voltage ($V_{\mathrm{d\_ref}}$), or reference gamma (*Gamma_min*), as long as α is within the minimum and maximum limits ($5 < \alpha < 166$ for rectifier, $92 < \alpha < 166$ for inverter). The regulator gains K_P and K_I are adjusted during small perturbations in the reference.

11.2.2. Voltage source based HVDC system

The identical design of the controller is implemented on the inverter side and the rectifier side of the VSC-HVDC system. The two controllers are independent with no communication between them. Each converter has two degrees of freedom; here these are used to control:

- P and Q in rectifier station
- U_{dc} and Q in inverter station.

The control of the AC voltage would be also possible as an alternative to Q. This requires an extra regulator which is not implemented in the simulated model.

Per-unit sampled voltages and currents are provided to the controller. The real time sampled quantities transform to space vector components α and β (real and imaginary part) by the Clark transformation. In order to have the same reference frame with the measured signals on the secondary side of the transformer, the measured signals (voltage and current measurements) on the primary side are rotated by ±pi/6 according to the transformer connection (YD11 or YD1) if it is required.

The direct current axis d and the quadratic axis q are computed from the α and β quantities by implementing $\alpha\beta - dq$ transformation. The PLL block measures the system frequency and provides the phase synchronous angle θ (more precisely $[\sin(\theta), \cos(\theta)]$) for the dq transformation. In steady state, $\sin(\theta)$ is in phase with the fundamental (positive sequence) of the α component and phase A of the PCC voltage (V_{abc}).

11.2.2.1. Outer active and reactive power and voltage loop

The outer loop regulators of the active and reactive power and voltage loop calculate the reference value of the converter current vector ($I_{\mathrm{ref\_dq}}$) which is the input to the inner current loop. The control modes are: in the *d* axis, either the active power flow at the PCC or the pole-to-pole DC voltage; in the *q* axis, either the reactive power flow at the PCC or AC voltage control at the PCC. Here the reactive power flow is considered and the regulator for AC voltage control at the PCC is not included (the AC voltage controller is an alternative to reactive power control). The main functions of the active and reactive power and voltage loop are described below.

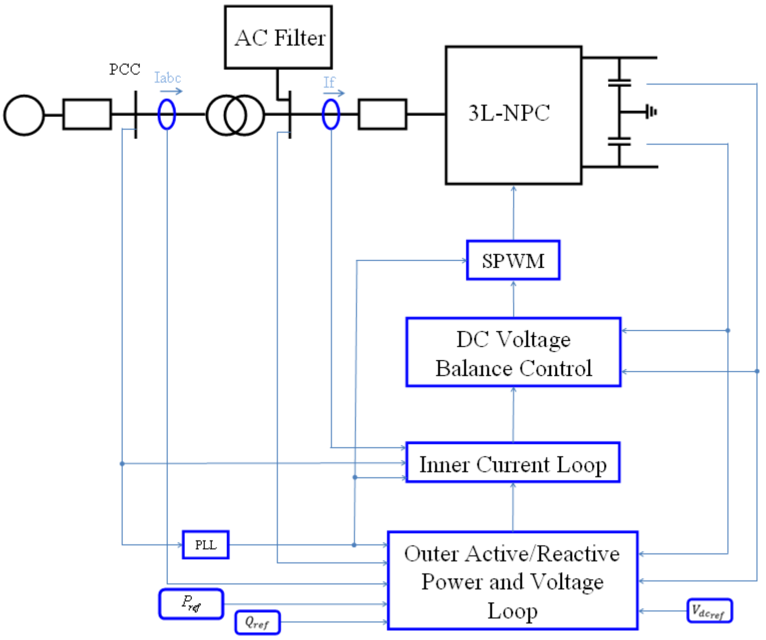

Figure 11.3 High Level Block Diagram of the Discrete VSC Controller

A PI regulator with a feed-forward control to increase the speed response provides the reactive power control regulator. To avoid integrator wind up the following actions are taken: the error is reset to zero, when the measured PCC voltage is less than a constant value (i.e., during an AC perturbation); when the regulator output is limited, the limitation error is fed back with the right sign, to the integrator input. The AC voltage override's controller, based on two PI regulators, will override the reactive power regulator to maintain the PCC AC voltage within a secure range, especially in steady-state.

Similar to the reactive power control a PI regulator with feed-forward control provides the active power control. For ramping the active power towards the desired value with an adjustable ramp rate in the network the when the control is de-blocked an extra ramping block also implements in the active power control regulator. The ramped value is reset to zero when the converter is blocked. The active power regulator will override with the DC voltage control based on two PI regulators, to maintain the DC voltage within a secure range, especially during a perturbation in the AC system of the station controlling the DC voltage.

The DC voltage control regulator uses a PI regulator; this regulator is enabled when the active power control is disabled. The DC voltage regulator output is a reference value, for the *d* component of converter current vector, for the current reference limitation.

The active and reactive power references - calculated by the *P* and *Q* controllers - transfer to the current references according to the measured voltage at the filter bus in the current reference calculator. The current reference is estimated by dividing the power reference by the voltage (up to a minimum preset voltage value). The current reference vector is limited to the maximum acceptable value (i.e., equipment dependent). In power control mode, equal scaling is applied to the active and reactive power reference when a limit is imposed. In the DC voltage control mode, higher priority is given to the active power when a limit is imposed for an efficient control of the voltage.

11.2.2.2. Inner current loop

Feed forward scheme is implemented in the AC current controller to track the current reference vector (*d* and *q* components) in order to achieve a fast control of the current at load changes and disturbances (e.g., so short-circuit faults do not exceed the references) [11.2], [11.4] and [11.5]. In essence, the controller consists of measuring the V_{dq} vector voltages (in d-q reference frame) and computing the converter output voltage by adding the voltage drops due to the currents across the impedance between the V_{PCC} and the PWM-VSC voltages. The *d* and *q* components are decoupled to obtain two independent first-order plant models. For reducing the steady state error to zero a proportional integral (PI) feedback of the converter current is used. The unlimited reference voltage vector $V_{\mathrm{ref\_dq\_tmp}}$ is the output of the AC current controller. Since overmodulation is not desired the reference voltage vector amplitude will limit to 1.0.

For generating optimized reference voltage vector, the voltage conditioning controller takes into account the actual DC voltage and theoretical maximum peak value of the fundamental bridge phase voltage in relation to the DC voltage. Here the ratio between the maximum fundamental peak phase voltage and the DC voltage (i.e. modulation index) is considered 0.816.

The inverse *dq* and inverse Clark transformation blocks are required to generate the three-phase voltage references to the PWM.

11.2.2.3. DC Voltage Balance Control

In the steady state the difference between the DC sides voltages (positive and negative) are controlled to keep near zero. Due to the nonlinearity on lack of precision in the execution of pulse width modulation bridge voltage or changes of active/reactive converter current small deviations between the pole voltages may occur. Furthermore, deviations between the pole voltages may be due to the inherent imbalance in the impedances of the circuit components.

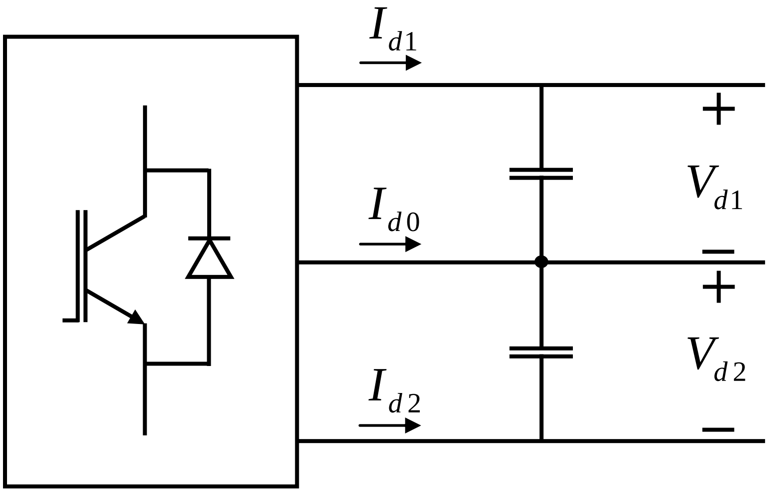

Figure 11.4 DC Voltages and Currents of the Three-Level Bridge

The DC midpoint current I_{d0} determines the difference V_{d0} between the upper and lower DC voltages:

$$I_{\mathrm{d0}} = -(I_{\mathrm{d1}} + I_{\mathrm{d2}}) = -C\frac{\mathrm{d}}{\mathrm{d}t}(V_{\mathrm{d1}} - V_{\mathrm{d2}}) = -C\frac{\mathrm{d}}{\mathrm{d}t}V_{\mathrm{d0}} \tag{11.1}$$

By changing the conduction time of the switches in a pole it is possible to change the average of the DC midpoint current I_{d0} and thereby control the difference voltage V_{d0}. For example, a positive difference ($V_{\mathrm{d0}} \geq 0$) can be decreased to zero if the amplitude of the reference voltage which generates a positive midpoint current is increased at the same time as the amplitude of the reference voltage which generates a negative DC midpoint current is decreased. This is done by the addition of an offset component to the sinusoidal reference voltage. Consequently, the bridge voltage becomes distorted, and to limit the distortion effect, the control has to be slow. Finally, for a better performance this function should be activated in the station controlling the DC voltage.

11.3. CABLE DESIGN

Design procedure of the cable is discussed in chapter 8 is applied for the design of the cable. In this chapter, CD layout of the cable and the criteria for choosing distance between the cooling stations (*L*) will discuss later in this section. As mentioned before typical values of the radius of the copper former are in the range 5-20 mm [7.3], [7.6], and [8.3]. In [7.3] it is shown that a copper cross section area of 400 mm^2 is enough to tolerate 63 kArms AC fault current for 0.6 s with a temperature increase of 20 K. In the following a radius of the former R_f = 20 mm is assumed.

The design of the cable based on commercially available 2G HTS (YBCO coated conductors) is considered. An YBCO tape with 12 mm width and 0.1 mm thickness produced by Superpower Inc. is assumed. Figure 8.3 shows the critical engineering current density of these conductors in the operating temperature range as a function of the magnetic field.

For the design of the dielectric, a breakdown voltage E_b = 20 kV / mm can be assumed for LN_2/PPLP [8.6] in AC condition and has also been assumed for LH_2/paper insulation subject to DC operation [6.22], so this value is assumed. A conservative safety margin $\eta = 0.3$ is assumed due to the DC operation.

The given data in Table 8.2 are assumed in the following for the design of the cable. A corresponding thickness of thermal insulation of 25 mm is also assumed. Also, the average mass density, specific heat and dynamic viscosity of LN_2 and LH_2 in the operating temperature and pressure intervals are listed in Table 8.3 are considered.

Choosing the distance between the cooling stations for cable design is the one the most important parameters, where the distance between the cooling stations will change the cable diameter, cable cost and the required cooling power of the system. Figure 11.5 - Figure 11.7 show the effect of the distance between the cooling stations on the cooling energy, material cost, and mass flow rate of the LN_2 respectively. For calculating the cost, the amount of the different material in the cable and the cooling cost of the HTS-DC cable (100€/W_{cold}) is considered, also the constant cost for auxiliary equipment per each cooling station is taken into account. The cost of the HTS material based on the state of the art of the HTS material cost (100 €/kA-m) and optimistically expected material cost (20 €/kA-m) is depicted in Figure 11.6. Figure 11.8 compares the cost of the HTS-DC cable with different available DC transmission technologies. In the case of the conventional DC cable investment cost, 0.25 M€/km-MW for overhead line, 0.842 M€/km-MW for line commutated controlled (LCC) based HVDC XPLE cable, and 0.947 M€/km-MW for voltage source control (VSC) based HVDC XPLE cable is considered [11.6]. As it is shown in Figure 11.8 HTS-DC cable system is more preferable than underground cable and somehow it is comparable to the DC overhead line. Based on the economic evaluation a cooling station distance *L* = 20 km is considered in the rest of this chapter.

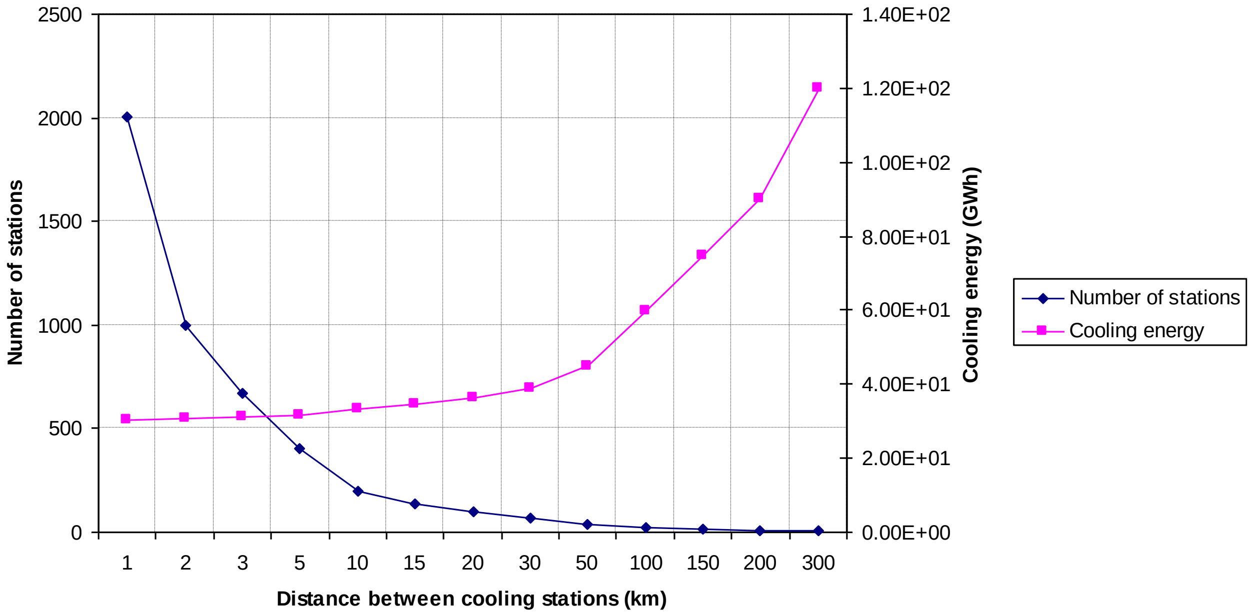

Figure 11.5 Effect of the distance between cooling stations on cooling energy of the cable

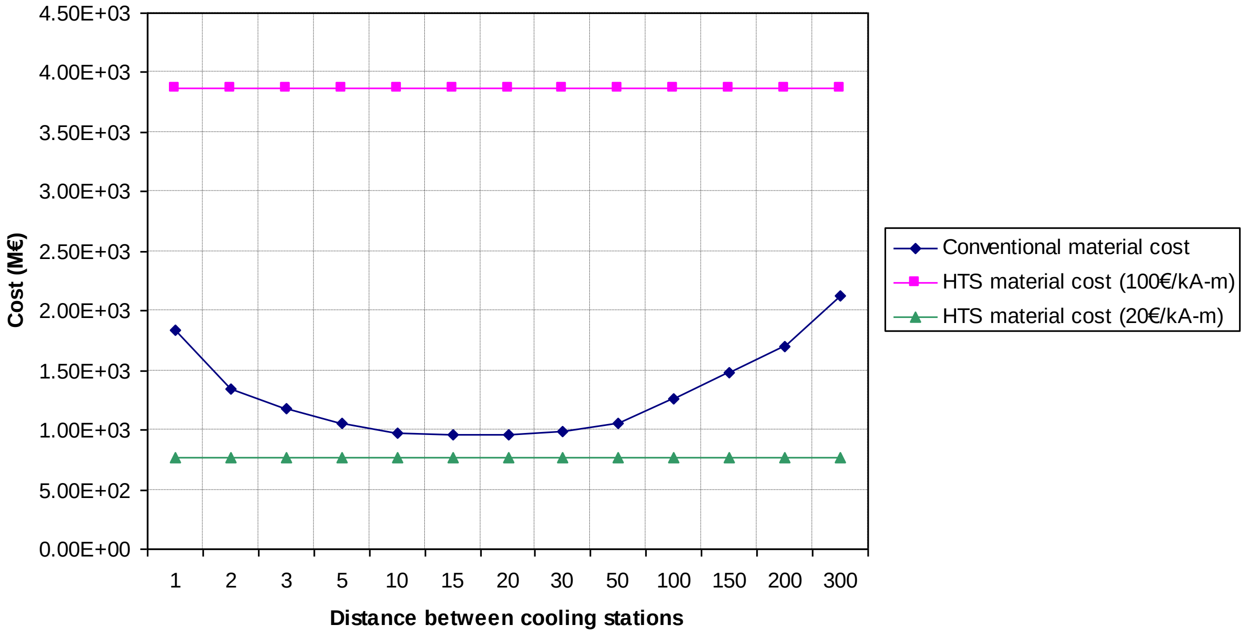

Figure 11.6 Effect of the distance between cooling stations on the cost of the cable material cost

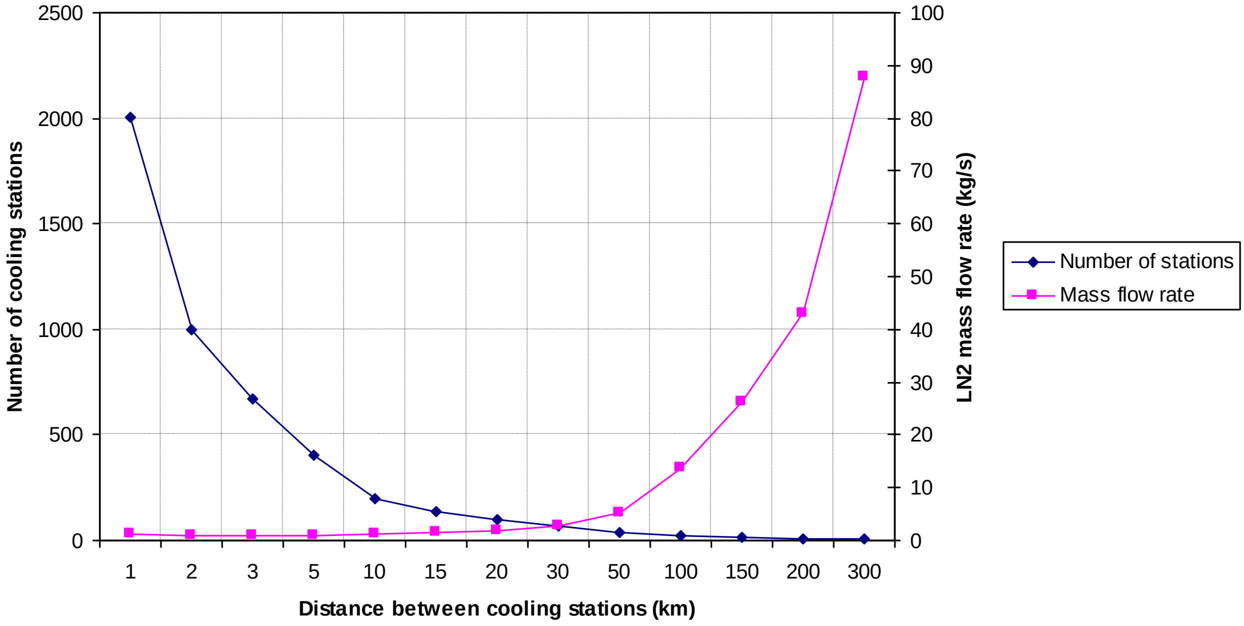

Figure 11.7 Effect of the distance between cooling stations on mass flow rate of the LN_2

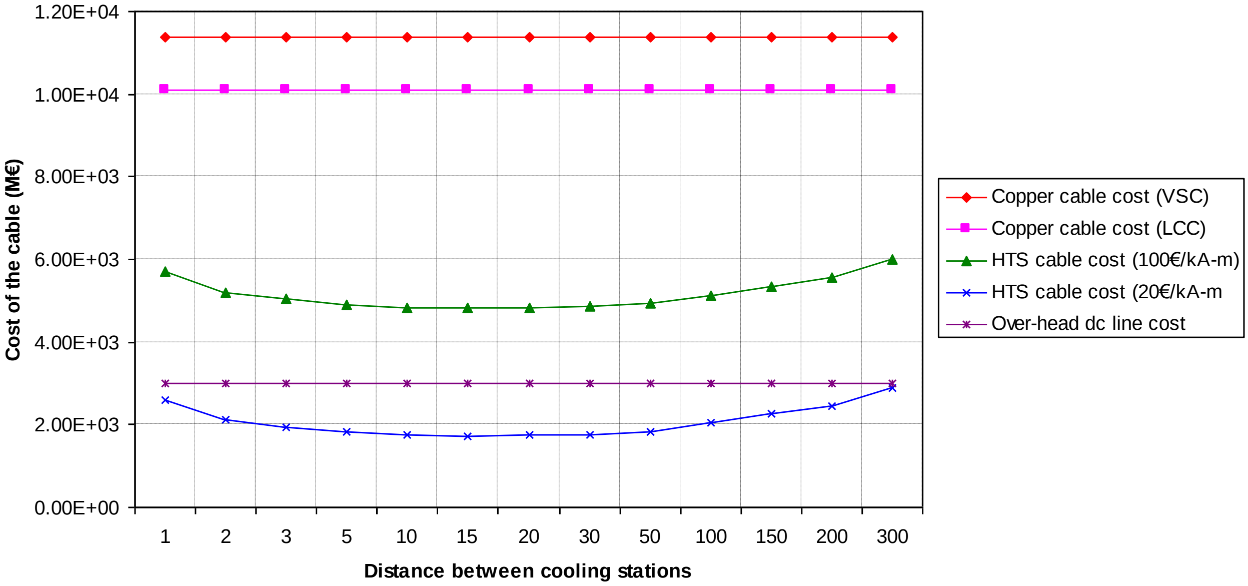

Figure 11.8 Comparison of the XPLE copper based cable and copper base overhead line DC transmission with the HTS-DC cable cost respect to the distance between cooling stations and HTS material cost

In [11.6] the cost of the XLPE DC cable and the overhead line is reported for the 1000 MW, 190 km, ± 320 kV, DC system. This case study is relevant to the HVDC connection between France and Italy. In this connection underground XLPE DC cable and VSC based HVDC system is considered. A brief comparison between HTS-DC cable and conventional XLPE DC cable is presented here. Figure 11.9 shows the cost comparison between the HTS-DC cable and the conventional DC system. As it is illustrated in Figure 11.9 the most preferable solution seems to be the overhead line connection. However, comparing the XLPE DC cable with HTS-DC cable shows that the cable based on the HTS material is more economical when 19 km as the distance between cooling stations is chosen. Figure 11.10 illustrates that in this case the cost of the non-HTS material and cooling cost is more than the HTS material cost.

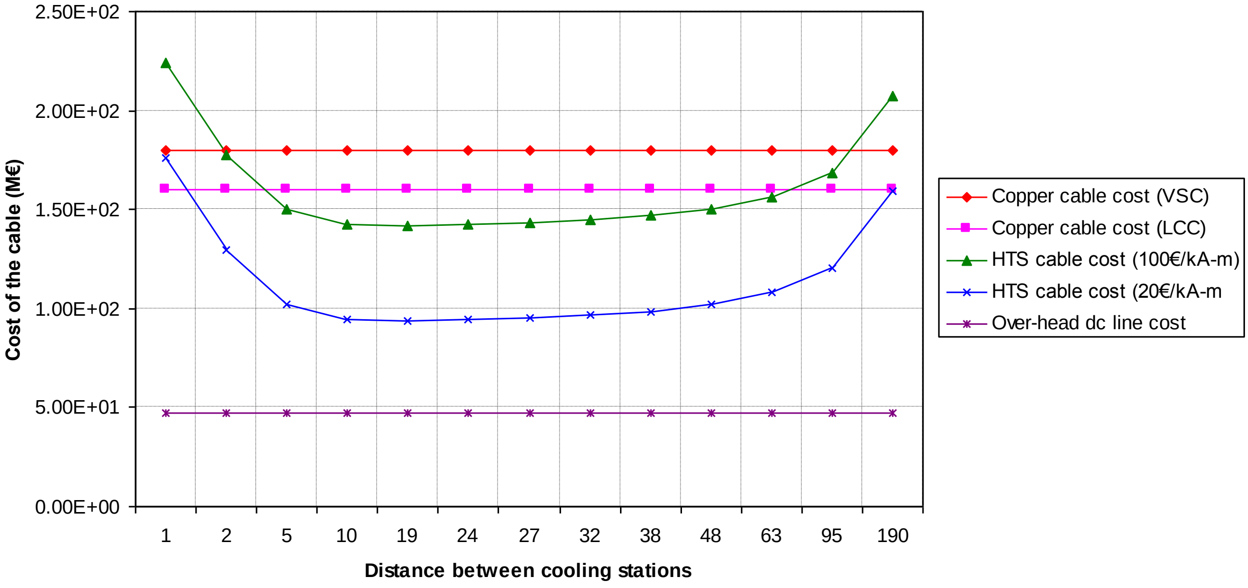

Figure 11.9 Comparison of the XPLE copper based cable and copper base overhead line DC transmission with the HTS-DC cable cost respect to the distance between cooling stations and HTS material cost

By considering above mentioned assumptions, the isogradient curve of the cable is drawn and the choice of the outer diameter and mass flow is made by the procedure which is explained in 8.5. The isogradient curve of the cable is depicted in Figure 11.11.

The radiation heat loss and the termination loss of the cable by considering the data provided in Table 8.4 and by using equation (8.18) is 0.91 MW per 20 km of the cable is calculated. The overall cooling power of the cable is 100 times of this power equal to 91 MW. The major part of the heat loss is the radiation heat loss rather than the termination heat loss.

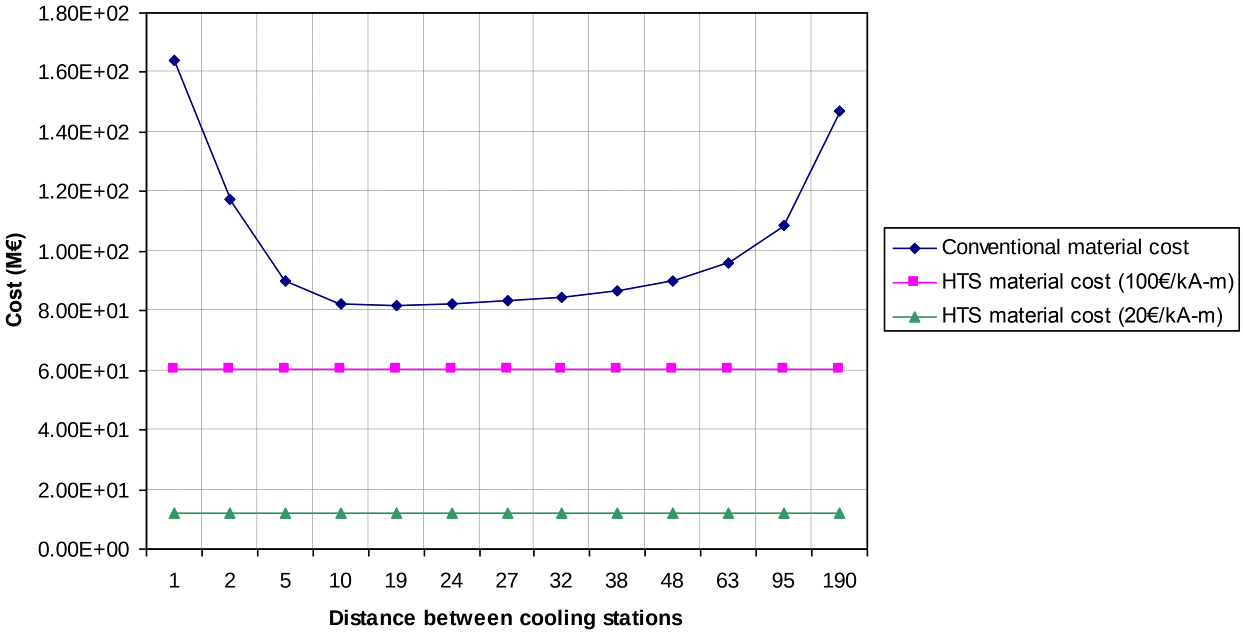

Figure 11.10 Effect of the distance between cooling stations on the cost of the cable material cost

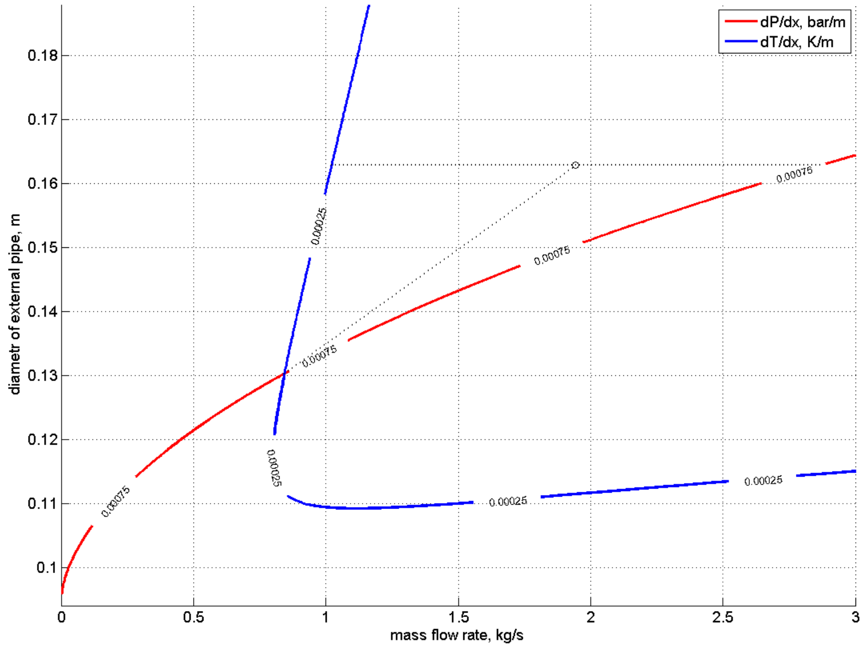

Figure 11.11 Isogradient curve of the cable for LN_2 obtained from equations (8.13)-(8.15) with $R_f = 20$ mm and $L = 20$ km

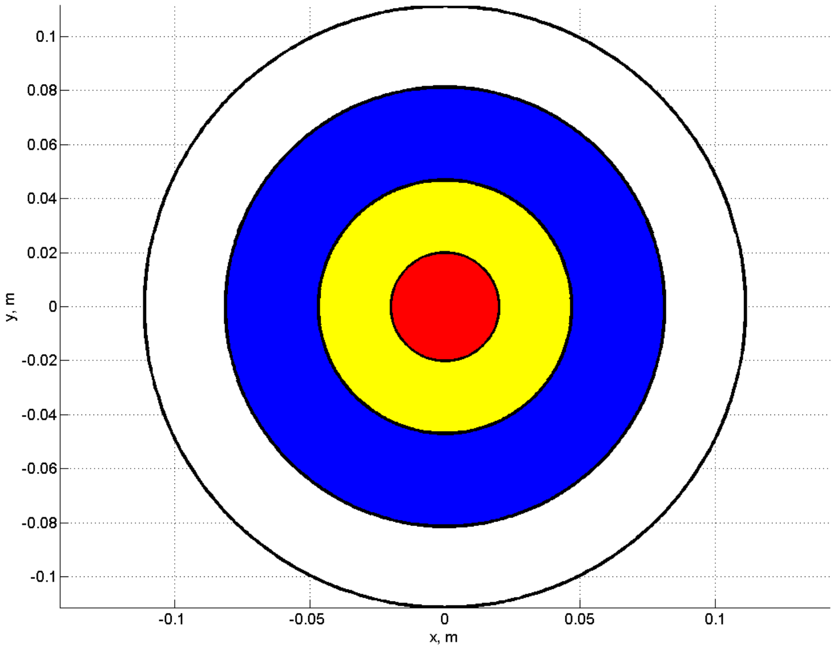

Figure 11.12 Diameters of the cable, red: former of the cable, yellow: electrical insulation, blue: LN_2, white: hybrid thermal insulation. Note: the superconducting thickness is too narrow and is not visible in the actual sized figure.

A 6400 MW / ±320 kV superconducting HVDC link is investigated in this section. The procedure and the assumptions introduced in chapter 8 are used for the design of the HTS cable and for the evaluation of its performance. If not otherwise specified a distance of 20 km between the cooling stations is assumed and a cold dielectric layout is considered.

Conventional DC cables with extruded XLPE insulation are now available and are gaining increasing attention for application to VSC based HVDC systems; their applicability is being extended also to CSC based HVDC with polarity reversal for bulk energy transmission [11.7]. Voltage limit of commercial XLPE cables now reaches ± 320 kV, corresponding to a power rating in the range 800-1000 MVA per bipole [11.8]. Cu/XLPE cables at ± 320 kV are likely to be, now and in the future, the reference benchmarking for transmission technologies. The Joule loss of a Cu/XLPE system depends on the transmitted power and are given by

$$P_{\mathrm{Cu}} = \frac{2\rho_{\mathrm{Cu}} J_{\mathrm{Cu}}}{V_{\mathrm{dc}}} \left(\frac{P}{P_{\mathrm{n}}} \right)^2 P_{\mathrm{n}} \tag{11.2}$$

A current density J_{cu} = 1 A/mm^2 and a resistivity ρ_{cu} = 2.1 μΩcm are assumed in the following which are typical for copper based HVDC cables. It is clear from the equation (11.2) that the loss of the Cu cables decreases with the voltage rating of the cable, hence high voltage is the only way both for increasing the transport capacity and for reducing the loss. The comparison of the cooling energy and copper loss in the study case considering the distance between the cooling stations is depicted in Figure 11.13.

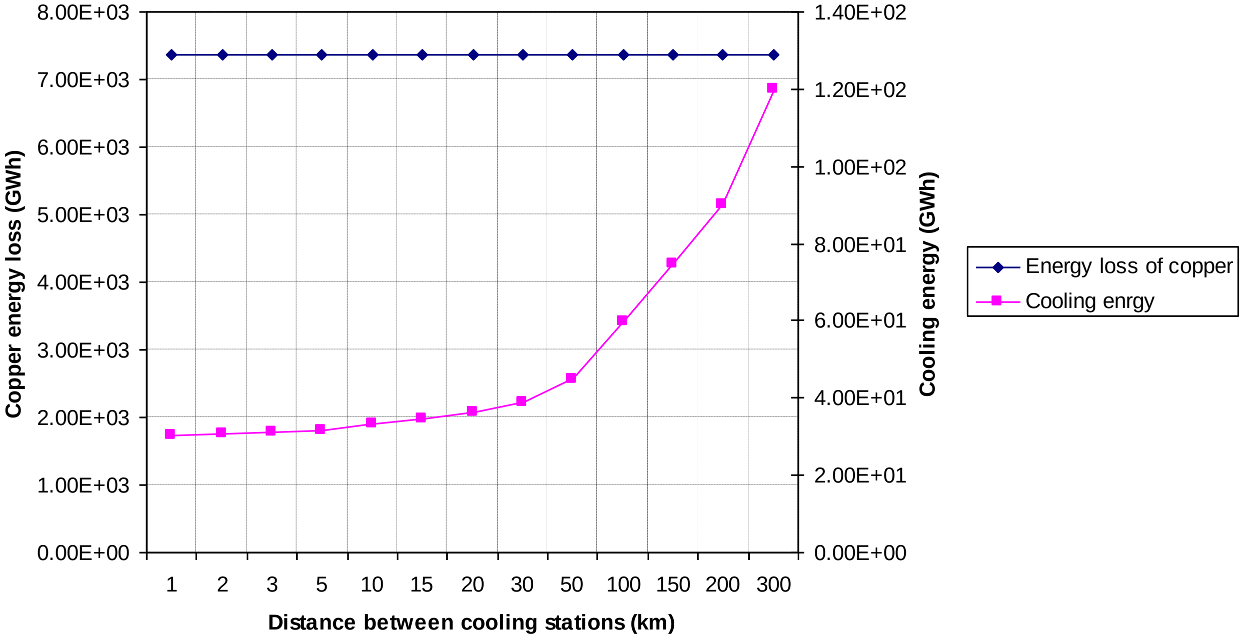

Figure 11.13 Copper energy loss and the cooling energy respect to the distance between cooling stations

11.4. MODELING OF THE CABLE IN POWER SYSTEM

HTS-DC cable is simulated by the lumped parameter per unit lent of the cable (km). For the first assumption currents ripples of the DC system are ignored for driving the lumped parameter of the superconducting cable so the skin effect resistance of the cable is not considered. Lumped parameter of the cable based on [11.9] can be given as follows:

(11.3)
$$L_{\mathrm{self}} = l_{\mathrm{cable}}\left(\mu_0 \frac{\pi r_{\mathrm{in}}}{l_{\mathrm{p}}^2} + \frac{\mu_0}{2\pi}\ln\left(\frac{GMR}{r_{\mathrm{in}}}\right)\right)$$

(11.4)
$$C_{\mathrm{o}} = \frac{2\pi\varepsilon_0\varepsilon_{\mathrm{S}}\varepsilon_{\mathrm{ins}}}{\varepsilon_{\mathrm{ins}}\ln\frac{2H - r_{\mathrm{out}}}{r_{\mathrm{out}}} + \varepsilon_{\mathrm{S}}\ln\frac{r_{\mathrm{out}}(2H - r_{\mathrm{in}})}{r_{\mathrm{in}}(2H - r_{\mathrm{out}})}}$$

where $\mu_0 = 4\pi \times 10^{-7}$ is the magnetic permeability of the free space, r_{in} is the radius of HTS layer, l_{p} is the twist pitch of the layer, l_{cable} is the length of the cable, $\varepsilon_0 = 8.85 \times 10^{-12}$ is the permittivity of the air, ε_{S} is the surrounding environment relative permittivity, $\varepsilon_{\mathrm{ins}}$ is the insulator (dielectric material of cable) relative permittivity, r_{out} is the radius of insulation layer, and H is the distance from center of the cable to the ground. Calculated cable parameter per unit length of the cable is summarized in Table 11.1.

Table 11.1. Lumped parameters of the cable

	Inductance [mH/km]	Capacitance [pF/km]	Resistance [mΩ/km]
Cable parameters	0.93	16.42	0.0

11.5. TRANSIENT BEHAVIOR OF THE CABLE

The control system of the HVDC system based on [11.10] as discussed in previous sections is implemented (see section 11.2). The proper protection during the AC and/or DC side fault adapts to the control system of LCC based HVDC link in order to block the rectifier and inverter during the fault. Simulation by using Matlab/Simulink power system toolbox is carried out.

The different transient conditions are expected to happen in the system and each of which will have different transient currents. In the simulation case planned transient because of the energy transfer management and unplanned transients because of the short circuit in AC side (both single phase to ground and symmetrical three phase fault) and DC side fault in inverter side is considered.

Figure 11.14 shows the transient behavior of the HTS cable in LCC based HVDC system. The system starts to load the cable at t = 0.3 s with a planned ramp rate of the 5.0 pu/s. With the chosen ramp rate, the system increases the current in the cable gradually to reach the full load current. For the contingency reason’s power transferring of the HVDC link could reduce or increase. Changing the power cause to change of the current through the HVDC link and it can add a transient in the DC link. In the simulation case the current through the cable reduces by 20% at t = 0.9 and increases again by 20% at t = 1.1 s. The system responses the current change without any significant disturbance. Another contingency situation in the HVDC system happens because of the voltage amplitude change in the AC power system. In the simulation case study the DC side voltage increases by 10% at t = 1.6 s and decreases by 10% at t = 1.8 s during this change no disturbance occurs in the cable. One of the unplanned transients in the power system is the single phase to ground fault. In the simulation case a single phase to ground short circuit is simulated in the inverter side AC network at t = 2.2 s and the fault is ended at t = 2.3 s. Because of the single phase short circuit current through the cable increases and the protection module of the controller is activated and the system shuts down. After clearance of the fault the system loaded again with the pre-planned ramp rate of the 5.0 pu/s. Three phase short circuit at the inverter side is simulated at t = 3.2 s and the three phase short circuit ends at t = 3.3 s. In the case of the three phase short circuit the protection module activates again and the power transmitting in the HVDC link set to zero. After the clearance of the short circuit the system loaded again with the pre-planned ramp rate of the 5.0 pu/s. Another unplanned transient in the system is the DC side short circuit. DC side short circuit is simulated at t = 4.1 s and the system backs to the service at t = 4.15 s. This fault is detected by the protection system and the power transmitting function of the HVDC link sets to zero, and after the fault clearance the system cold loaded by the planned ramp rate (here 5.0 pu/s). As it is illustrated in Figure 11.14 the protection module prevents the current increment more than preset value which can be set by considering the critical current of the HTS material.

In concluding this investigation, it is worth to point out that from the point of view of the HVDC converters and AC power system superconducting cable will not have any extraordinary behavior during different circumstances.

Figure 11.15 illustrates the current ripple of the DC network during the normal operation of the HVDC system. DC side current ripple is important while the current ripples could produce the extra heat load in the superconducting cable. In the simulated network the current ripple is less than ±1%. This ripple cannot make any significant heat loads in the normal operation. The AC loss calculation is required, especially when the short circuit and fast power delivery direction change happens, to design the cooling system and guarantee the superconductivity during all the situations.

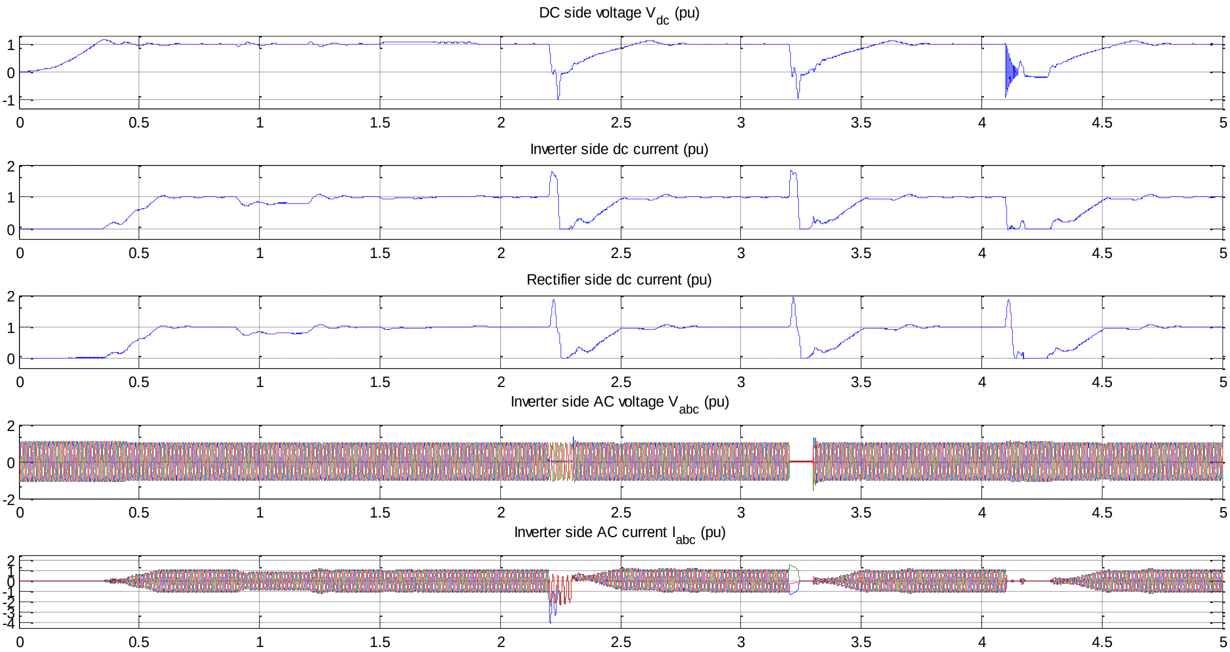

Figure 11.14 Transient behavior of the HTS cable during different transients in LCC based HVDC system

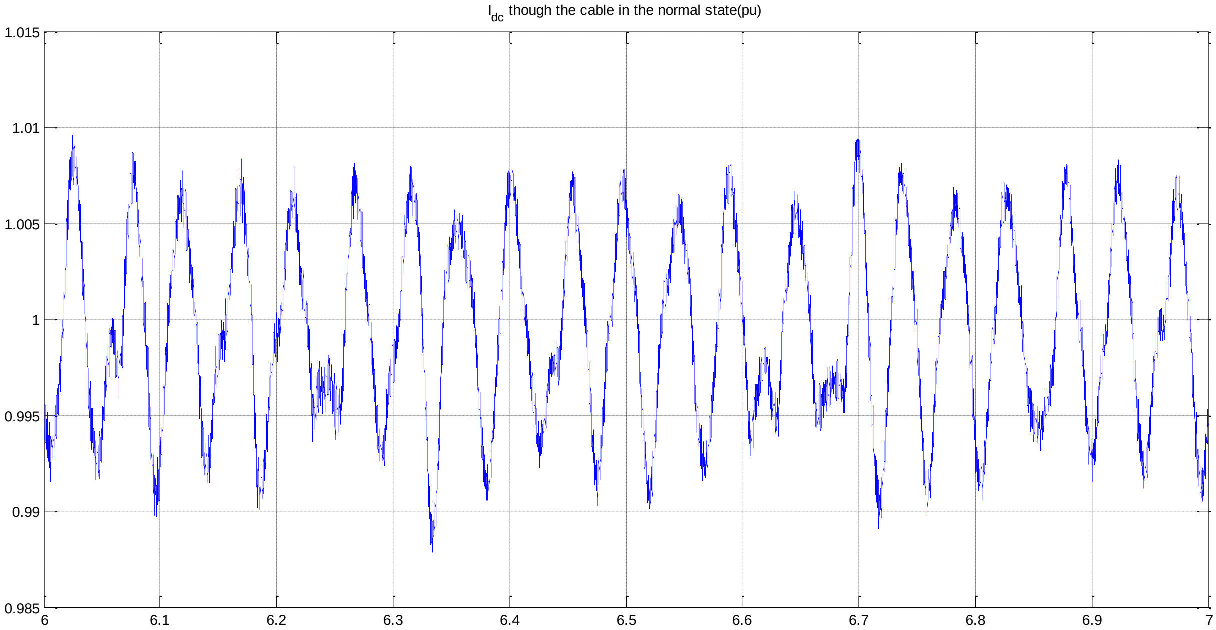

Figure 11.15 DC side current ripple during normal operation state in LCC based HVDC

Figure 11.16 shows the transient behavior of the HTS cable in VSC based HVDC system. The control system starts to control the DC voltage at t = 0.1 s. Then the system starts to load the cable at t = 0.3 s with a planned ramp rate. With the chosen ramp rate, the system increases the current in the cable gradually to reach the full load current. For the contingency reason’s power transmitting of the HVDC link could reduce or increase. Changing the power cause to change of the current through the HVDC link and it can add a transient in the DC link. In the simulation case the current through the cable reduces by 10% at t = 2.0 and increases again by 10% at t = 2.7 s. The system responses the current change without any significant disturbance. At t = 3.1 s reactive power reference decreases by 10% during this change no significant transient happens in the system. Another contingency situation in the HVDC system happens because of the voltage amplitude change in the AC power system. In the simulation case study the DC side voltage decreases by 5% at t = 3.3 s s and increases by 5% at t = 4 s during this change no disturbance observable in the cable. At t = 4.5 s AC voltage of the rectifier side decreases by 10% and the AC voltage increases by 10% at t = 4.84 s during this transient system works properly without any problem. One of the unplanned transients in the power system is the single phase to ground fault. In the simulation case a single phase to ground short circuit is simulated in the inverter side AC network at t = 5.2 s and the fault is ended at t = 5.32 s. As it is illustrated in Figure 11.16 inverter control decreases transmitted power through the cable and since the DC side voltage does not experience too much disturbance the system response the single phase short circuit without DC current disturbance. After clearance of the fault the system loaded again. Three phase short circuit at the inverter side is simulated at t = 8.4 s and the three phase short circuit ends at t = 8.52 s. During three phase short circuit DC side voltage experience severe disturbance and the inverter controller by decreasing transmitted power maintains the DC side voltage, therefore larger disturbance in the DC side current occurs. During the three phase short circuit stricter cooling system to guarantee the superconducting situation is required. After the clearance of the short circuit the control system immediately starts to transmit the power. This behavior introduces larger oscillation and increases the electromagnetic heat loss (i.e. AC loss) of the cable and the cooling for the period of 3 s is necessary.

In this case DC side short circuit is not simulated. During DC side short circuit, the DC sides capacitors is discharged and since there is no resistance in the HTS cable short circuit current ramp rate will be too high and a proper current limiting technology is required.

In concluding this investigation, it is worth to point out that from the point of view of the HVDC converters and AC power system superconducting cable will not have any extraordinary behavior during different circumstances.

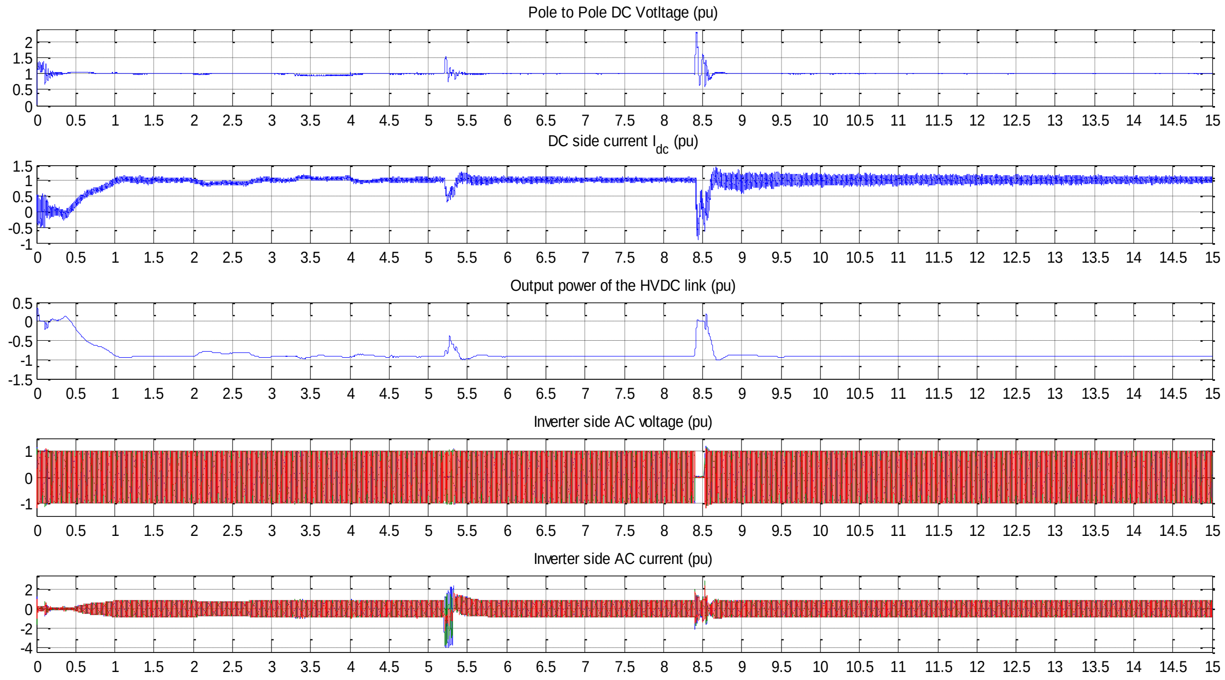

Figure 11.16 Transient behavior of the HTS cable during different transients in VSC based HVDC system.

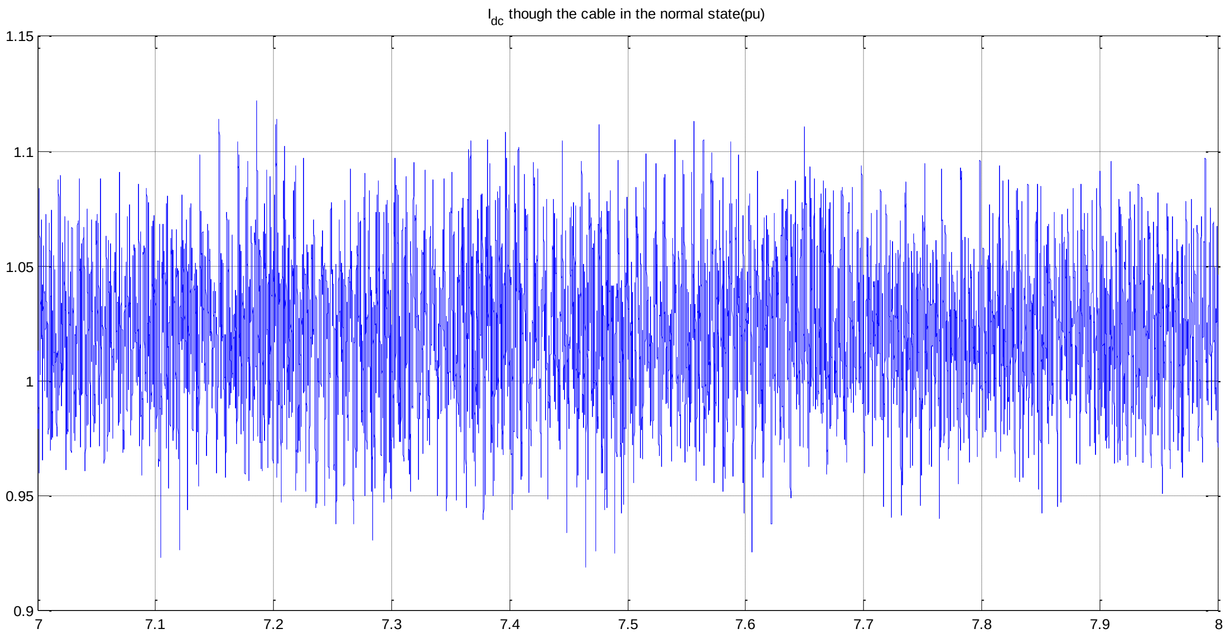

Figure 11.17 DC side current ripple during normal operation state in VSC based HVDC

Figure 11.17 illustrates the current ripple of the DC network during the normal operation of the HVDC system. DC side current ripple is important while the current ripples could produce the extra heat load in the superconducting cable. In the simulated network the current ripple is less than ±10%. This ripple could introduce electromagnetic heat loads (AC loss) in the normal operation so the stricter cooling design is required. The AC loss calculation is required, especially when the short circuit happens, to design the cooling system and guarantee the superconductivity during all the situations.

11.6. REFERENCES

[11.1] Sadaba, Alonso, O., P. Sanchis Gurpide, J. Lopez Tanerna, I. Munoz Morales, L. Marroyo Palomo, "Voltage Harmonics Generated by 3-Level Converters Using PWM Natural Sampling," IEEE 32nd Annual Power Electronics Specialist Conference, 17–21 June 2001, Vancouver, BC, Vol. 3, pages: 1561–1565, DOI:10.1109/PESC.2001.954341

[11.2] A. Lindberg “PWM and control of two and three level high power voltage source converters,” Licentiate thesis, ISSN-1100-1615, TRITA-EHE 9501, The Royal Institute of Technology, Sweden, 1995.

[11.3] L. Zhang and L. Dofnas, “A Novel Method to Mitigate Commutation Failures in HVDC Systems,” International Conference on Power System Technology, Proceedings PowerCon 2002, Vol. 1, 13–17 October 2002, page: 51–56, DOI: 10.1109/ICPST.2002.1053503

[11.4] Weixing Lu and Boon-Teck Ooi, “Optimal Acquisition and Aggregation of Offshore wind Power by Multiterminal Voltage-Source HVDC,” IEEE Transactions on Power Delivery, Vol. 18, No. 1, January 2003, pages: 201–206, DOI: 10.1109/TPWRD.2002.803826

[11.5] C. K. Sao, P.W. Lehn, M.R. Iravani, and J.A. Martinez, “A benchmark system for digital time-domain simulation of a pulse-width-modulated D-STATCOM,” IEEE Transactions on Power Delivery, Vol. 17, No. 4, October 2002, pages:1113–1120, DOI: 10.1109/TPWRD.2002.803836

[11.6] CIGRE Working Group B4.46 “Voltage Source Converter (VSC) HVDC for Power Transmission – Economic Aspects and Comparison with other AC and DC Technologies”, 2012, ISBN: 978-2-85873-184-8, online available: http://www.e-cigre.org/Publications/file.asp

[11.7] Y. Ohki, “Developmenet of XPLE-Insulated cable for high-voltage DC submarine transmission line (1),” IEEE Electrical Insulation Magazine, Vol. 29, No. 4, 2013, pages 65-67, DOI: 10.1109/MEI.2013.6545264

[11.8] E. Zaccone, “High voltage underground and subsea cable technology options for future transmission in Europe,” E-Highway 2050, WP3 workshop, April 15th 2014, Brussels, online: http://goo.gl/grnxPQ

[11.9] M. -C. Dinh, S. -K. Kim, J. -G. Kim, M. Park, I. -K. Yu, and B. Yang, “Loss Characteristic Analysis of an HTS DC Model Connected to a VSC-HVDC System,” IEEE Transactions on Applied Superconductivity Vol. 23, No. 3, June 2013, DOI: 10.1109/TASC.2013.2239343

[11.10] M. O. Faruque, Y. Zhang, and V. Dinavahi “Detailed Modeling of CIGRÉ HVDC BenchmarkSystem Using PSCAD/EMTDC and PSB/SIMULINK,” IEEE Transactions on Power Delivery, Vol. 21, No. 1, January 2006, pages 378-387, DOI: 10.1109/TPWRD.2005.852376

CONCLUSION

In this thesis integration of high temperature superconductor technology in the future advanced power system has been investigated. In particular superconducting magnetic energy storage system (SMES) and high temperature superconducting DC cable has been studied.

The complete design method, including the magnet and power electronic interface design has been discussed in details. The developed design method has been applied to the design of an industrial scale conduction cooled SMES system, more specifically 1 MW - 5 s SMES system. Commercially available high temperature superconductor (HTS) material (YBCO) and magnesium diboride (MgB_2) tapes have been considered for the design of the magnet; and three different magnets have been designed. In the case of the MgB_2 solenoidal 3T magnet and in the case of the YBCO both 3 T and 8 T solenoidal magnets have been designed. AC loss of the magnets has been evaluated and the required materials for each case have been calculated. Also, the cooling power requirement of each case and round trip efficiency of the SMES system has been evaluated. The SMES system and the medium voltage power system have been simulated in Matlab/Simulink. A multifunctional control algorithm for compensating voltage sag and improving the power quality of the power system has been developed and implemented in the simulation. For choosing the switching frequency of the power electronics interface of the SMES system, lumped parameter model of the coil has been derived. Simulation results show the advantages of the SMES system and utilized control algorithm for this application.

As a second part of the thesis, high temperature superconducting DC (HTS-DC) cable for transmission and distribution power system has been studied. A method for both the electromagnetic and the thermo fluid-dynamic design of power cable has been developed. As a first case study superconducting DC collector grid for offshore wind-park technically and economically has been evaluated. For this, the HTS-DC cables for different part of the collector grid have been designed, the cost model of the wind park collector and loss model of the system has been introduced. The results show that the superconducting DC collector economically comparable with conventional wind park collector.

Also, the transient behavior of the high temperature superconducting DC cable in high voltage DC (HVDC) system, which is crucial for stability, has been studied. Both line commutated converters (LCC) and voltage source converters (VSC) have been considered. Construction and required controllers have been discussed. The HTS-DC cable by considering the cost of the cable has been designed. Lumped parameter electrical model of the cable has been derived and implemented in the simulated network in Matlab/Simulink. Different expected perturbations are simulated and the behavior of the cable for them has been studied. In this study it has been assumed that the HTS cable has always been remained in the superconducting condition. The simulation results show that the HTS-DC cable has no extraordinary behavior.